ANALYSIS OF CONJUGATE LIGHTNING-INDUCED ELECTRON PRECIPITATION EVENTS USING THE VLF REMOTE SENSING METHOD

By

DOOYOUNG KIM

A DISSERTATION PRESENTED TO THE GRADUATE SCHOOL
OF THE UNIVERSITY OF FLORIDA IN PARTIAL FULFILLMENT
OF THE REQUIREMENTS FOR THE DEGREE OF
DOCTOR OF PHILOSOPHY

UNIVERSITY OF FLORIDA

2020

This dissertation is dedicated to my grandmother, 박홍순
and to my husband, Anthony Joseph Erdman.

ACKNOWLEDGMENTS

As this Ph.D. journey comes to an end, I realize there are many people to whom I owe many thanks. First, I would like to thank my principal adviser, Dr. Robert Moore, for supervising my doctoral thesis. I am very grateful for his support and enthusiasm that helped me through my research. Thanks to him, I have traveled to many interesting, remote, but beautiful places, including Greenland and Antarctica.

Next, I would like to thank Dr. Martin Uman, Dr. Vladimir Rakov, Dr. William Eisenstadt, and Dr. Subrata Roy for serving as my committee members. I greatly enjoyed the lightning class taught by Dr. Rakov and the plasma physics class taught by Dr. Uman. Also, all of the RF/microwave knowledge provided by Dr. Eisenstadt will be helpful throughout my career.

I would like to extend my thanks to all of the labmates I have shared time and space with for so many years. I have shared many discussions and memories with Dr. Michael Mitchell, Dr. Danny Kotovsky, Dr. AJ Erdman, Hunter Burch, Clinton Snider, and Quincy Flint. Dr. Michael Mitchell helped me to have successful deployments, and Dr. Danny Kotovsky shared valuable insights with me, especially concerning the FEED model derivation. Dr. AJ Erdman, Hunter Burch, Clinton Snider, and Quincy Flint were great friends/colleagues throughout so many projects.

The most important people in my life are my family. My parents, 김정 and 홍정희, have always been there for me with unlimited support. I'd like to thank my sister, 김보경, who flew many times to the opposite side of the Earth to be there for me. Lastly, I would like to thank my husband, Anthony Joseph Erdman, for taking this journey together. You taught me that we can accomplish so much more together than apart. I can never thank you enough for your love and support.

Dooyoung Kim

August 2020

TABLE OF CONTENTS

LIST OF TABLES

LIST OF FIGURES

LIST OF ABBREVIATIONS

FDFD	Finite-Difference Frequency-Domain
FEED	Fluid Energetic Electron Deposition
FWHM	Full Width Half Max
GCP	Great Circle Path
GLAT	Geomagnetic Latitude
LEP	Lightning-induced Electron Precipitation
LWPC	Long Wave Propagation Capability
MC	Monte Carlo
NAV	University of Florida North American VLF array
NLDN	U.S. National Lightning Detection Network
PSD	Power Spectral Density
Rx	Receiver
SFM	Scattered Field Magnitude
SNR	Signal to Noise Ratio
Tx	Transmitter
VLF	Very Low Frequency, 3-30 kHz
WIPP	Whistler-Induced Particle Precipitation

Abstract of Dissertation Presented to the Graduate School
of the University of Florida in Partial Fulfillment of the
Requirements for the Degree of Doctor of Philosophy

ANALYSIS OF CONJUGATE LIGHTNING-INDUCED ELECTRON PRECIPITATION EVENTS USING THE VLF REMOTE SENSING METHOD

By

Dooyoung Kim

August 2020

Chair: Robert C. Moore
Major: Electrical and Computer Engineering

Lightning-induced electron precipitation (LEP) is an important loss mechanism for energetic particles in the Earth's radiation belts. Understanding the specifics of LEP processes leads to a better understanding of magnetospheric physics and impacts important societal interests such as space weather prediction. This dissertation utilizes the very low frequency (VLF, ∼3–30 kHz) remote sensing method to perform ground-based observations of *conjugate* LEP events, which are LEP events that are detected simultaneously at both ends of a geomagnetic field line. Observations are interpreted in the context of an LEP event model that simulates wave-particle interactions in space, particle deposition in the lower ionosphere, and radio wave scattering in the Earth-ionosphere waveguide.

New modeling presented in this dissertation focuses on the implementation of a fluid precipitation model (FEED). Compared to previous ionospheric deposition work based on the Monte Carlo method, the FEED model implementation decreases simulation run time by a factor of 15, and it easily runs on a desktop computer, rather than on a supercomputer. FEED simulation results accurately reproduce the results of the well-accepted Monte Carlo model for the specific application of wave-induced electron precipitation. The FEED model thus enabled the large number of simulations used to interpret the observations presented in this dissertation.

The experimental observations presented herein demonstrate that so-called *scattered field analysis* significantly impacts the interpretation of conjugate LEP events. Compared to

previous work, the much smaller interhemispheric time delays observed using scattered field analysis imply that the observed delays are not dominated by magnetospheric processes, but instead are determined by the different event detection geometries in the northern and southern hemispheres (i.e., the different spatial relationships between the developing precipitation region and the VLF signal propagation path).

Two special cases of conjugate LEP observations highlight the importance of these results. In the first case, standard poleward displacement of the precipitation is evident, and observations in *both* the northern and southern hemispheres are shown to be consistent with predictions for a non-ducted LEP event. The second case demonstrates what appears to be the first observation of radial expansion of the ionospheric disturbance from a central location, rather than poleward displacement with time. This event is interpreted as the result of precipitation produced by a *ducted* LEP event.

Together, the modeling and experimental observations presented in this dissertation demonstrate that the spatio-temporal development of LEP events critically impacts the ground-based observations that are leveraged to provide insight into magnetospheric processes. It is therefore critically important to experimentally quantify the spatio-temporal development of LEP events in order to advance the scientific understanding of important magnetospheric processes.

CHAPTER 1
INTRODUCTION

This dissertation demonstrates that the spatio-temporal development of conjugate lightning-induced electron precipitation (LEP) patches strongly impacts scattering signatures observed on very low frequency (VLF, 3–30 kHz) radio waves. Previously reported LEP observations that seemed to be in conflict with one another are re-interpreted and shown to be consistent with the presented physical explanation. As a result of this effort, it is clear that sensitivity to the spatio-temporal development of ionospheric disturbances associated with LEP (in both hemispheres) is required to successfully isolate magnetospheric effects from the effects produced by VLF propagation and scattering.

This introductory chapter provides the context necessary to understand the relevance of the scientific contributions of this work. Chapter 2 presents the LEP event model and focuses on a newly implemented fluid precipitation model for calculating electron density changes in the lower ionosphere. Chapter 3 applies scattered field analysis to LEP event onset and duration timing measurements with significantly different results than previously observed. Chapter 4 compares two conjugate LEP special cases: one which appears to result from non-ducted whistler-induced precipitation, and one which appears to result from ducted whistler-induced precipitation. At the end of Chapter 4, it will be clear how conjugate LEP event observations and statistics are affected by the type of LEP event (ducted vs. non-ducted) and by the observation geometry. Chapter 5 summarizes the contributions of this dissertation and suggests directions for future research.

1.1 The Ionosphere

The ionosphere is the ionized layer of Earth's upper atmosphere starting approximately 60 km altitude above the Earth's surface and extending up to several hundred kilometers altitude (*Mimno*, 1937; *Ratcliffe*, 1962; *Tarcsai et al*, 1988). The ionosphere is present due to the interactions between the Earth's atmosphere and the radiation from the sun – X-ray and Lyman-α emissions from the sun ionize particles faster than they recombine due to

the relatively low gas densities (*Tarcsai et al*, 1988). This partially ionized layer, also called a plasma, consists primarily of neutral particles, but contains significant enough densities of ionized particles and free electrons to affect radio propagation. The properties of the ionosphere vary significantly with time and depend strongly upon (for example) the time of day (diurnal variations), time of year (seasonal variations), geomagnetic location (latitude and longitude), solar activity, and, more generically, space weather activity.

The ionosphere is largely composed of three layers: the D- (60–100 km), E- (100–150 km), and F- (150–400 km) regions. The neutral atmospheric constituents and electron density change with height. Typical ionospheric profiles are shown in Figure 1-1. In terms of geomagnetic categorizations, the Earth is divided into three regions based upon geomagnetic latitude (GLAT): high-latitude (GLAT $> 60°$), mid-latitude ($30° <$ GLAT $< 60°$), and low-latitude (GLAT $< 30°$) (*Ratovsky et al.*, 2014). Different physical processes dominate in the different regions, and as a result, different types of studies are performed in the different GLAT zones. For example, in the high-latitude zone, studies focus on the coupling between the ionosphere and the magnetospheric tail (*Tarcsai et al*, 1988), whereas in the low-latitude zone, plasma instabilities or the magnetospheric ring current are often studied. The mid-latitude ionosphere is where most of classical ionospheric physics can be applied and modeled (*Tascione*, 1988; *Saito et al.*, 1995; *Tsunoda and Cosgrove*, 2001). This dissertation focuses on effects observed in the D-region at mid-latitudes.

Of importance to this work, an electromagnetic wave sourced at the ground can reflect from the ionosphere due to the variation of electron density with altitude (*Westcott*, 1962a,b). Reflections at the ionosphere and at the ground allow the radio signal to efficiently propagate long distances around the globe in a manner known as subionospheric propagation. Signals that efficiently propagate in this manner are roughly in the VLF frequency range (3–30 kHz)

[1] https://ccmc.gsfc.nasa.gov/modelweb/models/iri2016_vitmo.php

[2] https://ccmc.gsfc.nasa.gov/modelweb/models/nrlmsise00.php

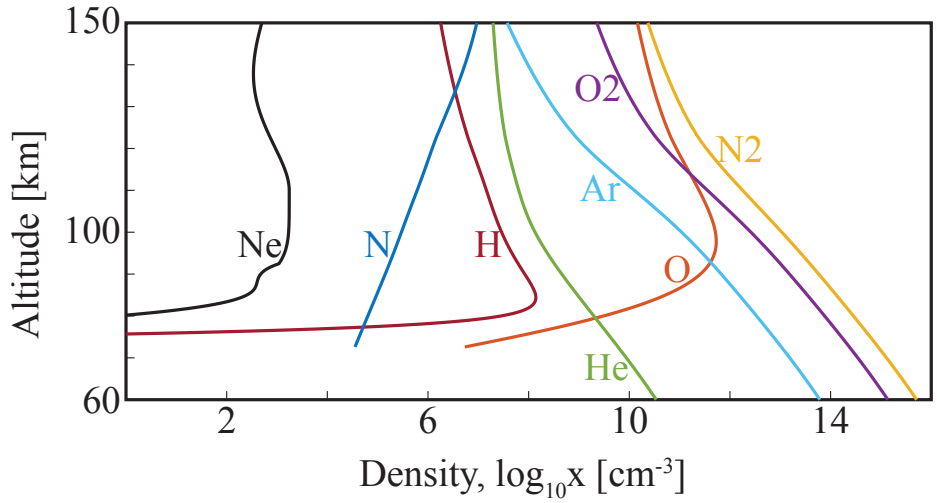

Figure 1-1. Night time electron density and neutral constituent density profiles up to 150 km altitude. Provided by IRI [1] and NRLMSISE-00 [2] models.

or below. This work focuses on measurements of man-made VLF radio signals near ∼25 kHz. The amplitude and phase of these signals vary with time in response to the electron density of the ionosphere all along the propagation path from the transmitter to the receiver. The typical reflection heights of VLF radio waves are at ∼85 km altitude during nighttime and at ∼70 km during daytime (*Cummer et al.*, 1998; *McRae and Thomson*, 2000), but they are expected to vary over shorter time scales (10–100 seconds, for instance) in response to transient ionospheric events, such as LEP events.

VLF radio waves are not entirely reflected from the lower ionsphere, however. Due to the presence of the Earth's magnetic field, the ionosphere is anisotropic and supports a whistler-mode branch of propagation (*Helliwell*, 1965). Thus, some VLF energy propagates past the nominal VLF reflection height and couples to the magnetosphere in the whistler-mode. In this manner VLF radio waves emitted by lightning can couple to the magnetosphere and illuminate the radiation belts.

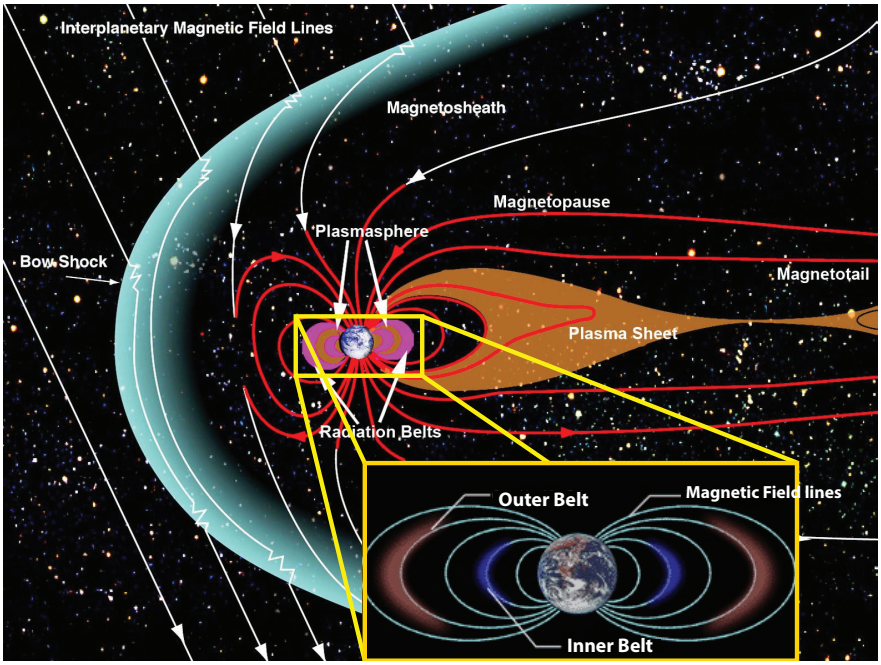

Figure 1-2. Illustration of the magnetosphere and Van Allen Radiation Belts. Reprinted with permission from NASA[3] [4]

1.2 The Magnetosphere

The magnetosphere is the region of space where the Earth's magnetic field governs the dynamics and interactions of particles and waves. The Earth's magnetic field is produced by electric currents in the Earth's core (*Walt*, 2005). The magnetosphere is located above the ionosphere starting at ∼1000 km altitude and extends outward into space. It is accurately considered a collisionless plasma, and its shape is largely dependent on the solar wind and solar activity since solar particles compress, flow around, and extend the magnetosphere at a velocity of 300-500 km/s (*Walt*, 2005). On the sun side, the solar wind compresses the Earth's magnetic field at $\sim 10R_E$ [5] , while on the night side, it extends $> 60R_E$ creating a long tail. It is an active area of research to study solar drivers and interactions with the Earth's magnetic

[3] https://www.nasa.gov/mission_pages/sunearth/science/magnetosphere2.html

[4] https://www.nasa.gov/vision/universe/solarsystem/killer_electrons.html

[5] R_E is the mean radius of the solid earth. $R_E \simeq 6370km$

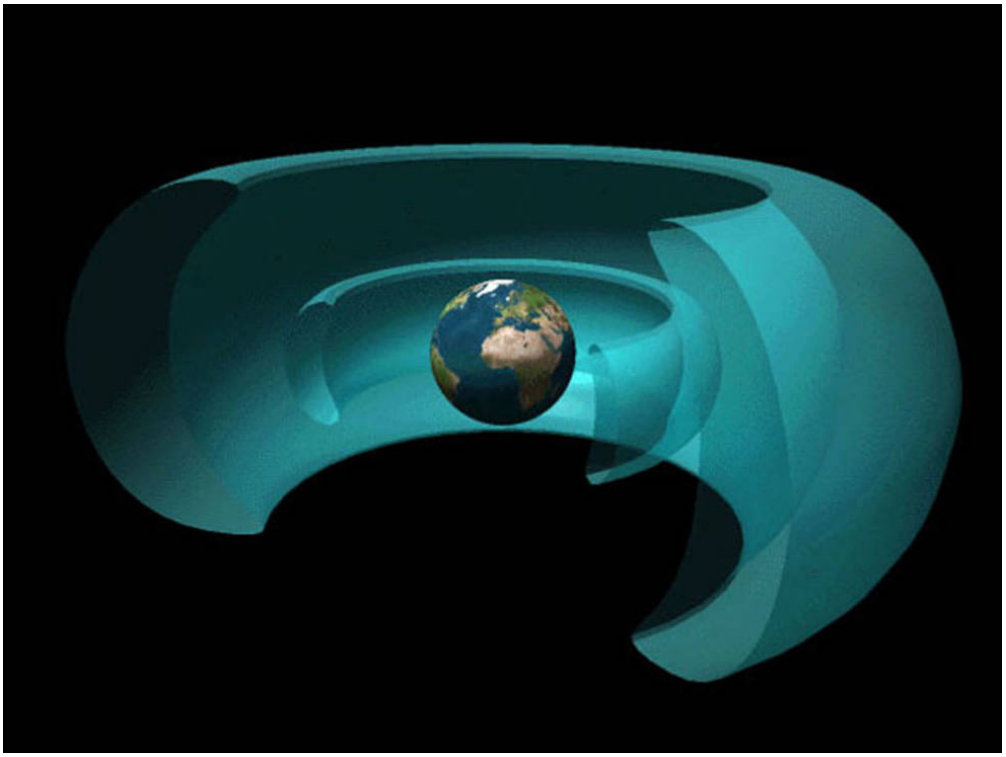

Figure 1-3. Cutaway illustration of the Earth's radiation belts, consisting of the toroidal shaped outer and inner belts. Reprinted with permission from NASA[6]

field (*Walt*, 2005; *Burch et al.*, 2016), and numerous research has been conducted using satellites (*Nishida and Maezawa*, 1971; *Faganello et al.*, 2008). Figure 1-2 is an illustration of the relevant regions of the magnetosphere.

Figure 1-3 shows an illustration of the Earth's radiation belts (*Baker et al.*, 1998; *Thorne et al.*, 2007; *Thorne*, 2010; *Reeves et al.*, 2013). The belts lie inside the inner magnetosphere region and consist of high energy particles trapped by the magnetic mirror formed by the Earth's magnetic field (*Baker et al.*, 1998). High energy particles form an inner and an outer belt, separated by a region depleted of flux known as the slot region (*Thorne et al.*, 2007). The intensity and extent of the belts are highly variable, affected by solar activity (*Thorne et al.*, 2007). The geomagnetic fields in this region are nearly dipolar fields and the field lines are

[6] https://www.nasa.gov/vision/universe/solarsystem/killer_electrons.html

closed. Locations here are routinely identified by L-shell, where L identifies the geomagnetic field line that crosses the geomagnetic equator L Earth radii (R_{E}) from the center of the Earth (*McIlwain*, 1961; *Walt*, 2005). Typically, the inner belt ranges from an L-shell of 1.1 to 2.5, the slot region from an L-shell of 2.5 to 3.0, and the outer belt from an L-shell of 3.0 to 9.0 (*Li and Temerin*, 2001). The Earth's radiation belts are composed of energetic ions and electrons ranging from keV to MeV on top of a more populous background cold plasma ($< 1\ eV$) (*Li and Temerin*, 2001). These high energy electrons and ions are thought to be continuously injected into the magnetosphere during solar events, such as solar flares or coronal mass ejections (*Li and Temerin*, 2001).

The continuous injection of energetic particles into the radiation belts is balanced by particle loss mechanisms (*Walt*, 2005). Understanding particle removal mechanisms continues to be an important research area due to the damage these energetic particles can cause to satellites and spacecraft, for example (*Rogers*, 1963). Wave-particle interactions are one key mechanism for radiation belt particle removal: stably trapped particles interact with whistler mode waves and precipitate from the radiation belts onto the ionosphere. Whistler mode waves can be introduced to the magnetosphere by different sources, such as lightning (*Helliwell et al.*, 1973; *Voss et al.*, 1984) or VLF transmitters (*Abel and Thorne*, 1998a). Electromagnetic ion-cyclotron (EMIC) waves are also an important driver for radiation belt particle loss (*Miyoshi et al.*, 2008). This study focuses on lightning generated whistler waves as the source for energetic wave-particle interactions.

1.2.1 The First Adiabatic Invariant

In the absence of external influences, radiation belt particles exhibit three types of periodic motion, which are described well by so-called *adiabatic invariants* (*Walt*, 2005). The three types of motion are: 1) helical gyration about individual geomagnetic field lines (on a timescale of 10^{-3} sec), 2) magnetic mirroring motion (due to the convergence of geomagnetic field lines) between northern and southern hemispheres (on a timescale of ~ 1 sec), and 3) slow longitudinal drift around the Earth (on a timescale of $\sim 10^{3}$ sec).

The motion of the radiation belt particles in a slowly-varying field can be determined using the adiabatic invariants. Interested readers are referred to *Jackson* (1999) and *Walt* (2005) for detailed derivations, but a brief explanation follows here.

The adiabatic invariants are obtained by the integration of the canonical momentum, **P**, over periodic orbits, as shown in Eq. 1-1.

$$J_n = \oint [m_s \mathbf{v} + q_s \mathbf{A}] \cdot d\mathbf{l} \tag{1-1}$$

where $m_s\mathbf{v} + q_s\mathbf{A}$ is the canonical momentum, **A** is the vector potential of the magnetic field and $d\mathbf{l}$ is an element of the particle orbit. The first adiabatic invariant integrates the canonical momentum around the gyration orbit path, the second adiabatic invariant integrates over an interhemispheric bounce path, and the third invariant integrates over a longitudinal drift path (i.e., an Earth orbital). The integration paths correspond to the gyration around the geomagnetic field lines, the north-south bounce path between magnetic mirror points, and the longitudinal drift around the Earth (*Walt*, 2005). The first adiabatic invariant is important in this document because it ultimately determines what is called the *pitch angle* of the particle and determines whether the particle precipitates into the ionosphere or remains stably trapped. The first adiabatic invariant, J_1, is expressed (*Walt*, 2005):

$$J_1 = \frac{p_\perp^2}{2m_{e0}B} \propto \frac{\sin^2\alpha}{B} = \text{constant} \tag{1-2}$$

where $p_\perp$ is the electron momentum perpendicular to the magnetic field, m_{e0} is the rest mass of the electron, B is the magnetic field intensity, and α is known as the pitch angle. The pitch angle, α, is the angle between the particle velocity and the magnetic field and is defined as $\alpha = \tan^{-1}(v_\parallel / v_\perp)$. The velocity components, $v_\parallel$ and $v_\perp$, are the particle velocity parallel and perpendicular to the magnetic field. Knowing the pitch angle at a reference point allows the calculation of the pitch angle at any location where the magnetic field strength is known, presuming that no energy is added to the system to move the particle to that location (i.e.,

adiabatic invariance). The pitch angle is often specified at the geomagnetic equator for which case we define the equatorial pitch angle, α_{eq}.

The Earth's magnetic field can be approximated as a centered dipole model (*Walt*, 2005) as shown in Equations 1-3 and 1-4 where r and λ are the geocentric radial distance and the latitude and R_E and B_0 are the Earth's radius (6370 km) and the mean geomagnetic field value on the equator at the Earth's surface (3.12×10^{-5} T) (*Walt*, 2005). The total magnitude (intensity) of the Earth's magnetic field at a location, (r, λ), can be evaluated through Equation 1-5.

$$B_r = -2B_0(\frac{R_E}{r})^3 sin\lambda \tag{1-3}$$

$$B_\lambda = B_0(\frac{R_E}{r})^3 cos\lambda \tag{1-4}$$

$$B(r,\lambda) = \sqrt{B_r^2 + B_\lambda^2} = B_0(\frac{R_E}{r})^3\sqrt{1+3sin^2\lambda} \tag{1-5}$$

As a particle moves down towards the Earth along a magnetic field line, the magnetic field that the particle experiences increases. For J_1 (Equation 1-2) to remain constant, the pitch angle of the particle, α, must increase as well. At altitude h_m, the geomagnetic field is large enough that the pitch angle becomes 90°, and the particle "mirrors" and returns to the magnetosphere. If this mirroring height is low enough in altitude, the neutral density of the Earth's atmosphere is large enough that the particle is highly likely to collide with the neutral constituents, dispersing its energy as heat or as ionization, and it does not mirror back to the magnetosphere. In other words, the particle is removed, or precipitated, from the radiation belts. For electron precipitation, which is the primary precipitating particle considered in this dissertation, when the electron collides with neutral molecules, the impact ionization produces additional energetic particles that continue to collide with neutral particles, in turn producing

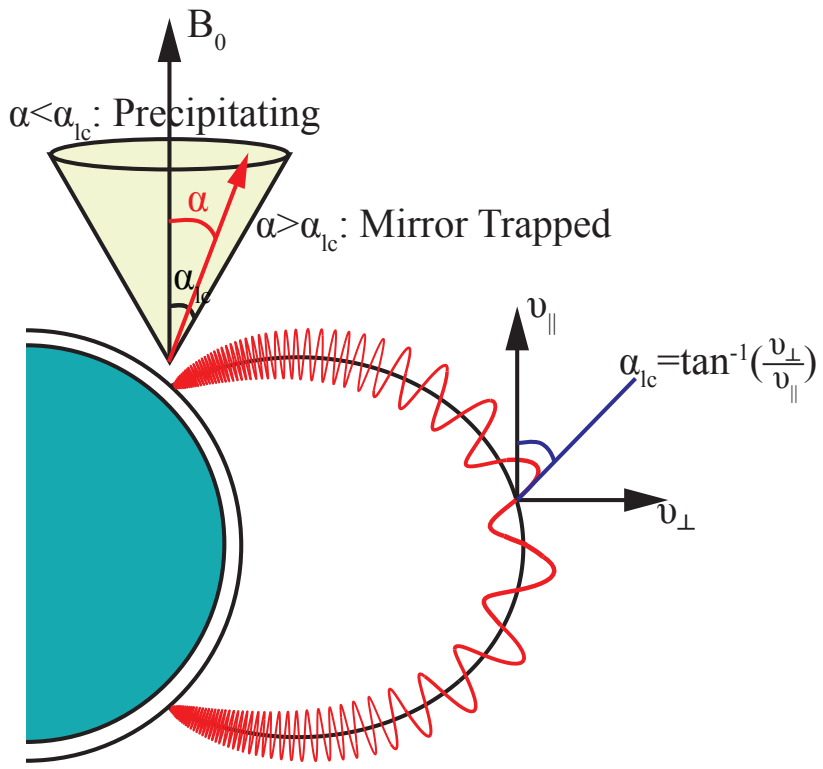

Figure 1-4. Illustration of the relationship between pitch angle and loss cone angle.

what is deemed *secondary* ionization. It is the secondary ionization patch in the ionosphere that scatters subionospherically propagating VLF radio waves.

In this work, as in others (*Bortnik*, 2005; *Cotts et al.*, 2011), the precipitating height is assumed to be 100 km altitude. If the pitch angle is 90° at $h_m = 100$ km, the equatorial pitch angle, also known as the loss cone angle, α_{lc}, is determined:

$$\sin \alpha_{lc} = \sqrt{\frac{\zeta_m^3}{\sqrt{1 + 3(1 - \zeta_m)}}} \tag{1-6}$$

where $\zeta_m = (R_E + h_m)/(R_0)$, $R_0 = LR_E$, and L is the L-shell. The equatorial loss cone angle, α_{lc}, is a useful parameter in that it easily identifies particles that will precipiatate into the ionosphere ($\alpha_{eq} \leq \alpha_{lc}$) and those that will return to the magnetosphere and remain trapped ($\alpha_{eq} > \alpha_{lc}$). Figure 1-4 illustrates the relationship between the equatorial pitch angle of a particle and the loss cone angle.

In practice, of course, the Earth's magnetic field is not perfectly dipolar, and the loss-cone-angle discussion is slightly more complicated than described above. Due to features such as the South Atlantic Anomaly, the Earth's magnetic field is asymmetric between the northern and southern hemispheres (*Laundal et al.*, 2017). Such asymmetry results in different loss cone angles for the northern and southern hemispheres. In this case, the larger of the two loss cone angles is deemed the *bounce* loss cone angle. Additionally, a percentage of the particles deemed to be precipitating by the method described above actually backscatter to the magnetosphere, rather than precipitate into the ionosphere (*Voss et al.*, 1998; *Cotts et al.*, 2011). These practicalities are thought to produce different precipitation signatures (energy and timing) at the northern and southern ends of the same geomagnetic field line (*Cotts et al.*, 2011).

1.2.2 Wave-Particle Interactions

The whistler wave that makes it to the interaction region in the radiation belts can be generated by many different types of sources: plasmaspheric hiss (*Lyons and Thorne*, 1973), lightning generated whistlers (*Dungey*, 1963; *Abel and Thorne*, 1998a), and man-made VLF transmitters (*Abel and Thorne*, 1998a; *Kulkarni et al.*, 2008). This document focuses on terrestrial lightning as a source. The lightning-launched whistler wave interacts with energetic particles and modifies the first adiabatic invariant described in the previous section (*Walt*, 2005).

The whistler wave interacts with radiation belt electrons in the equatorial region in a way that scatters the pitch angles of the stably-trapped electrons – some pitch angles are scattered higher and some are scattered lower. The electrons whose scattered pitch angles are now smaller than the loss cone angle may then precipitate into the ionosphere. The Lorentz equation can be written to accommodate the force exerted by a whistler-mode wave as shown in Equation 1-7.

$$\frac{d\mathbf{p}}{dt} = q(\mathbf{E}^W + \mathbf{v} \times [\mathbf{B} + \mathbf{B}^W]) \tag{1-7}$$

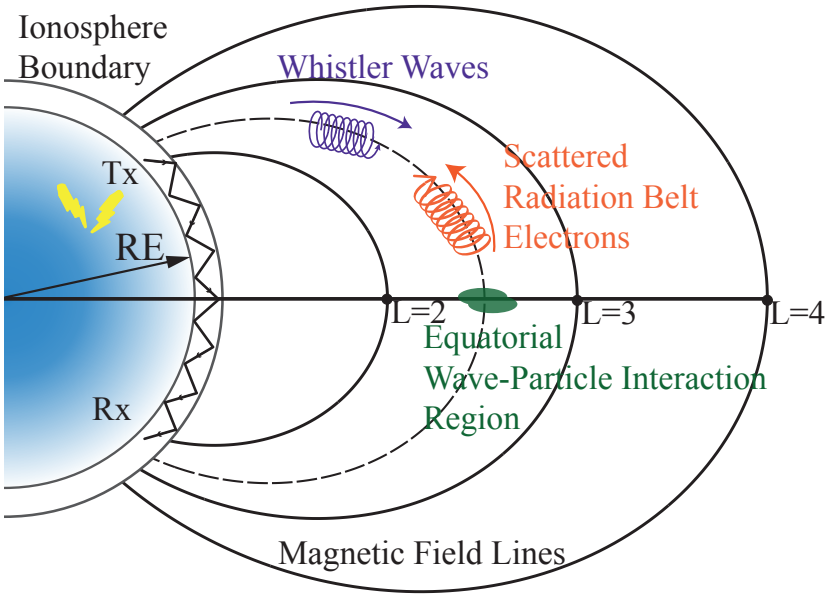

Figure 1-5. LEP Process in the ionosphere-magnetosphere view.

where $\mathbf{E}^W$ and $\mathbf{B}^W$ are the electric field and magnetic field of the whistler wave, $\mathbf{p}$, $\mathbf{v}$, and q are the momentum vector, the velocity, and the charge of the electron, and $\mathbf{B}$ is the geomagnetic field. Gyroresonance occurs when the Doppler-shifted frequency of the whistler wave (experienced by the electron) is an integer multiple of the electron gyrofrequency (*Walt*, 2005). Under this condition, the magnetic field of the whistler wave appears stationary to the electron which redirects the electron and modifies the electron pitch angle. Wave-particle interaction can also result in wave amplification (*Ashour-Abdalla*, 1972; *Chen et al.*, 2012), the triggering of emissions (*Dysthe*, 1971; *Omura and Nunn*, 2011), and wave-particle-wave interactions (*Sa*, 1990). During all of these different interactions, electrons are scattered in terms of energy and pitch angle, leading to the precipitation of at least some near-loss-cone electrons (*Chang and Inan*, 1983). Readers who are interested in the physical derivations related to gyroresonance theory are referred to *Chang and Inan* (1983), *Bell* (1984), and *Bortnik* (2005).

1.3 Lightning-induced Electron Precipitation

Using the terminology provided in the previous sections, the physical mechanisms associated with lightning-induced electron precipitation (LEP) can now be described. LEP is known

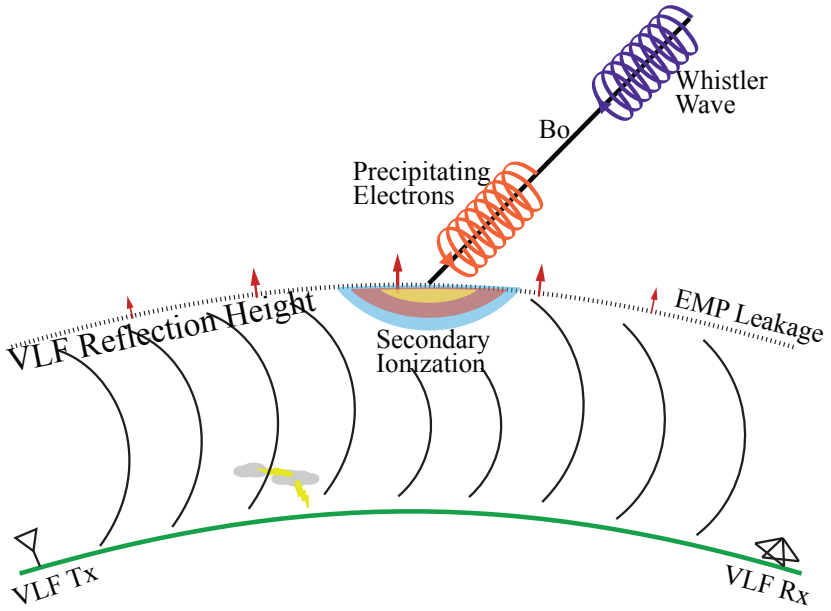

Figure 1-6. LEP Process in the Earth-Ionosphere wave guide.

to be an important natural loss mechanism for energetic radiation belt electrons, and it has been investigated in detail since it was first discovered as the VLF Trimpi effect (*Helliwell et al.*, 1973; *Voss et al.*, 1984; *Inan and Carpenter*, 1987; *Johnson et al.*, 1999; *Peter and Inan*, 2007; *Cotts et al.*, 2011; *Golkowski et al.*, 2014). The physical mechanisms that combine to produce LEP are illustrated in Figures 1-5 and 1-6. First, a terrestrial lightning discharge emits an electromagnetic pulse in a broad spectrum from below 1 Hz to above 300 MHz (*Rakov and Uman*, 2003). The low frequency ($<\sim$100 kHz) components of the lightning-generated electromagnetic wave propagate away from the source to large (1000's of km) distances, reflecting multiple times between the conducting lower ionosphere ($\sim$80 km altitude) and the conducting ground in what is known as the Earth-ionosphere waveguide (*Poulsen et al.*, 1993a). Due to the presence of the Earth's magnetic field, some portion of the lightning-emitted radio wave is transmitted through the ionosphere and couples to the magnetosphere as a whistler-mode wave (*Helliwell*, 1965). This magnetospheric whistler-mode wave continues propagating away from the Earth, but it is significantly refracted by the geomagnetic field – it propagates to equatorial

region rather than escaping into space (*Lauben*, 1998; *Bortnik*, 2005). Near the geomagnetic equator, the whistler-mode wave encounters energetic radiation belt electrons that are trapped by the magnetic mirror formed by the Earth's geomagnetic field. High energy radiation belt electrons (tens to hundreds of keV) interact with the whistler mode wave via cyclotron resonance (*Bortnik*, 2005), and some of the near-loss-cone electrons are scattered into the loss cone. This scattering results in the particles' removal from the radiation belts, also known as electron precipitation onto the ionosphere. The precipitation produces secondary ionization in the ionosphere, creating a localized and transient electron density enhancement at D-region altitudes. The transient conductivity enhancement is detected via VLF remote sensing. LEP events can often be detected at both ends of a geomagnetic field line, in which case they are termed *conjugate* LEP events. Research into conjugate ionospheric phenomena have reported such events as conjugate auroral display (*DeWitt*, 1962), conjugate airglow depletions (*Otsuka et al.*, 2002), and conjugate LEP events (*Burgess and Inan*, 1990).

LEP events have historically either been interpreted as *ducted* or *non-ducted* LEP events (*Inan et al.*, 1978, 1989; *Lauben et al.*, 1999; *Johnson et al.*, 1999; *Bortnik*, 2005). Original interpretations of LEP events typically relied upon the ducted perspective, for which the whistler wave energy follows a duct, or electron density flux tube, that necessarily lies along a single geomagnetic field line. Ground-based observations of a lightning-generated whistler are usually taken to be indicative of the presence of a duct, due to the difficulty non-ducted waves have in coupling from the magnetosphere to the Earth-ionosphere waveguide (*Inan et al.*, 1978, 1989). In the late 1990's and early 2000's, however, LEP observations were interpreted using the non-ducted perspective, for which the whistler wave propagates obliquely in the magnetosphere, refracted by the Earth's magnetic field, but not perfectly following a field line (by a flux tube, for example). The oblique propagation tends to scatter radiation belt particles at larger L-shells later in time, resulting in particle precipitation at higher latitudes as time increases. This *poleward displacement* effect was predicted by *Lauben et al.* (1999) and detected by *Johnson et al.* (1999). As a result, much of the theoretical conjugate LEP work

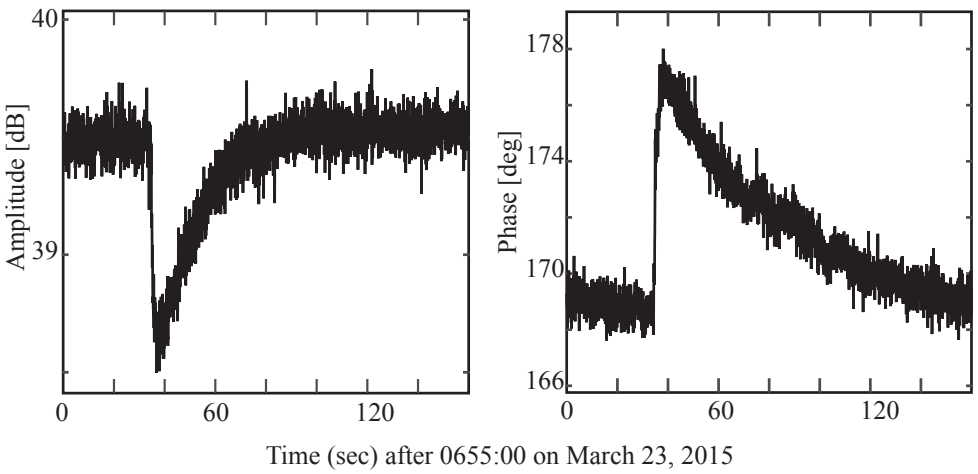

Figure 1-7. Typical transient signature of LEP event as a change of VLF amplitude (left) and phase (right) signal.

since the year 2000 has focused on the non-ducted LEP interpretation (*Bortnik*, 2005; *Peter and Inan*, 2007; *Cotts et al.*, 2011).

This dissertation determines that both ducted *and* non-ducted LEP events occur, and that they affect interhemispheric event timing observations in different ways.

1.4 VLF Remote Sensing

During the nighttime, the ambient ionization levels in the D-region ionosphere are low, which makes it easier to detect LEP-associated secondary ionization as well as other ionospheric disturbances (*Inan et al.*, 1988; *Cummer et al.*, 1998; *Kotovsky and Moore*, 2015). As depicted in Figure 1-6, the subionospheric propagation of VLF signals is sensitive to changes in the electron density of the D-region ionosphere; thus, the VLF remote sensing method has been a useful tool to probe the ionosphere and the magnetosphere remotely (*Cummer et al.*, 1997, 1998).

The VLF remote sensing method works because VLF transmitters operated by the U.S. Navy exist and operate continually around the world (*Rodriguez*, 1994). The transmitted signals can propagate to large distances around the globe, and they are a reliable stable source to probe the D-region ionosphere. University of Florida VLF receivers record the transmitted VLF waves continuously, which allows the study of the ambient and disturbed waveguide

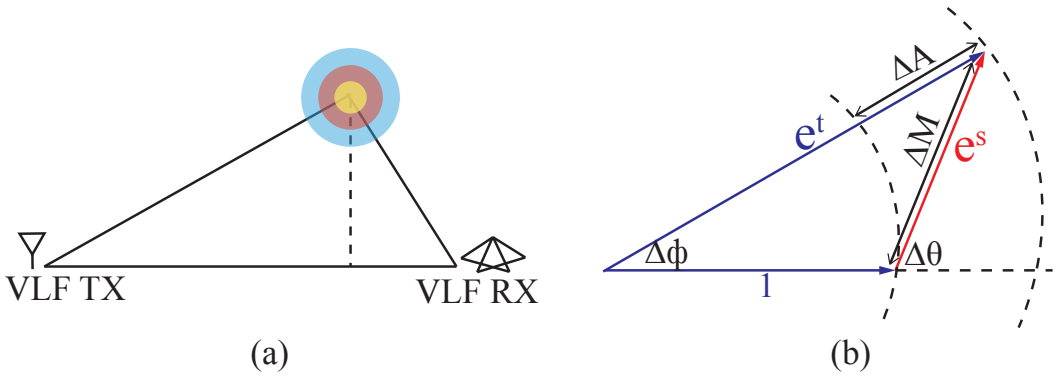

Figure 1-8. (a) the top view of the ambient, scattered, and total field with transmitter, receiver, and the disturbance. (b) Phasor diagram of normalized total and scattered field values.

properties. Because the ground conductivity remains constant with time, any changes observed by the receiver are attributed to changes in the ionospheric electron density. The receiving signal is quantified as a change of the amplitude and phase which results from ionospheric conductivity changes. Ionospheric disturbances can be caused by many different sources such as solar activity (*Thomson and Clilverd*, 2001), direct heating by lightning discharges (*Cummer and Inan*, 1997), and electron precipitations from the magnetosphere (*Helliwell et al.*, 1973) and result in the scattering of the VLF signal, among other effects. Figure 1-7 shows an example of the VLF transient signature of an LEP event. The left panel shows the amplitude change and the right panel shows the phase change during the event.

The measurements presented in this dissertation are recorded by VLF receivers operated by the University of Florida. Each receiver consists of two orthogonal triangular loop antennas that detect the tangential magnetic field, a preamplifier, a line receiver, and a 16-bit analog-to-digital converter operated by a computer. Timing is supplied by a GPS-trained oscillator with absolute timing error of 100 nsec (30 nsec-rms) and with $10^{-}12$ frequency stability. Each system exhibits a spurious-free-dynamic range of approximately 85 dB.

1.5 Scattered Field Analysis

The amplitude and phase changes shown in Figure 1-7 exhibit different event timing properties despite being created by the same ionospheric disturbance. To resolve this seeming

discrepancy, scattered field analysis is applied to the data set. During an ionospheric disturbance, the total field measured by a receiver is the sum of a direct-path (ambient) signal from the transmitter and a scattered-field signal that propagates to the receiver from the scattering body. Figure 1-8a shows a top-down-view illustration of the scattering geometry with a transmitter, a receiver, and a signal-scattering ionospheric disturbance. Figure 1-8b shows a phasor diagram representation of the amplitude and phase change (ΔA and $\Delta\phi$) of the total field (e^t) and the magnitude and angle change (ΔM and $\Delta\theta$) of the scattered field (e^s). As seen in the figure, the quantities of the amplitude and magnitude changes can be substantially different based on the properties of the ambient and scattered fields.

Poulsen et al. (1990) presented the mathematical framework for scattered field analysis. *Dowden and Rodger* (1997) and *Dowden et al.* (1997) applied scattered field analysis to LEP event recoveries, which were modeled using an exponential or logarithmic recovery fit. Event onset times and onset durations were not a concern, however, and conjugate events were not considered. Similarly, *Kotovsky and Moore* (2015) experimentally identified that early VLF events (which result from direct lightning interactions with the overlying ionosphere) exhibited different onset durations when measured using scattered field magnitude instead of the amplitude-only signal.

Scattered field analysis has not been extensively used to characterize LEP timing properties. In fact, no past works involving conjugate LEP event measurements (*Burgess and Inan*, 1990; *Cotts et al.*, 2011; *Golkowski et al.*, 2014) employed scattered field analysis – they only used amplitude observations to quantify interhemispheric timing properties. Note that *Golkowski et al.* (2014) presented both amplitude and phase change data during an LEP event but did not analyze the effect of the phase signal on interhemispheric timing.

Scattered field analysis is used throughout this dissertation, but in Chapter 3 in particular, it is theoretically and experimentally compared with amplitude-only analysis and shown to be a superior representation of the ionospheric disturbance, especially for timing difference measurements.

1.6 Relevant Past Work

Given the description of the LEP physical processes described above, this section highlights relevant past work in several areas relevant to the scientific contributions presented in this dissertation.

1.6.1 Numerical Modeling of LEP

Typically, three separate models are employed to calculate the effect of LEP on subionospherically-propagating VLF signals: 1) a particle precipitation calculator, 2) an ionospheric deposition calculator, and 3) a VLF propagation calculator.

The Whistler-Induced Particle Precipitation (WIPP) model calculates the coupling of lighting energy to the magnetosphere, the propagation of whistlers in the magnetosphere, and the scattering of energetic particles that results. It is an advancement of the Stanford VLF ray tracing code by *Inan and Bell* (1977). The original implementation was an integration of Haselgrove's equations in a tilted dipole geomagnetic field (*Haselgrove*, 1954), which was used for calculations of ducted whistler propagation (*Inan et al.*, 1978, 1989). *Lauben* (1998) improved the ray tracing code by adding oblique whistler propagation, *Bortnik* (2005) included Landau damping effects, and *Cotts et al.* (2011) used the code to couple with an ionospheric deposition code to explain precipitation backscattering effects.

A brief summary of the LEP physics in WIPP follows in order to provide a complete overview of the model. The WIPP code begins with a lightning radiation model that uses the lightning current waveform from *Cummer and Inan* (1997). The current waveform is converted to a far-field electric field (*Uman*, 1984) assuming a vertical cloud-to-ground lightning discharge. Then, a lightning wave power spectral density (PSD) at 100 km altitude is calculated (*Lauben*, 1998). This far-field PSD of the lightning is converted to PSD at 1000 km using Helliwell's absorption rates (*Helliwell*, 1965) for trans-ionospheric propagation. The wave power density is then injected as rays at 1000 km altitude, and the propagation of the ray-path is calculated in the plasmasphere. In the WIPP code, for the background cold plasma of the magnetosphere, two plasmaspheric density models are used for radial and

field-line directions. The electron density variation along the field lines is given by the diffusive equilibrium model of *Angerami and Thomas* (1964), and the radial variation is based on the work of *Tarcsai et al* (1988). A distribution of energetic electrons (hot plasma) is adapted from the AE8 radiation belt model for different L-shells (*Vette*, 1991). The pitch angle scattering of the trapped electrons in the equatorial region is calculated using the gyro-resonance condition as discussed in Section 1.2.2. As a result, the scattered pitch angle distribution is calculated for each energy and time at each L-shall value. The longitudinal dependance due to the geomagnetic asymmetry is not directly considered in the WIPP model (plasmaspheric density and loss cone do not automatically vary with longitude), although such longitudinal dependence can be accounted for by hard-coding in certain values. The output of the WIPP code provides the precipitating electron flux as a function of time and energy. The longitudinal dependence is added to the WIPP code but beyond this, it is essentially used as a black box in the dissertation.

The WIPP-calculated precipitation flux is taken as the input to an ionospheric deposition model. The state-of-the-art deposition model is known as the Monte Carlo Deposition model, which was implemented by *Lehtinen* (2000). It calculates runaway breakdown for a set of energetic electrons in an arbitrary directed magnetic field. The trajectories of the electrons gyrating around the magnetic field are calculated considering dynamic friction force, angular diffusion, and secondary ionization. The dynamic friction force (inelastic collisions) accounts for the energy lost due to excitation processes, while ionization is accounted for separately. The dynamic friction force equation that the Monte Carlo technique uses is from the Bethe theory with the Møller formula differential cross section (*Bethe and Ashkin*, 1953) (shown later in Figure 2-10). Another collision that the Monte Carlo model considers is the angular scattering of electrons colliding with nuclei. Though this collision scatters the direction of the energetic electrons minimally, this process creates the probability of new electron production. The Monte Carlo model was validated and agreed well with analytical expressions for runaway avalanche growth rates (*Lehtinen*, 2000).

The results of the electron runaway breakdown have been used to calculate sprites, gamma ray emissions, and secondary ionization, among other ionospheric effects (*Lehtinen*, 2000). *Peter and Inan* (2004) used this Monte Carlo model to calculate the secondary ionization from precipitating electron flux and determine amplitude and phase changes on a VLF signal, as further described in Section 1.6. *Cotts et al.* (2011) included the atmospheric backscatter response in the Monte Carlo model and coupled the result to the WIPP code. Atmospheric backscatter occurs when an electron is scattered to a pitch angle greater than 90° (*Cotts et al.*, 2011).

The Monte Carlo method requires large amounts of memory and long simulation times. The work presented in Chapter 2 provides a much faster implementation of an ionospheric deposition model, and the results compare well with the Monte Carlo method for the purpose of modeling wave-induced electron precipitation. Of course, the Monte Carlo model includes many physical effects not accounted for in this work, including the effect of the Earth's magnetic field, for instance, but the agreement between the models for wave-induced electron precipitation from the Earth's radiation belts indicates that neglecting these effects is a good approximation for this particular case. The output of these deposition models is the modified ionospheric electron density profile, which is in turn used to calculate VLF propagation and scattering.

VLF propagation and scattering are calculated using the 3-D implementation of the Long Wave Propagation Capability (LWPC) Code (*Poulsen et al.*, 1990). LWPC was first developed by the Naval Ocean Systems Center (*Pappert and Snyder*, 1972; *Ferguson and Snyder*, 1987) and was designed to calculate the amplitude and phase of a single-frequency wave, accounting for spatially-varying ground conductivity and ionospheric electron density profiles, as a function of distance from the transmitter along the great-circle-path (GCP) to a receiver. *Poulsen et al.* (1990) expanded LWPC's capabilities by accounting a localized disturbance in the D-region ionosphere as a scattering body. This initial improvement allowed the scattering body to be located off the GCP (a three dimensional LWPC) assuming a single-mode model. Later on,

a multiple-mode 3D LWPC code was presented by *Poulsen et al.* (1993a) and *Poulsen et al.* (1993b) to account for more realistic ionospheric and ground conductivity and permittivity changes along the propagation path. This multi-mode 3-D code uses the WKB (Wentzel, Kramers, and Brillouin) and Born approximations (*Wait*, 1964; *Born and Wolf*, 1961), limiting the electron density change to be slowly varying over a signal wavelength (*Wait*, 1964) and limiting the maximum deviation of the disturbance's electron density from ambient to be "small" (*Born and Wolf*, 1961). LWPC is employed as a black box in this dissertation in order to calculate VLF amplitudes, phases, and scattered field magnitudes at different times during LEP events.

Peter and Inan (2004) used an LEP event model similar to that described here, except a 2-D Finite Difference Frequency Domain (FDFD) VLF propgation model was used in place of LWPC. Similarly, *Cotts et al.* (2011) used the WIPP and the Monte Carlo models with backscatter effects included in an effort to reproduce their timing observations.

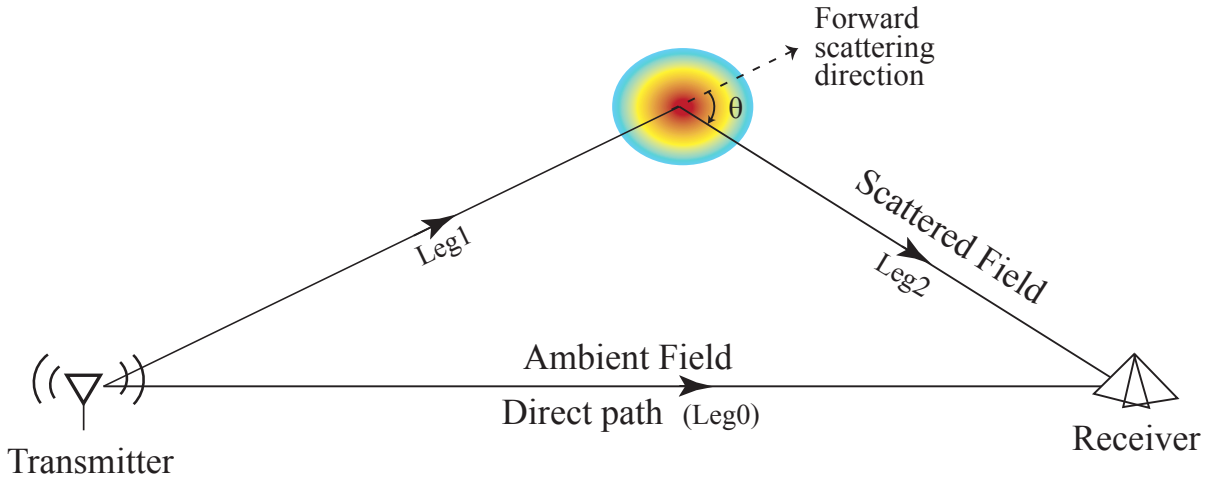

Figure 1-9. 3D LWPC top view schematic showing off GCP disturbance with a scattering angle, θ.

1.6.2 Statistical Observations of Conjugate LEP Events

Three articles address the interhemispheric timing of different aspects of conjugate LEP events detected using the VLF remote sensing method. *Burgess and Inan* (1990) presented

the first observations of conjugate LEP events. VLF signal amplitude changes associated with 129 events were simultaneously observed in the northern and southern hemispheres. The event onset delays (i.e., the time between the causative sferic and the LEP event onset) were analyzed in detail for a subset of 16 events, which were selected to represent a western group (close to Louisiana) and an eastern group (off the east coast of Maryland). In general, the LEP perturbations started $0.3 - 0.6$ seconds earlier in the southern hemisphere, but this is not the whole picture. The event onset delays in the southern hemisphere were $\sim$0.2 seconds shorter for the western group than for the eastern group, whereas the northern hemisphere onset delays did not exhibit a pronounced dependence on longitude. *Burgess and Inan* (1990) suggested that the asymmetry of the Earth's magnetic field in the vicinity of the receivers might explain the difference in onset delays, but they did not quanitatively investigate this possibility.

Cotts et al. (2011), on the other hand, did not directly observe individual conjugate LEP events. Instead, they identified the causative sferic for a large number (100's) of LEP events detected (at different times) in the northern and southern hemispheres. Two regions were selected to represent a western group (close to Colorado) and an eastern group (off the east coast of Virginia). LEP event onset delays (detected using VLF signal amplitude changes) were analyzed statistically, with the result that LEP amplitude perturbations started earlier in the southern hemisphere by $\sim$0.2 seconds; for LEP event onset delays, essentially no dependence on longitude was detected in the northern hemisphere. These observations strikingly contrast with the observations of *Burgess and Inan* (1990), which exhibited a larger change in onset delay (especially in the southern hemisphere) over a much smaller change in latitude. *Cotts et al.* (2011) also quantified the LEP event onset duration (i.e., how long the VLF signal amplitude continued to change before recovery started). LEP onset durations detected using VLF signal amplitude were shorter by $\sim$0.3 seconds for the eastern group than for the western group; southern hemisphere onset durations were essentially the same, statistically, as for the western group.

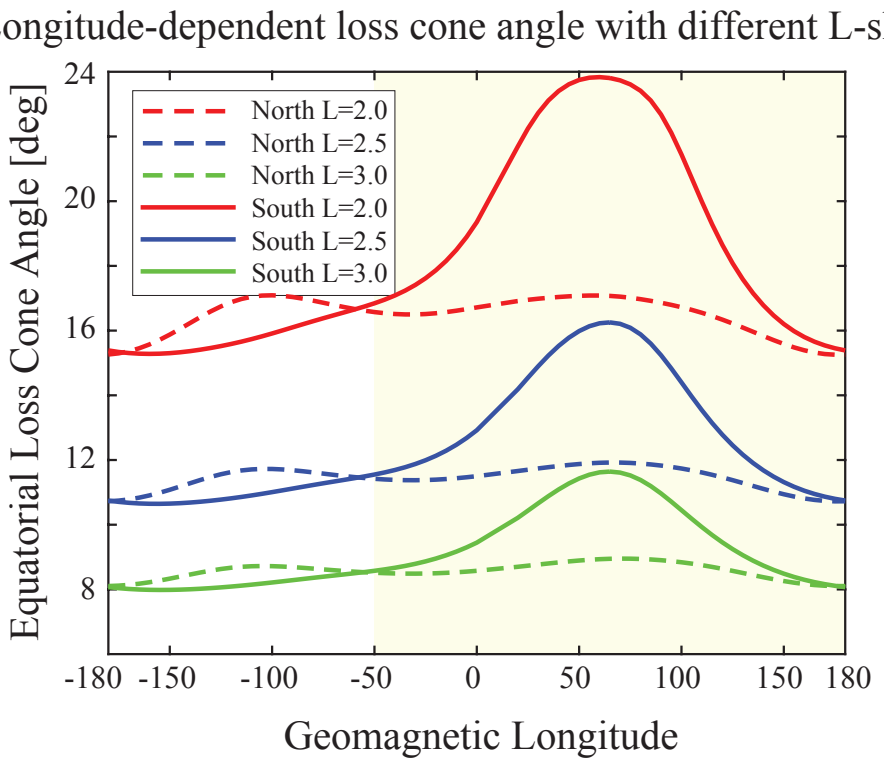

Figure 1-10. Equatorial loss cone angle dependence on longitude at L=2 (red), L=2.5 (blue), and L=3 (green) in the north (dashed lines) and south (solid lines).

Cotts et al. (2011) also attributed the event onset timing differences to the asymmetries of the geomagnetic field, and they presented a quantitative model for comparison with observations. For example, Figure 1-10 illustrates the bounce loss cone dependence on the geomagnetic longitude for different L-shells. In the highlighted section of geomagnetic longitude, stably-trapped electrons would scatter into the southern hemisphere bounce loss cone before they would scatter into the northern hemisphere bounce loss cone, resulting in an earlier event onset in the southern hemisphere. These predictions are in general agreement with the statistical observations presented by *Cotts et al.* (2011), but they are not consistent with the observations presented by *Burgess and Inan* (1990). Based on the southern hemisphere bounce loss cone values shown in Figure 1-10, western events (Louisiana) observed in the southern hemisphere should exhibit longer LEP event onset delays than eastern events (Maryland), which is opposite that observed by *Burgess and Inan* (1990).

Lastly, *Golkowski et al.* (2014) presented 3 conjugate LEP events simultaneously measured in the northern and southern hemispheres, but only analyzed the LEP events using VLF amplitude (i.e., the authors did not analyze the phase of the LEP events or present a scattered field analysis of the LEP events). The events occurred off the east coast of Virginia. The authors' interpretation of the observations were consistent with the statistical analysis presented by *Cotts et al.* (2011): the southern hemisphere LEP event preceded the northern hemisphere LEP event by ∼0.2 seconds due to the asymmetry of the Earth's magnetic field. The observed LEP onset durations were not significantly different in the two hemispheres, conflicting with 0.3-second differences presented by *Cotts et al.* (2011) for their eastern (Virginia) observations.

The experimental observations presented in Chapter 3 significantly contribute to the conjugate LEP event database – 46 conjugate LEP events are simultaneously detected in the northern and southern hemispheres. By applying scattered field analysis to the conjugate LEP events, simultaneously incorporating both the amplitude and phase signatures, at least some of the timing discrepancies discussed above are explained.

1.6.3 Evolution of Ducted and Non-Ducted LEP Events

Prior to the works of *Lauben* (1998) and *Johnson et al.* (1999), LEP modeling focused on the ducted LEP interpretation. The multi-mode 3-D LWPC code was used to interpret events occurring offset from the GCP. Figure 1-9 shows the diagram of the 3D scattering LWPC model with a disturbance located off of the GCP. It was found that the scattered field has a strong dependance on the altitude profile of the disturbance, while it is independent of the ground conductivity and permittivity (*Poulsen et al.*, 1993b). The scattering pattern is strongly focused in the forward direction: the magnitude of the scattered field reduces significantly past 20° scatter angle, which is converted to 200 km offset from the GCP (*Poulsen et al.*, 1993b). For a GCP up to 6000 km, a disturbance with a radius between 50 km and 200 km significantly scatters if it is located within 200 km of the GCP (*Poulsen et al.*, 1993b). Interestingly, *Poulsen et al.* (1993b) showed that the scattered field magnitude (SFM) increased with increased disturbance radius, and decreased with distance from the propagation

path. *Poulsen et al.* (1993b) did not consider that the radius or the center location of the ducted LEP event could be changing with time, however. If the location and radius are constant with time, normalized changes in amplitude and in scattered field magnitude typically result in the same trace (and therefore the same onset time and onset duration) no matter where the receiver is located, with the only exception occurring when a strong modal null affects the received signal.

As is shown in Chapter 2, changing the radius of the ionospheric disturbance with time, and by inference changing the location of the center of the disturbance with time, significantly modifies the perceived onset delay and onset duration of a modeled LEP event by modifying the maximum deviation from its ambient values.

Theoretical predictions about LEP spatial development were presented in previous works (*Lauben et al.*, 1999; *Bortnik et al.*, 2006a,b), using the WIPP code, assuming non-ducted oblique whistler propagation. The left panel of Figure 1-11 illustrates the trace of oblique whistler rays in the magnetosphere calculated by the WIPP code. It is seen that the rays traverse the magnetic field lines to the higher L-shells in the magnetosphere. Based on the projected propagation of the oblique whistler rays, the model prediction of a distribution of the precipitating energy flux is shown in the right panel of Figure 1-11. The right panel is plotted for L-shell values (L =2.4, 2.6, 2.8, and 3) across time. As shown in Figure 1-11, the precipitation occurs progressively later at higher L-shell values, which indicates the poleward movement of the non-ducted electron precipitation.

Johnson et al. (1999) and *Peter and Inan* (2004) experimentally tested the theoretical prediction of the poleward displacement of LEP. *Johnson et al.* (1999) observed LEP events using nine VLF receivers located at the same longitude but increasing latitudes. With the LEP observations, they presented that LEP events exhibited the increase in onset delay with increasing path latitude or L-shell value. The precipitation with more onset delay was observed at the higher latitude because it was caused by the non-ducted whistler propagating to the higher L-shell in the magnetosphere.

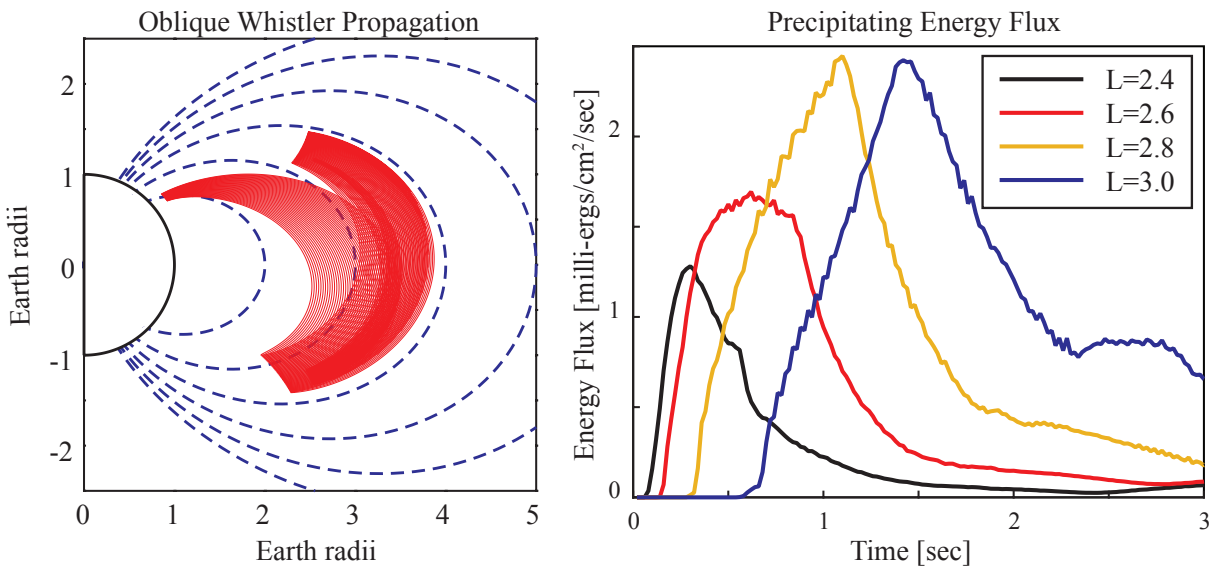

Figure 1-11. WIPP results of oblique whistler propagation in the magnetosphere (left) and precipitating flux at different L-shells (right).

While *Johnson et al.* (1999) made the first experimental observations of non-ducted LEP events, *Peter and Inan* (2004) used an LEP event model similar to that described in the previous section to interpret observations of non-ducted LEP events. The experimental observations demonstrated increasing onset delay and duration with increasing latitude. The VLF propagation modeling used a 2-D implementation and successfully reproduced much of the poleward displacement observations.

Cotts et al. (2011) used the WIPP and the Monte Carlo models with backscatter to interpret their observations. Their experimental statistics were therefore interpreted using non-ducted LEP theory. They used the calculated incoming flux from WIPP to quantify backscatter effects using the Monte Carlo model. By combining the two models with the backscatter effects, they predicted the southern hemisphere would onset earlier than the northern hemisphere by ~0.2 seconds. The hypothesis was that the particles are half-trapped in north on the first bounce, they transverse to the southern hemisphere where particles precipitate first, and then backscatter to the northern hemisphere.

Experimental observations and theoretical modeling of non-ducted LEP events is thus well established in the literature. Chapter 4 of this work shows conjugate non-ducted LEP events and demonstrates that the event timing is as expected in both hemispheres based on previous work. Other than this one non-ducted LEP event, this dissertation focuses on modeling ducted LEP events, and in particular modeling the dependence of the perceived onset time and duration based on changing the radius of the LEP disturbance in relation to the great circle path of the VLF radio wave.

1.7 Organization of the Dissertation

The following chapters of this dissertation are organized as follows.

Chapter 2 presents a newly implemented electron deposition model (FEED) that computes the interaction of precipitating electrons with the neutral atmosphere. LEP event modeling is produced by combining WIPP, FEED, and LWPC models. Example simulations of the combined models are presented for varying disturbance properties.

Chapter 3 presents a statistical analysis of conjugate LEP events comparing amplitude-only observations and scattered field magnitude observations.

Chapter 4 discusses two experimental observations of conjugate LEP events that exhibit different spatio-temporal development signatures. The cases are interpreted as demonstrating that non-ducted LEP events exhibit different timing signatures than ducted LEP events.

Chapter 5 summarizes the scientific contributions of this dissertation and makes suggestions for future areas of research.

1.8 Scientific Contributions

The scientific contributions of this work are as follows:

1. A new fluid model for energetic electron deposition in the D-region ionosphere for electron energy ranges between 400 eV to 1 MeV is developed and validated by comparison with a well accepted Monte Carlo deposition model. The model calculates secondary ionization production in the ionosphere as a function of precipitating electron energy and time. The implementation runs 15 times faster than contemporary models.

2. The inter-hemispheric timing of conjugate LEP events is demonstrated to be significantly different if measured using scattered field analysis, rather than amplitude-only analysis,

which was employed by all previous analyses of conjugate LEP events. Inter-hemispheric onset time differences are shorter using scattered field analysis and as a result cannot be attributed to changing bounce periods or precipitation backscattering effects.

3. LEP events exhibiting characteristically different spatio-temporal profiles are identified and attributed to ducted and non-ducted LEP events. LEP event observations thus depend strongly on the transmitter-receiver observation geometry and the spatio-temporal development of the event itself.

CHAPTER 2
FEED AND LEP EVENT MODELING FRAMEWORK

This chapter presents and discusses the methodology to combine three numerical models in order to accurately simulate lightning-induced electron precipitation events. In this work, the LEP processes are divided into three steps and each model accounts for different parts of LEP event physics. The combination of the three codes is used to explore more realistic simulation results and to examine the spatial and temporal developments of electron precipitation. The modeling results are compared with experimental LEP observations reported in Chapter 3 and Chapter 4.

Chapter 1 introduced and described the ray tracing particle precipitation code (WIPP) (*Inan et al.*, 1978, 1989; *Lauben*, 1998; *Bortnik et al.*, 2006a; *Cotts et al.*, 2011) and highlighted the details of 3D LWPC model (*Pappert and Snyder*, 1972; *Ferguson and Snyder*, 1987; *Poulsen et al.*, 1990, 1993a,b) that calculates the VLF scattering produced by an LEP-related ionospheric disturbance. This chapter focuses on the development of a new energetic electron deposition model and the incorporation of that model with the two other models.

Section 2.2 provides details on longitudinal effects of loss cone angle in WIPP, Section 2.3 introduces a newly-implemented FEED model with comparisons to a Monte Carlo model, Section 2.4 presents 3D LWPC utilization for transient LEP scattering, and finally in Section 2.5, the combination results of the models with a sample simulation are shown.

2.1 LEP Event Modeling Framework

As described in Chapter 1, three numerical models are employed to model LEP events detected using VLF remote sensing. Figure 2-1 illustrates the framework consisting of the three models that are Whistler-induced particle precipitation (WIPP) model (*Lauben*, 1998; *Bortnik*, 2005; *Cotts et al.*, 2011), Fluid Energetic Electron Deposition model (FEED, developed herein), and the Long Wave Propagation Capability (LWPC) code (*Pappert and Snyder*, 1972; *Ferguson and Snyder*, 1987; *Poulsen et al.*, 1990, 1993a). First, the WIPP code is utilized to model the initial part of the LEP process. It models the electromagnetic radiation from a

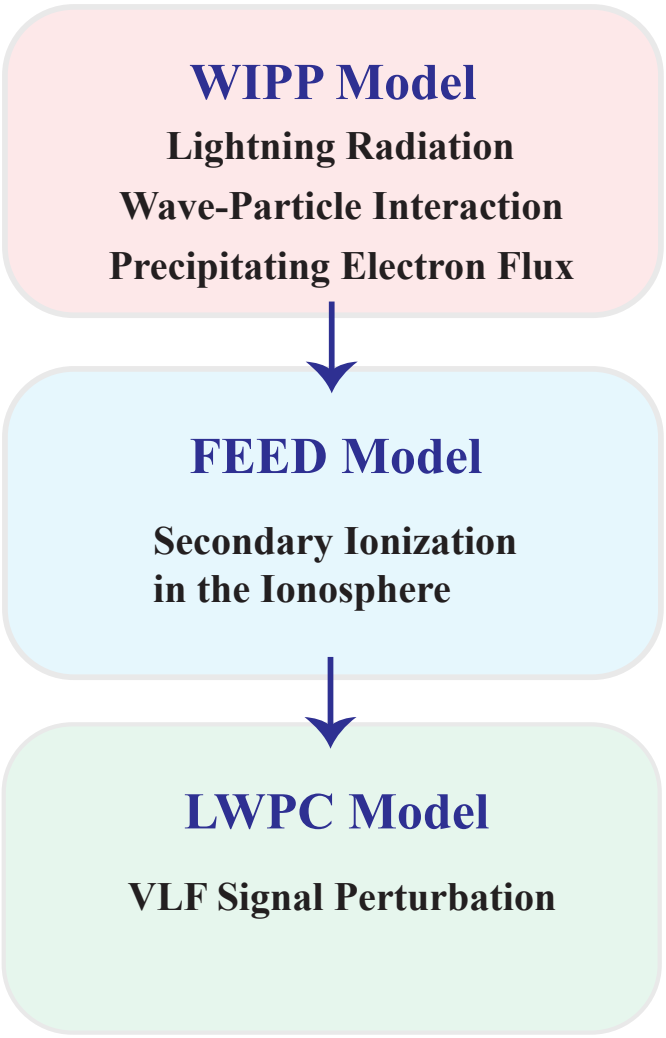

Figure 2-1. Flowchart of the LEP modeling framework. The framework is divided into three major blocks which are WIPP, FEED, and LWPC models.

lightning return stroke with user-selected rise-times, fall-times, peak currents, and lightning channel lengths, and it calculates the power spectral density of the lightning radiation at the top of the ionosphere. The WIPP code then computes the whistler energy interaction with trapped particles to quantify pitch angle scattering in the equatorial region and energy flux propagating into the ionosphere, instead of remaining trapped in the magnetosphere. Second, the calculated incoming flux into the ionosphere is input into the newly implemented FEED model. The FEED model accounts for secondary ionization in the ionosphere, resulting from

the interaction of precipitating electrons with the neutral atmospheric constituents. This model is validated in Section 2.3.3 using a separately validated Monte Carlo Deposition model (*Lehtinen*, 2000) that has been widely used (*Peter and Inan*, 2004; *Cotts et al.*, 2011). Lastly, the resulting electron deposition profiles calculated as a function of time are sequentially fed into the LWPC VLF propagation code in order to calculate perturbations on VLF transmitter signals with respect to a transmitter-to-receiver GCP. The three models are chosen for their proven and leading capabilities to simulate each stage of the LEP process. Details of WIPP and LWPC were introduced in Chapter 1. Additional aspects of WIPP and LWPC follow in this chapter along with a detailed explanation of the FEED model.

2.2 WIPP: Longitudinal Dependance of Loss Cone Angle

The current WIPP model does not automatically account for the longitudinal dependence of the loss cone angle due to the asymmetry of the geomagnetic field. Because the current WIPP model is written in 2-dimension (latitudinal and vertical), the loss cone angle that decides whether a particle precipitates or remains trapped is only a function of L-shell. This section describes how the loss cone dependence on longitude is accounted for.

The equation for the equatorial loss cone angle is reproduced here (Equation 2-1):

$$\sin(\alpha_{lc}) = \left[\frac{\zeta_m^3}{\sqrt{1+3(1-\zeta_m)}}\right]^{1/2} \tag{2-1}$$

where $\zeta_m = \frac{R_E+h_m}{R_o}$, R_{E} is the earth radius (6370 km), h_{m} is the mirroring height, and $R_o = LR_{\mathrm{E}}$ is the distance to the L-shell field line (L) at the equator. The equatorial loss cone angle as a function of L-shell is plotted in Figure 2-2.

Figure 2-3 shows the equatorial loss cone angle as a function of geomagnetic longitude at L-shells of 2, 2.5, and 3 in both northern and southern hemispheres overlaid on top of one another. The magnetic field, L-shell, and geomagnetic longitude values are taken from

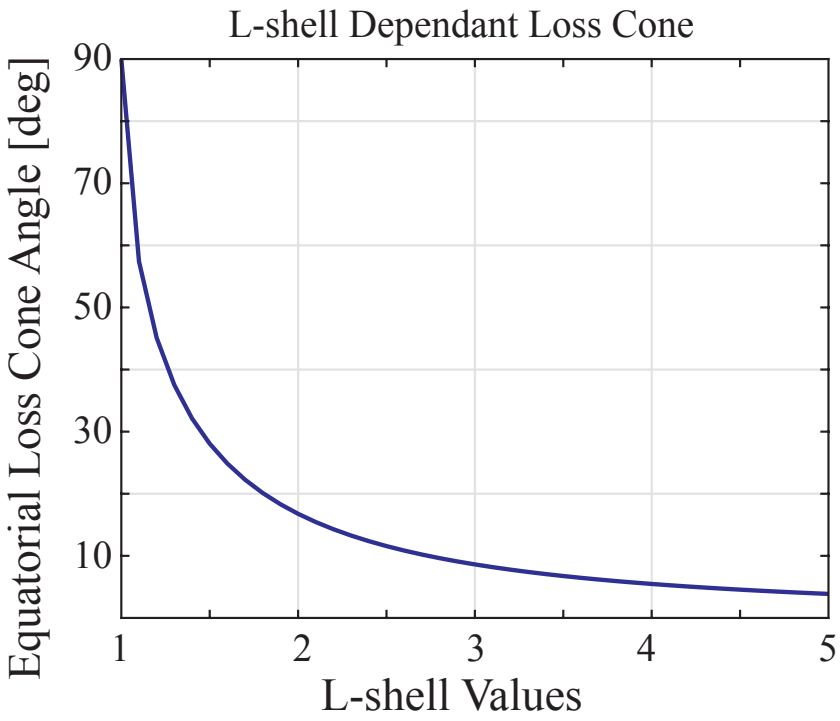

Figure 2-2. L-shell dependent loss cone angle as calculated by WIPP assuming dipole moment.

IGRF/DGRF model[1] for 2011. More detailed plots of the equatorial loss cone angle with longitudinal dependence are shown in Figure 2-4 for the northern hemisphere and Figure 2-5 for the southern hemisphere. With the large numbers of L-shells considered in these figures, it is difficult to overlay the northern and southern hemisphere plots, and so they are provided separately for reference.

In the western hemisphere, the southern equatorial loss cone angles are larger than the northern loss cone angles. The eastern United States is located at ~0 degrees of geomagnetic longitude. For example, at 0 degrees longitude and L=2.5, the equatorial loss cone angle in the northern hemisphere is 11.5° and 12.9° in the southern hemisphere, according to Figure 2-3.

The southern loss cone angles peak near 60° geomagnetic longitude (due to the South Atlantic Anomaly), while both northern and southern loss cone angles exhibit minima near

[1] https://omniweb.gsfc.nasa.gov/vitmo/cgm.html

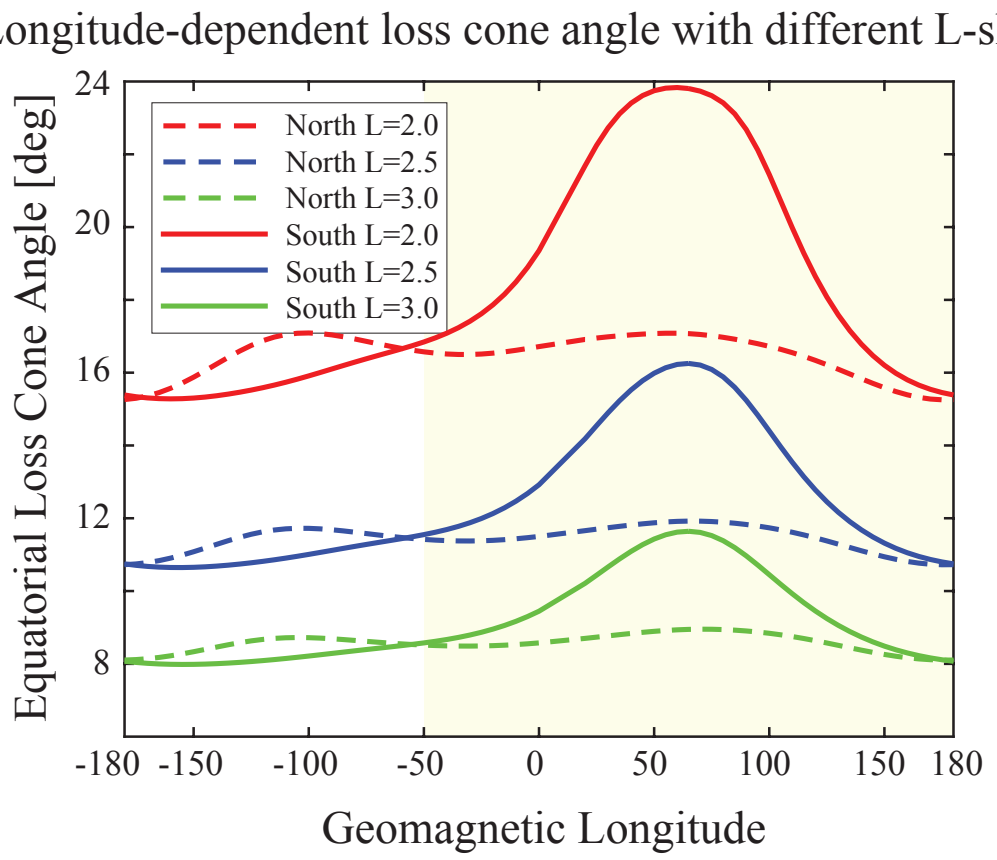

Figure 2-3. Equatorial loss cone angle dependence on longitude at L=2 (red), L=2.5 (blue), and L=3 (green) in the north (dashed lines) and south (solid lines).

180° for all the L-shells. To analyze the largest difference caused by the longitudinal effects on the loss cone angles, the equatorial loss cone angle at 60° and 180° geomagnetic longitudes are chosen and plotted as a function of L-shell in Figure 2-6. The largest equatorial loss cone at 60° geomagnetic longitude was 16° and the smallest equatorial loss cone at geomagnetic longitude of 180° was 11°, both at $L = 2.5$. The default loss cone angles as a function of L-shell follow very closely to the northern loss cone angle, both at 60° geomagnetic longitude (left panel) and at 180° (right panel). Comparing the default loss cone angle with the southern loss cone angle at 60° geomagnetic longitude, there is a maximum 9° difference at $L = 1.5$, and there is a 5° difference at $L = 2.5$, as shown in Figure 2-6. The right panel of Figure 2-6 provides a comparison at 180° geomagnetic longitude: the northern and southern equatorial loss cone angles are very close to the default loss cone value, with 0.8° difference at $L = 2.5$.

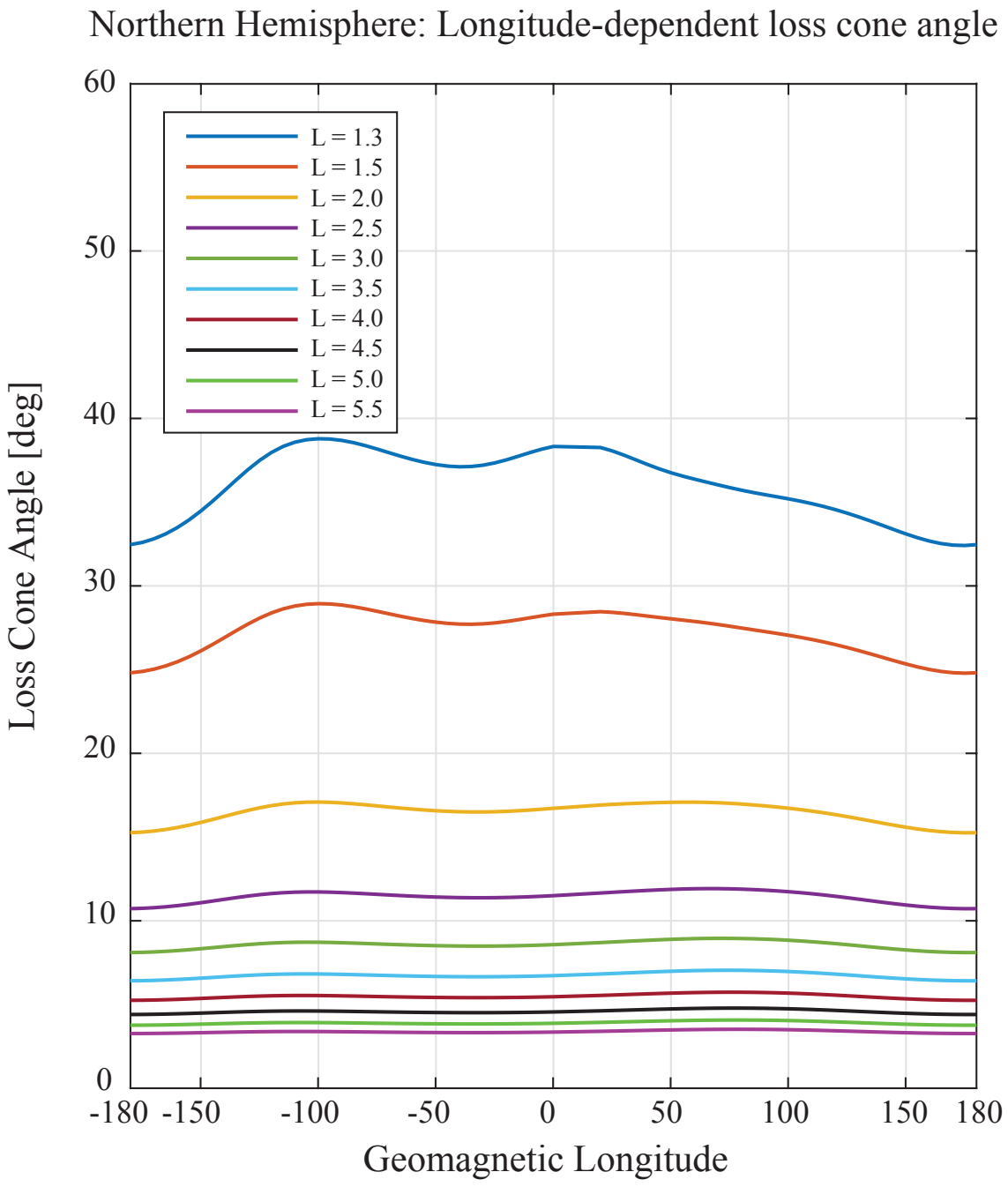

Figure 2-4. Loss cone angle dependence on longitude at L values between 1.3 and 5.5 in the northern hemisphere

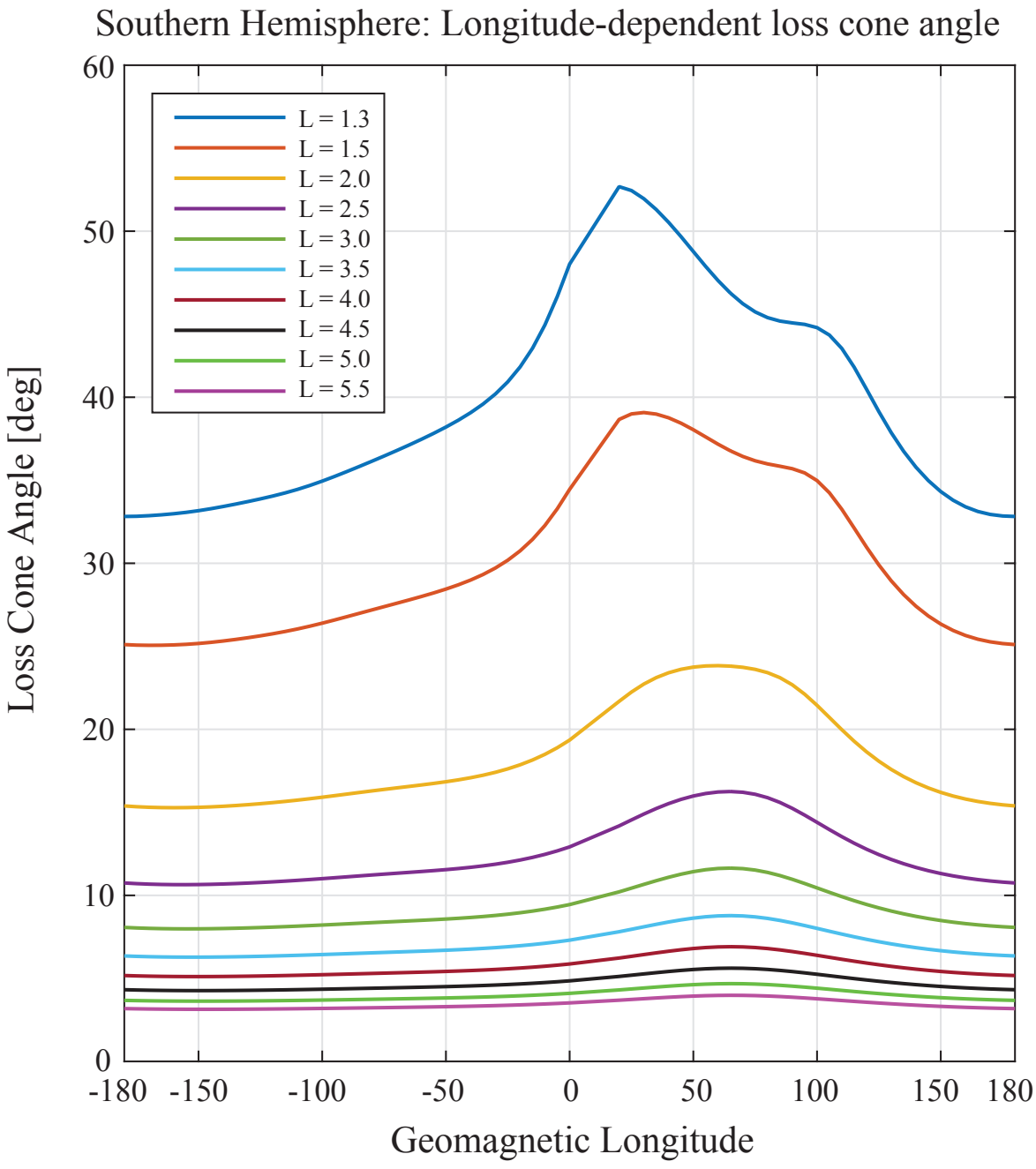

Figure 2-5. Loss cone angle dependence on longitude at L values between 1.3 and 5.5 in the southern hemisphere

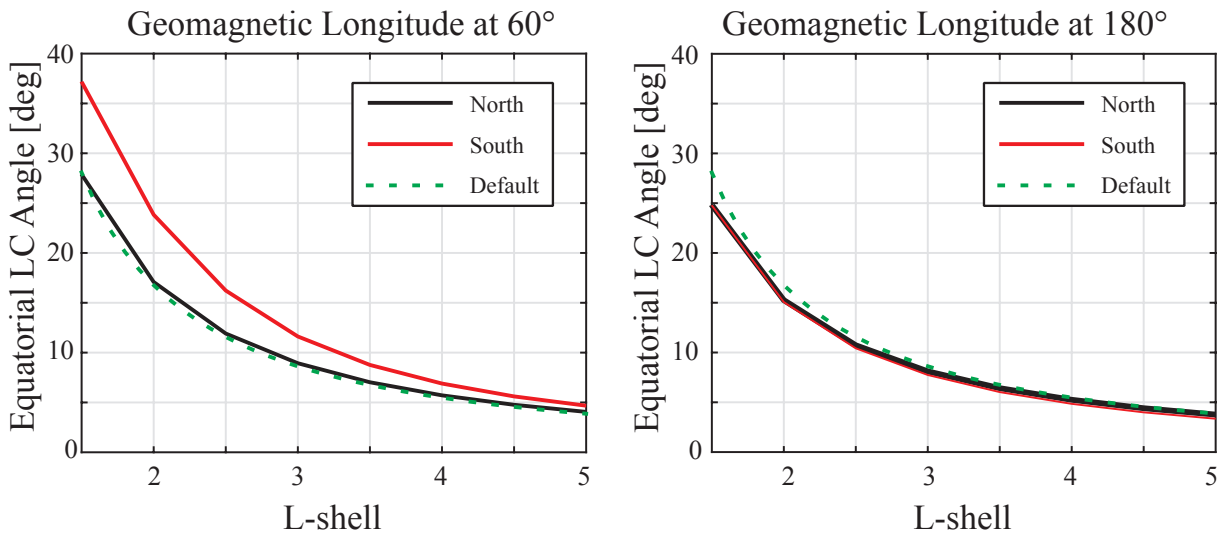

Figure 2-6. Equatorial loss cone angle over different L-shells with longitude effects.

Incorporating the longitudinal dependence of the equatorial loss cone angles causes changes in two main parts of WIPP code. First, it affects the bounce period (i.e., flight time constant) of a particle between mirror points of both hemispheres, which may affect the relative onset time between the conjugate points. Second, it affects the amount of flux that precipitates to the ionosphere. The approximate formula of the bounce period (τ_b) is shown in Equation 2-2 (*Walt*, 2005). Figure 2-7 plots Equation 2-2 showing the bounce period as a function of equatorial loss cone angle (α_{lc}) at L-shells of 2.0, 2.5, and 3.0. The black squares on the figure are the bounce period using the default equatorial loss cone and the red squares use the southern hemisphere equatorial loss cone at 60° geomagnetic longitude (left panel of Figure 2-6). According to Equation 2-2 and Figure 2-7, the change in the bounce period caused by the maximum longitudinal dependance at $L = 2.5$ is ~20 msec. This minimal change confirms the statement by *Walt* (2005) that geomagnetic longitude impacts the bounce period minimally.

$$\tau_b = 0.117 \frac{R_0}{R_E} \frac{1}{\beta} [1 - 0.4635(\sin(\alpha_{eq}))^{3/4}] \tag{2-2}$$

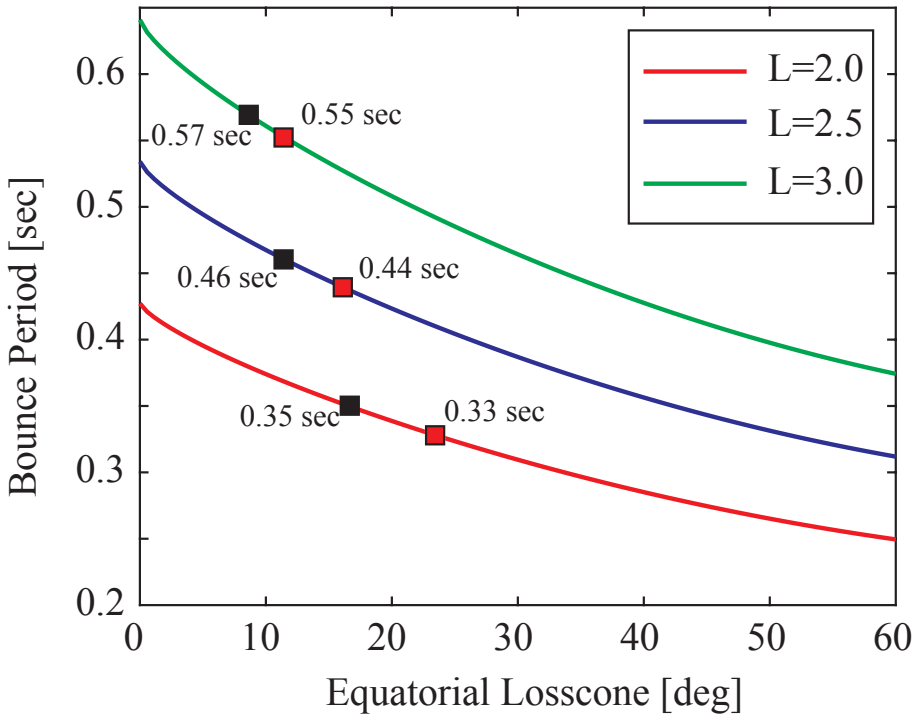

Figure 2-7. Bounce period change over loss cone angle in different L-shell values.

However, the longitude dependence of the equatorial loss cone angle significantly affects the amount of precipitating flux. Because the realistic loss cone angle is larger than the originally modeled loss cone angle, it allows more particles to precipitate. Figure 2-8 shows the simulation results of the precipitating energy flux (an output of WIPP code) at $L = 2.4$ with the equatorial loss cone angle at geomagnetic longitude of 60° and the WIPP code default equatorial loss cone angle. The peak magnitude of the energy flux is larger by 42% and the onset is earlier by 20 msec with the the realistic loss cone angle than with the latitudinal-only loss cone angle. These effects are now automatically included in WIPP.

2.3 Fluid Energetic Electron Deposition

WIPP predicts the projected propagation of whistlers and produces an energy-time distribution of precipitating electrons in the ionosphere. The calculated precipitating flux at 200 km altitude is subsequently input into the Fluid Energetic Electron Deposition (FEED) model. The FEED model is implemented to calculate the additional ionization caused by

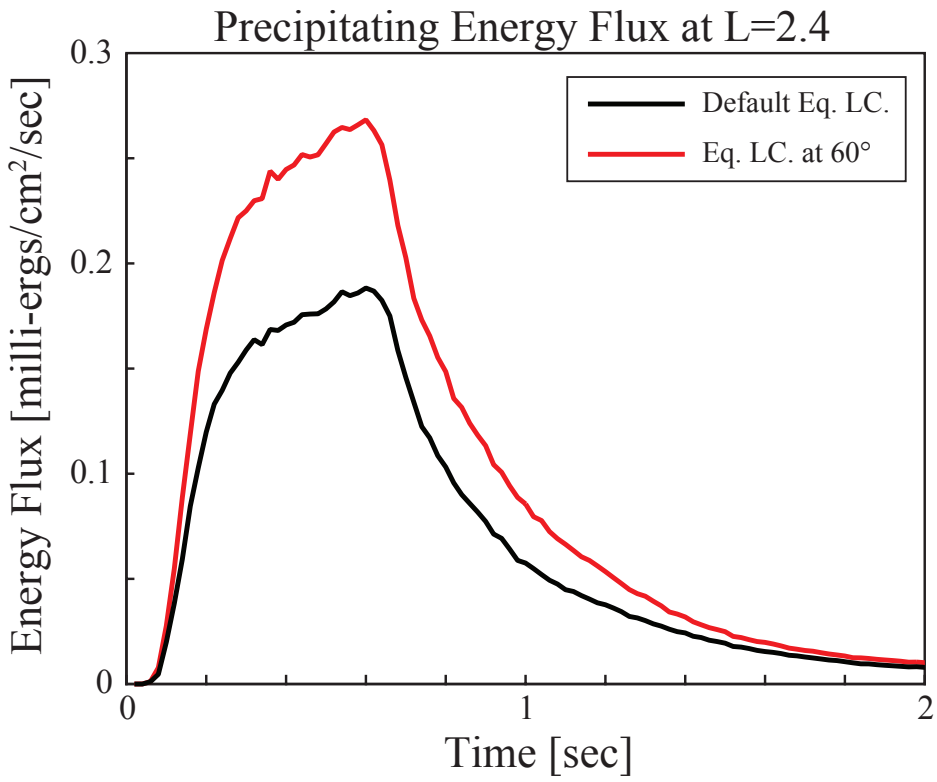

Figure 2-8. Precipitating flux change due to realistic Loss cone angle.

the precipitating particles on the ionosphere, also known as secondary ionization. Figure 2-9 is an illustration for the relationship between the WIPP and the FEED models. Figure 2-9a illustrates the process by which precipitating flux produces secondary ionization in the ionosphere and scatters subionospherically propagating VLF radio waves. The distribution of the incoming precipitating electrons is modeled with the WIPP code as shown in Figure 2-9b, which shows the energy-time spectrogram for the particle flux. Figure 2-9c is an example of the FEED model output calculating the electron density change due to the secondary ionization of the disturbance.

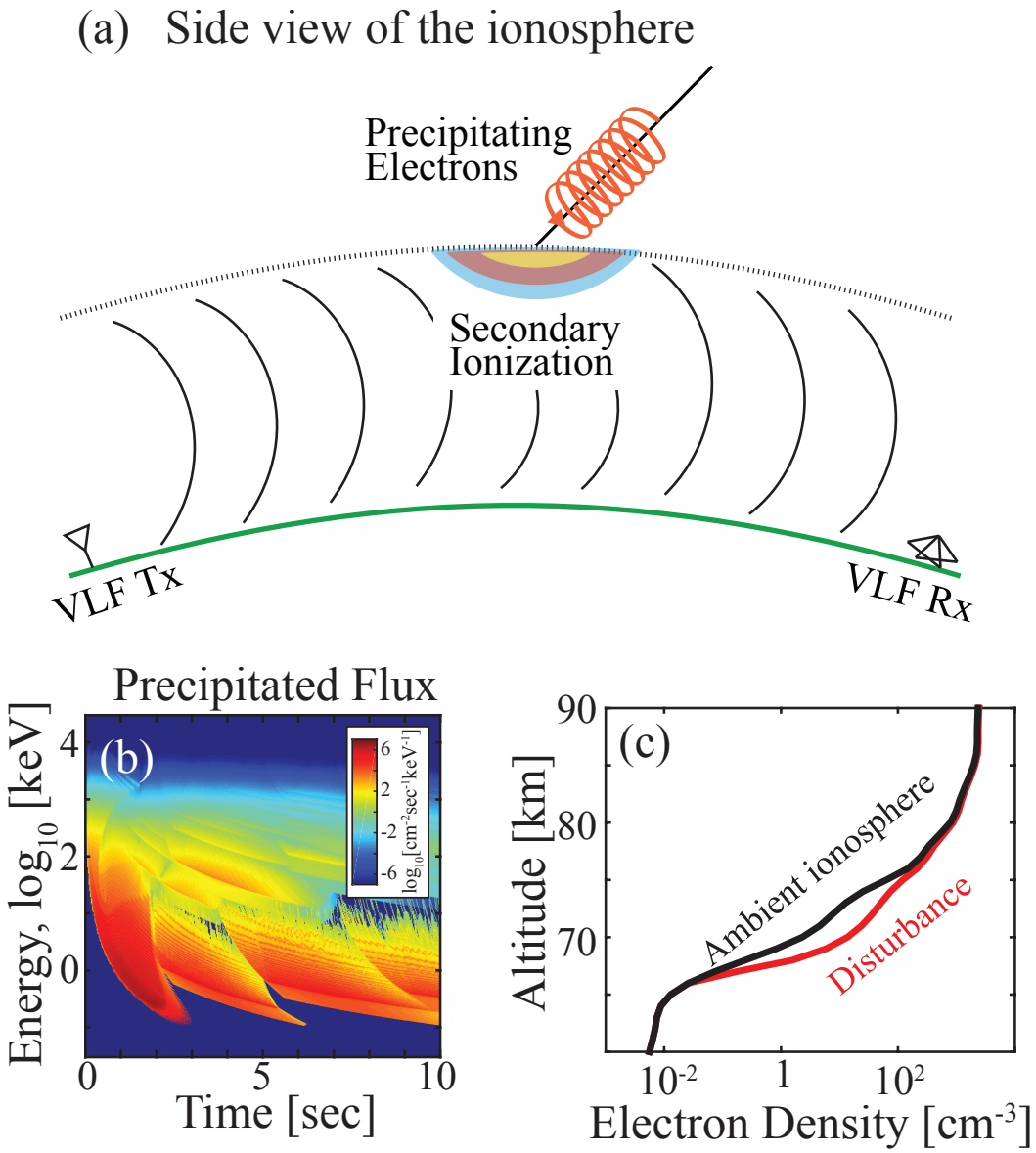

Figure 2-9. Illustration of the secondary ionization. (a) The side view of the ionosphere with precipitating electrons creating a secondary ionization patch affecting the ionosphere reflection height. (b) The incoming precipitated flux as a function of energy and time, as determined by WIPP. (c) An example of the electron density change due to the secondary ionization of the disturbance, calculated by the FEED model.

2.3.1 FEED Model Derivation

Prior to deriving the FEED model equations, it is useful to review several basic relativistic relationships. The kinetic energy of a relativistic particle is expressed:

$$E = E_R \left[\frac{1}{\sqrt{1 - \left(\frac{v}{c}\right)^2}} - 1 \right] \tag{2-3}$$

where $E_R = m_0 c^2$ is the rest energy of the particle, m_0 is the mass of the particle, v is the particle velocity, and c is the speed of light. The derivative of the kinetic energy with respect to velocity is therefore:

$$\frac{dE}{dv} = \frac{m_0 v}{\left(1 - \left(\frac{v}{c}\right)^2\right)^{3/2}} = m_0 v \left(\frac{E}{E_R} + 1\right)^3 \tag{2-4}$$

One may solve for velocity in terms of energy as well:

$$v = c\sqrt{1 - \left(\frac{1}{\frac{E}{E_R} + 1}\right)^2} \tag{2-5}$$

and take the derivative of velocity with respect to energy:

$$\frac{dv}{dE} = \frac{c}{E_R \left(\frac{E}{E_R} + 1\right)^3 \sqrt{1 - \left(\frac{E}{E_R} + 1\right)^{-2}}} \tag{2-6}$$

Having prepared to use the relativistic relationships listed above, the FEED model equations may now be derived. The FEED model begins with a phase space distribution function, $f(\vec{r}, \vec{v}, t)$, for the number of precipitating electrons, where $\vec{r}$ and $\vec{v}$ are the position and velocity vectors of each electron. The full time derivative of the distribution function is:

$$\frac{d}{dt} f = \frac{\partial f}{\partial t} + \frac{\partial \vec{r}}{\partial t} \cdot \frac{\partial f}{\partial \vec{r}} + \frac{\partial \vec{v}}{\partial t} \cdot \frac{\partial f}{\partial \vec{v}} \tag{2-7}$$

Note that the velocity of the particle is equal to the time rate of change of the position of the particle, $\vec{v} = \frac{\partial \vec{r}}{\partial t}$. Also note that the stopping force acting in the opposite direction on

the particles is the time rate of change of the velocity, $\vec{F}_{\text{col}} = m\frac{\partial \vec{v}}{\partial t}$. With these substitutions, Equation 2-7 is re-expressed:

$$\frac{d}{dt}f = \frac{\partial f}{\partial t} + \vec{v}\cdot\frac{\partial f}{\partial \vec{r}} + \frac{\vec{F}_{\text{col}}}{m}\cdot\frac{\partial f}{\partial \vec{v}} \tag{2-8}$$

Assuming that the energetic particles are precipitating vertically, and that the stopping force is only in the $\hat{z}$ direction, then $\vec{v} = v\hat{z}$ and $\vec{F}_{\text{col}} = F_{\text{col}}\hat{z}$. The third term of the right side of Equation 2-8 can be written in terms of energy such as $\frac{\partial f}{\partial v} = \frac{\partial E}{\partial v}\frac{\partial f}{\partial E}$. Considering relativistic electrons, the third term of Equation 2-8 becomes $F_{\text{col}}v\frac{\partial f}{\partial E}/(1-(v/c)^2)^{3/2}$. Substituting for the third term and allowing time derivatives to go to zero for a steady-state solution, Equation 2-8 becomes:

$$0 = \frac{\partial f}{\partial z} + \frac{F_{\text{col}}}{(1-(v/c)^2)^{3/2}}\frac{\partial f}{\partial E} = F_{\text{col}}\left(\frac{E}{E_R}+1\right)^3\frac{\partial f}{\partial E} \tag{2-9}$$

Thus, the one-dimensional differential equation for the distribution function as a function of altitude z is:

$$\frac{\partial f}{\partial z} = -\frac{F_{\text{col}}}{(1-(v/c)^2)^{3/2}}\frac{\partial f}{\partial E} = -F_{\text{col}}\left(\frac{E}{E_R}+1\right)^3\frac{\partial f}{\partial E} \tag{2-10}$$

where the distribution function f is now a function of two variables: E and z. Using a fluid approximation, when multiplied by the velocity v, f is transformed into a quantity that is proportional to electron flux, ϕ_e.

$$\phi_e(E,z) \propto v(E)f(E,z) \tag{2-11}$$

One may substitute ϕ_e/v into Equation 2-10, with the following step-by-step results:

$$\frac{\partial}{\partial z}\left(\frac{\phi_e}{v(E)}\right) = -F_{\text{col}}\left(\frac{E}{E_R}+1\right)^3\frac{\partial}{\partial E}\left(\frac{\phi_e}{v(E)}\right) \tag{2-12}$$

Expanding the derivatives:

$$\left(\frac{1}{v(E)}\right)\frac{\partial \phi_e}{\partial z} = -F_{\text{col}}\left(\frac{E}{E_R}+1\right)^3\left[\left(\frac{1}{v(E)}\right)\frac{\partial \phi_e}{\partial E} + \phi_e\frac{\partial}{\partial E}\left(\frac{1}{v(E)}\right)\right] \tag{2-13}$$

Multiplying by velocity:

$$\frac{\partial \phi_e}{\partial z} = -F_{\text{col}} \left(\frac{E}{E_R} + 1 \right)^3 \left[\frac{\partial \phi_e}{\partial E} + v(E) \phi_e \frac{\partial}{\partial E} \left(\frac{1}{v(E)} \right) \right] \tag{2-14}$$

Expanding the derivative with respect to energy:

$$\frac{\partial \phi_e}{\partial z} = -F_{\text{col}} \left(\frac{E}{E_R} + 1 \right)^3 \left[\frac{\partial \phi_e}{\partial E} - \frac{\phi_e}{v(E)} \frac{\partial v}{\partial E} \right] \tag{2-15}$$

Evaluating the derivative with respect to energy, using the relativistic relationships noted above:

$$\frac{\partial \phi_e}{\partial z} = -F_{\text{col}} \left[\left(\frac{E}{E_R} + 1 \right)^3 \frac{\partial \phi_e}{\partial E} - \frac{\phi_e}{E_R \left(1 - \left(\frac{E}{E_R} + 1 \right)^{-2} \right)} \right] \tag{2-16}$$

The stopping force for electrons, $F_{col}(E)$, which opposes the electron motion, is obtained from *Berger et al.* (1984) and is based on the Bethe formula integrating the Møller differential cross section for inelastic collisions. The stopping force is a function of energy and altitude and Figure 2-10 shows the stopping force for air at sea level used in FEED (red) and Monte Carlo (blue) models. The two stopping powers are similar for most of the energy range and they are only slightly different below 100 eV. The stopping power is scaled to the higher altitudes, based on the air density.

The differential equation, Equation 2-16, is solved using a central finite difference scheme with second order accuracy. The input flux from WIPP is taken at 200 km altitude and it is integrated progressively downwards in altitude. Because the input flux at 200 km is a function of energy and time, this calculation is performed at each time instance across all energy and repeated for each time step considered.

Secondary ionization is calculated based on the electron flux with altitude. The ionization rate per volume per unit electron flux, $\frac{q}{\phi_e}$, is taken from *Rees* (1963) and shown here:

$$\frac{q}{\phi_e} = \frac{E/r_0}{\Delta E_{ion}} \lambda \left[\frac{z_h}{R} \right] \frac{n(M)_{z_h}}{n(M)_R} \tag{2-17}$$

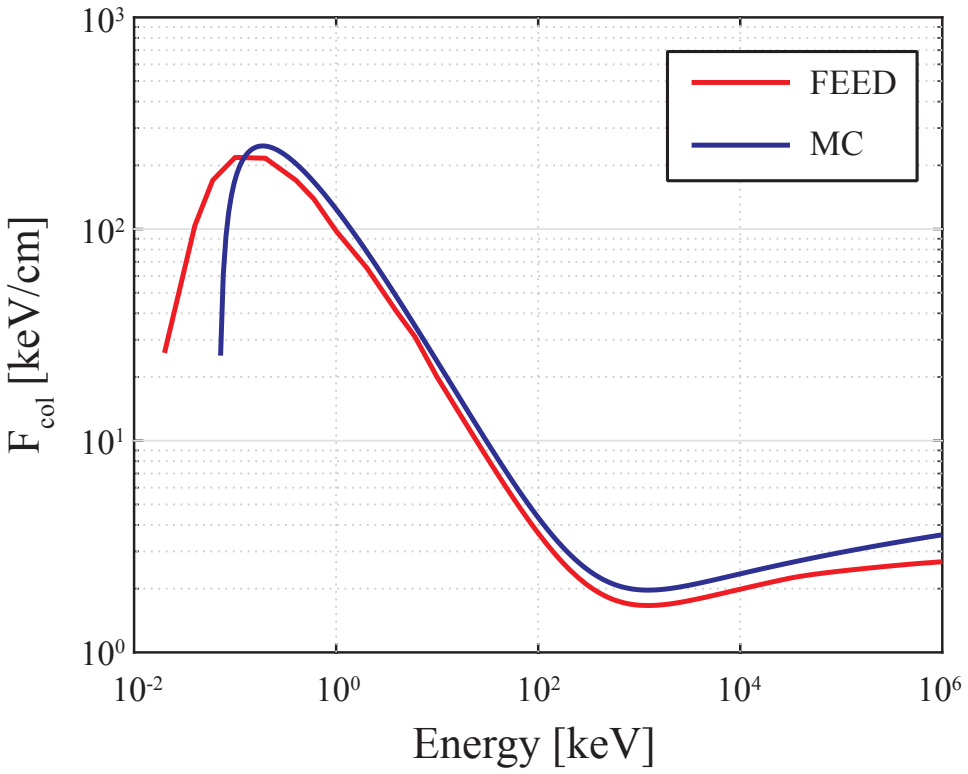

Figure 2-10. Energy dependent collisional stopping power for energetic electrons for air at sea level (*Berger et al.*, 1984). The stopping force used in FEED (red) and Monte Carlo (blue) are shown for comparison.

where E is the initial energy of the electron, ΔE_{ion} is the mean energy to create an ion-electron pair (35 eV), R is the penetration depth, $\frac{z_h}{R}$ is the fractional penetration depth, $\lambda\left[\frac{z_h}{R}\right]$ is the normalized energy dissipation (or deposition) function, $n(M)_{z_h}$ and $n(M)_R$ are ratios of the number densities of O_2, N_2, and O, at atmospheric depths, z_h and R, respectively, $r_0 = \frac{R}{\rho}$ is the range for electrons at energy, E, and ρ is the mass density at the lowest altitude of penetration.

The atmospheric parameters such as the atmospheric depth, z_h, the mass density, ρ, and the number density ratio, $n(M)$, are found in Table 1 of *Rees* (1963). This work uses the same neutral density profile that the Monte Carlo deposition code uses. Therefore, z_h and ρ from Table 1 of *Rees* (1963) are scaled appropriately in this work.

Because the penetration depth, R, is energy dependent and the FEED model uses the energy range from 100 eV to 1 MeV, this work uses Equations 2-18 and 2-19 for the penetration depth, R, (*Gledhill*, 1973).

$$\log R = -5.133 + 1.358 \log E - 0.215 (\log E)^2 - 0.043 (\log E)^3 \qquad (0.1 < E < 100 \text{ keV}) \quad \text{(2-18)}$$

$$\log R = -6.193 + 2.585 \log E - 0.22 (\log E)^2 \qquad (100 \text{ keV} < E) \quad \text{(2-19)}$$

where $\log x$ is log base 10 ($\log_{10} x$). The penetration depth expressions are derived assuming the incoming electron flux is isotropic. The penetration depth ratio, $\frac{z_h}{R}$, is altitude dependent ranging between -0.4 and 1, with negative values being backscatter. As the energetic electrons penetrate to the lower altitude, $\frac{z_h}{R}$ increases to 1, indicating maximum penetration (the higher the altitude is, the smaller $\frac{z_h}{R}$ is). This parameter decides the energy deposition, or energy dissipation (λ), as the energetic electrons precipitate through the ionosphere. In this work, the normalized energy dissipation distribution function is chosen assuming an isotropic angular distribution of incoming electrons with pitch angles between 0° and 80°. With this energy distribution function, 83% of the energy deposition is from forward-scattering and 17% of the energy deposition is from back-scattering. The distribution function is shown in Figure 1 of *Rees* (1963).

The secondary ionization production rate, Equation 2-17, can now be analyzed. Equation 2-17 is a function of energy and altitude where E, r_0, and $n(M)_R$ are energy-dependent, $n(M)_{z_h}$ is altitude-dependent, and $\lambda\left[\frac{z_h}{R}\right]$ is energy and altitude dependent. The ionization rate is calculated at each altitude with different energy values and is presented in Figure 2-11. As the incoming energy increases, the electrons can penetrate further down into the ionosphere, shown by the peaks progressively moving down in altitude. Additionally, the maximum of the peaks increase with higher incoming energy. For example, with 100 keV electrons, the peak of

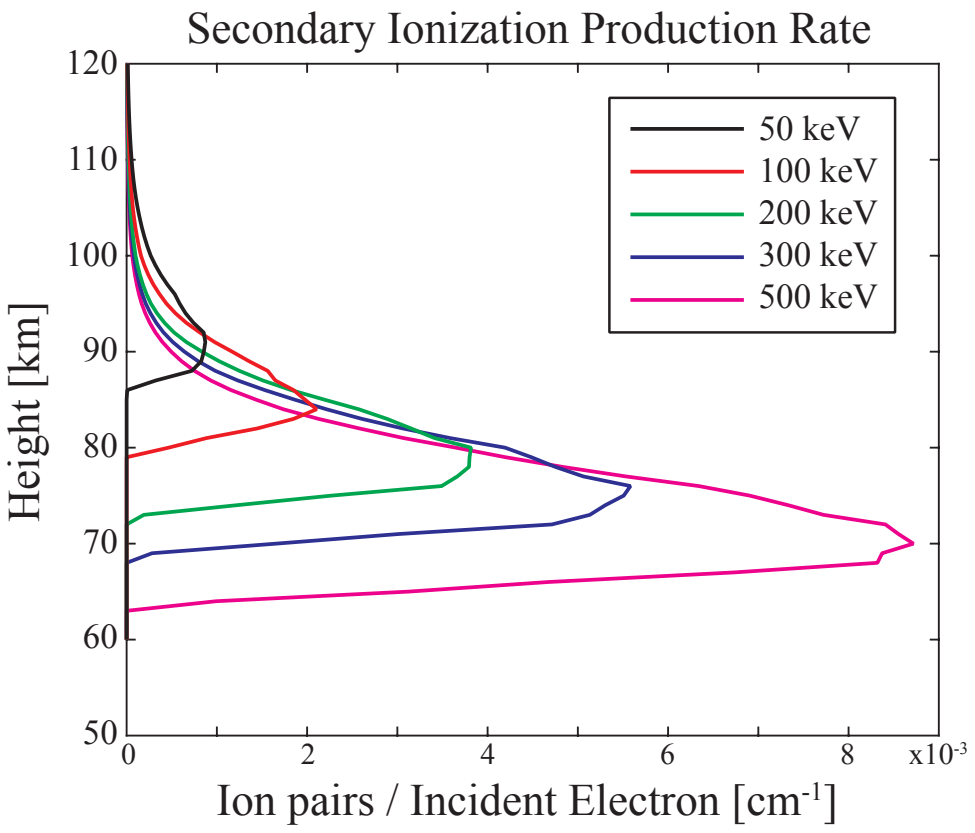

Figure 2-11. Secondary Ionization Production Rate.

the secondary ionization rate is $2.105 \cdot 10^{-3}$ cm^{-1} at 84 km and with 300 keV electrons, the peak of the ionization rate is $5.583 \cdot 10^{-3}$ cm^{-1} at 76 km.

The energetic electron flux is a function of altitude, energy and time. At one time step, the electron flux is multiplied by the corresponding secondary ionization rate at each energy throughout altitude. This is multiplied by the differential time increment (dt). Then, the number of produced electrons is summed across energy at each altitude. As a result, the electron density change is calculated at one time step throughout altitude (accounted for all energy). This process is repeated over time and the secondary ionization profiles are summed to the time of interest. This calculation process determines the ionospheric response due to the incoming flux. A sample result of the FEED model is shown in Figure 2-12. The range of the energy shown in the figure is 30 keV to 1 MeV and each curve represents the summation of the secondary ionization up to the corresponding energy values. As shown in Figure 2-12,

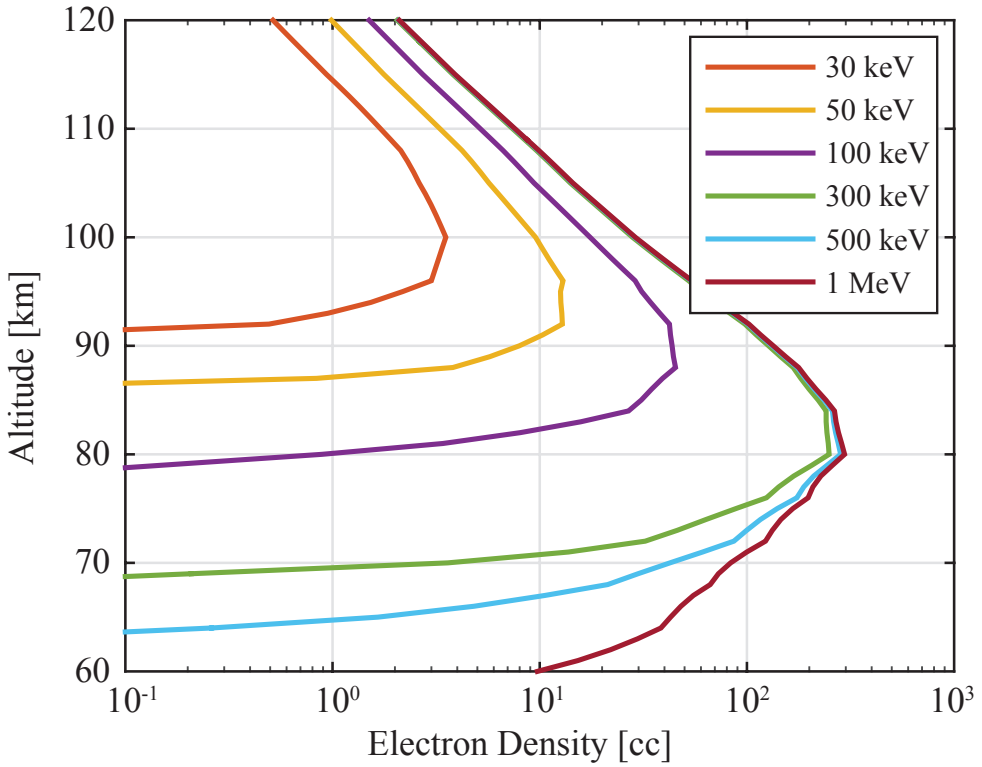

Figure 2-12. FEED Model Sample Result. Electron density change due to the secondary ionization from 30 keV up to respective energies.

the primary interest of energy for LEP (100 keV to 300keV) accounts for the majority of the secondary ionization approximately above 70 km. The results are compared with a well established Monte Carlo deposition model in Section 2.3.3.

2.3.2 FEED Model Assumptions and Limitations

Several assumptions built into the FEED model limit the applications of the model in practice. The first assumption is in the application of the energy-dependent external force to the Boltzmann Equation. Technically, this energy-dependent force can produce a non-unity-magnitude Jacobian for the Boltzmann volume element, and it is assumed in this work that the Jacobian remains unity in magnitude. Secondly, it is assumed that enough particle precipitation flux is present that the flux can be treated as a fluid. This assumption excludes the effects of individual high-energy particles, for instance, or particle populations with extremely stressed electron energy distributions. Furthermore, the FEED model neglects the effects of the Earth's

magnetic field, which changes the way particles behave at altitudes above the D-region ionosphere.

These assumptions essentially limit the applicability of the FEED model to simulations of energetic particle precipitation into ionosphere. Reasonable applications would include auroral precipitation, VLF-transmitter induced precipitation, lightning-induced precipitation, and precipitation produced by electromagnetic ion-cyclotron (EMIC) waves.

2.3.3 FEED Model Validation

The newly implemented FEED model is compared with a Monte Carlo deposition model (*Lehtinen*, 2000) which has been widely used to calculate electron density changes (*Peter and Inan*, 2004; *Cotts et al.*, 2011). The details of the Monte Carlo model are presented in Chapter 1. Both the Monte Carlo and FEED models take incoming flux and calculate resulting secondary ionization production. The main difference is that the Monte Carlo technique tracks the motion of electrons, while the FEED model uses a fluid approach. The biggest benefit of using the FEED model is the run time. The run time of the FEED model is significantly faster than the Monte Carlo model. Using University of Florida's super computer (HiperGator) with the computer resources of 4 cores and 8 GB of RAMs, the Monte Carlo takes on average 10 hours of run time while the FEED model takes 40 minutes ($\sim$15 times faster). It is noted that the Monte Carlo is not parallelized and did not utilize multiple cores, while the FEED model used the built-in MATLAB parallelization. Figures 2-13 and 2-14 show the direct comparisons of the two models for a range of energies, when given the same input electron flux.

Figure 2-13 is the summation of the secondary ionization for different ranges of electron energies. The minimum energy for these models is 30 keV and the secondary electron density is integrated up to 50 keV (yellow), 100 keV (purple), 300 keV (green), 500 keV (blue), and 1 MeV (red). The dashed lines are Monte Carlo results and the solid lines are FEED model results.

Looking at the altitude where the secondary ionization change stops, the maximum penetration depths of the incoming electron flux are close between the two models, within a

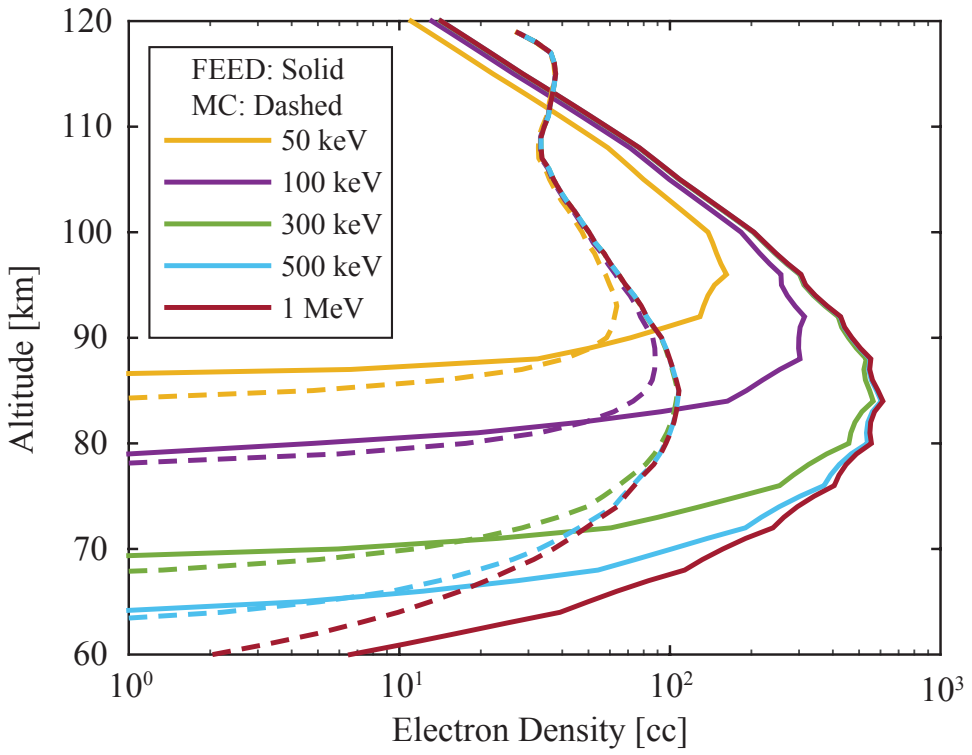

Figure 2-13. FEED and Monte Carlo comparisons: Secondary ionization for different energies.

few kilometers for each energy range. Specifically, the penetration altitude difference between the two models for 100 keV and 300 keV is $\sim$ 2 km. The altitude of each electron density peak agrees well between FEED and Monte Carlo models. At 100 keV, the peak electron density altitude is at 90 km for FEED and 88 km for Monte Carlo and at 300 keV, it is at 84 km for FEED and 85 km for Monte Carlo. The density peaks of each energy range also match within a factor of four or five with the previous model. Considering the significant reduction on the computation time and the similar accuracy of the results, the fluid model is the preferred method to implement large number of simulations.

Figure 2-14 is the electron density change added to the actual D-region ambient profile. Above 90 km, the secondary ionization of both FEED and Monte Carlo is minimal and the electron density is nearly the ambient profile. At an approximate VLF reflection height of 80 km up to 300 keV, the total electron density is 465 electrons/cm^3 for FEED and 100 electrons/cm^3 for Monte Carlo Deposition, which is less than a factor of five. It is noted that

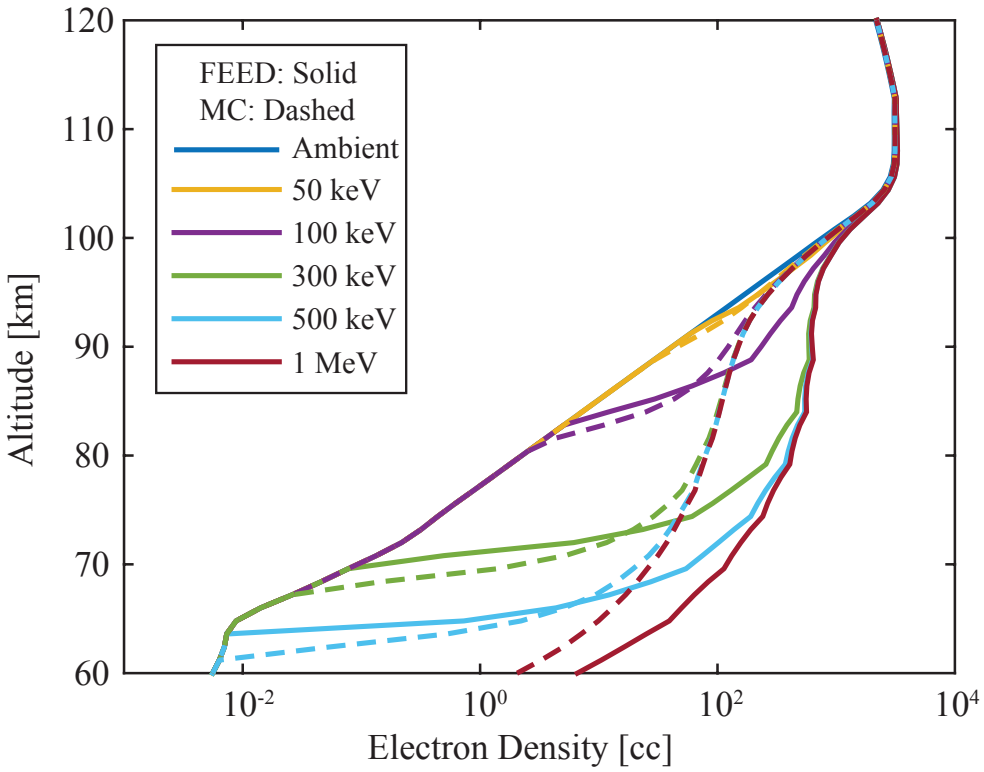

Figure 2-14. FEED and Monte Carlo comparisons: Electron density profiles for different energies.

the energy up to 100 keV causes a minimal increase in the total electron density profile above ambient for both models. Also, the majority of the additional ionization is contributed by the energy between 100 keV and 300 keV for the altitude range of 70 km to 90 km for both models. This region corresponds to the typical VLF reflection height for nighttime ionosphere.

2.4 3D LWPC: Transient Technique

Using WIPP and FEED models, LEP process of lightning energy interactions in the magnetosphere and the secondary ionization effect in the ionosphere can be modeled. The transient LEP VLF signature is a result of the VLF signal scattered by the secondary disturbance in the lower ionosphere. This can be simulated by integrating the two models with the Long Wave Propagation Capability (LWPC) code.

As described in Chapter 1, the WIPP code outputs the precipitating flux as a function of energy and time and the FEED model produces the secondary ionization electron profiles in

terms of time across altitude. To account for the time-varying LEP transient, the 3D LWPC code is simulated repeatedly to model the change of the scattered field. In order to do so, the secondary ionization electron density profiles which are stepping in time are inputted to the LWPC code as separate runs and this produces the total field and scattered field change over time. Since the purpose of the two codes, WIPP and FEED, is to quantify the incoming flux distribution and its secondary ionization effects, this combination of the three codes can quantify the onset delay and onset duration caused by the period of the electron density enhancement representing the LEP onset. This work focuses on modeling onset delay and duration of LEP events and LEP recovery modeling is beyond the scope of this work. In later sections, the effects of the disturbance radial expansion are investigated and varying disturbance locations along the GCP and off the GCP are analyzed for inter-hemispheric timing.

2.5 Examples of LEP Event Modeling

Details of the three models have been explored in the previous sections. In this section, the focus is the combination of the three models with a sample case of the entire LEP process, showing specific simulation results of each model.

Figure 2-15a is the precipitating flux at 200 km altitude as a function of energy and time from WIPP code, when the input lightning peak current is 130 kA injected at 30° latitude. The black box in Figure 2-15a indicates the energy and time range of interest for LEP secondary ionization, corresponding to the energy range of 100 keV to 1 MeV and the time up to 2 seconds. The majority of the electrons in this energy range, which causes most of the secondary ionization, precipitate within the first two seconds (*Peter and Inan*, 2007). The precipitating flux integrated with energy (greater than 10 keV) produces the energy flux in terms of time, as shown in Figure 2-15b. The peak of the energy flux is 0.3 milli-ergs/cm^2/sec at 0.72 second. For $t > 1$ second, the energy flux decreases substantially. The precipitating flux on Figure 2-15a can also be presented at a single time slot to see the differential flux as

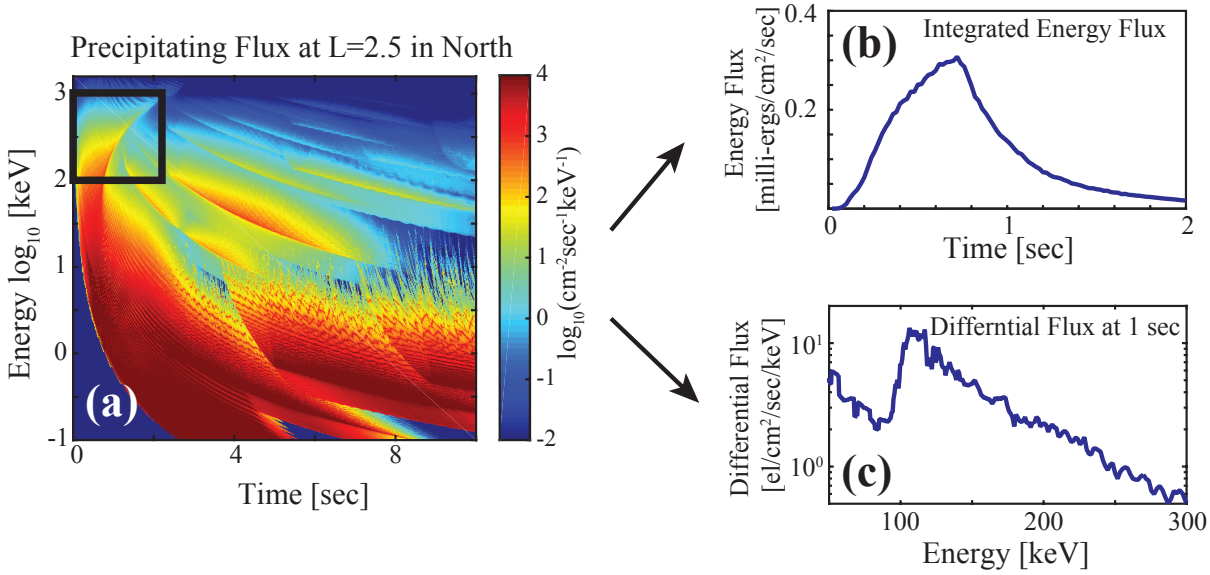

Figure 2-15. Sample results of WIPP: (a) is the differential precipitating flux at L=2.5 in the northern hemisphere at 200 km altitude, (b) is the integrated energy flux with time, and (c) is the differential flux at 1 second over energy.

a function of energy. Figure 2-15c is the differential flux at 1 second between 50 keV and 300 keV. The peak of the flux occurs at $\sim$ 100 keV at 1 second.

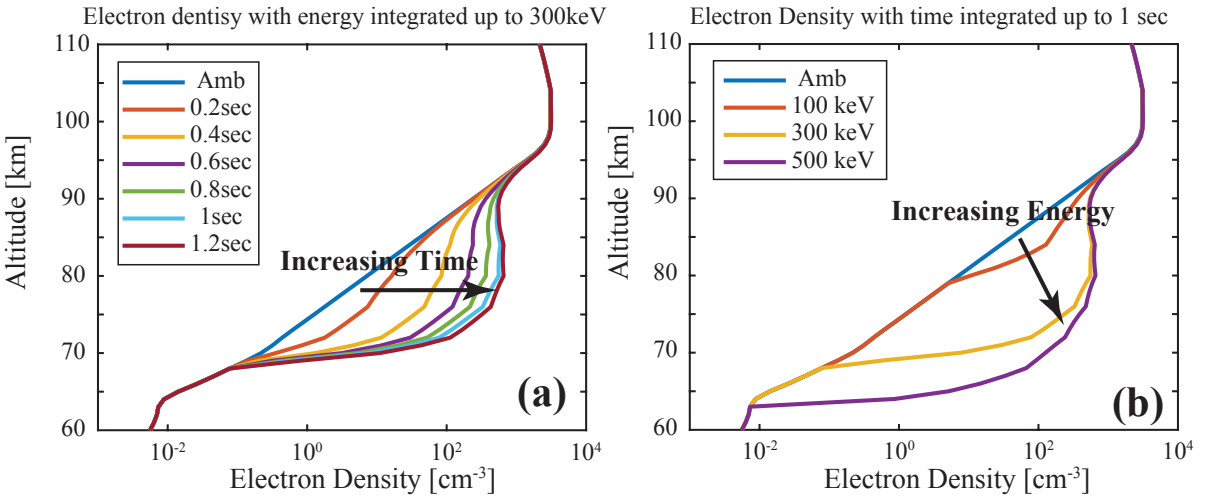

Figure 2-16. Sample results of FEED: (a) is the electron density profiles when increasing time with the same range of energy (integrated up to 300 keV) and (b) is the electron density profiles with increasing energy with the same range of time (up to 1 second).

The FEED model uses the differential flux at 200 km altitude sequentially over time in order to calculate the electron flux over altitude, energy and time and to produce the secondary ionization. The electron density profiles integrated up to 0.2 s, 0.4 s, 0.6 s, 0.8s, 1 s, and 1.2 s are shown in Figure 2-16a. The secondary ionization is summed up to 300 keV and is also integrated up to each time instant in order to see the gradual change of the electron density with time. The electron density peak reaches its maximum at 1.2 seconds and there is only minimal change afterwards. This minimal change of the electron density agrees well with Figure 2-15b which shows minimal energy flux after 1.2 seconds.

Figure 2-16b is the electron density with different energy range, integrated up to 1 second. The red, yellow, and purple lines are the electron densities considering the integrated energy flux up to 100 keV, 300 keV, and 500 keV, respectively. There is a substantial increase between the 100 keV and 300 keV electron density profiles and the peaks descend in altitude with increasing energy, which could potentially affect VLF reflection height.

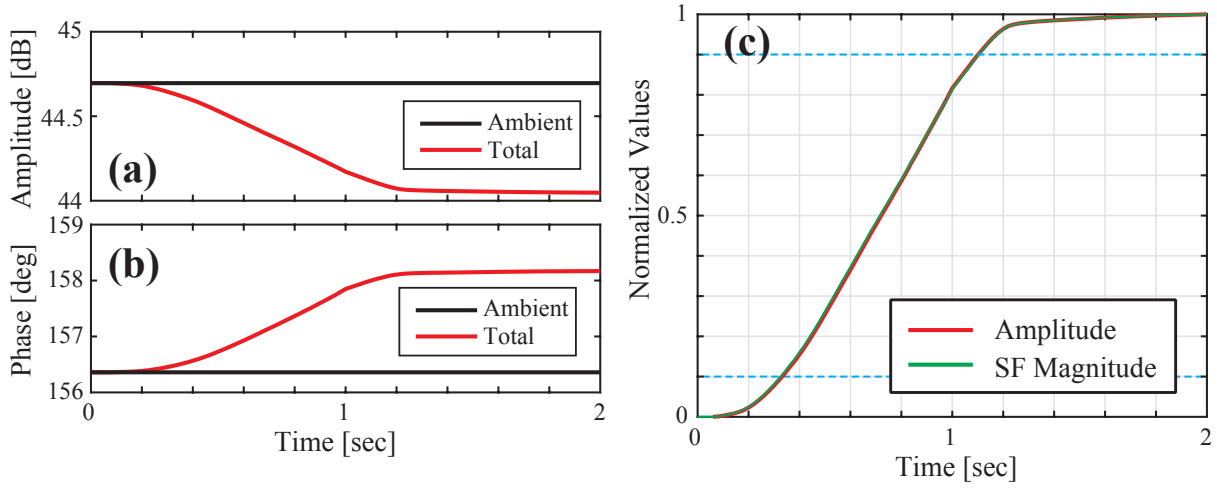

Figure 2-17. Sample results of LWPC: (a) is the amplitude of the ambient and total fields, (b) is the phase of the ambient and total fields, and (c) is the amplitude and scattered field magnitude signals normalized between 0 and 1.

The electron density profiles with time, as shown in Figure 2-16a, are placed as a scattering body on a propagation path in the LWPC code. The LWPC code calculates the electric field amplitude of the total and ambient signals and it is presented in Figure 2-17a. Figure

2-17b is the phase signal of the total and ambient signals and Figure 2-17c is the normalized amplitude-only and scattered field magnitude signals. For this particular example, the scattering body is positioned directly on the propagation path and the normalized amplitude and the SFM are identical with the same onset time, onset duration, and general shape.

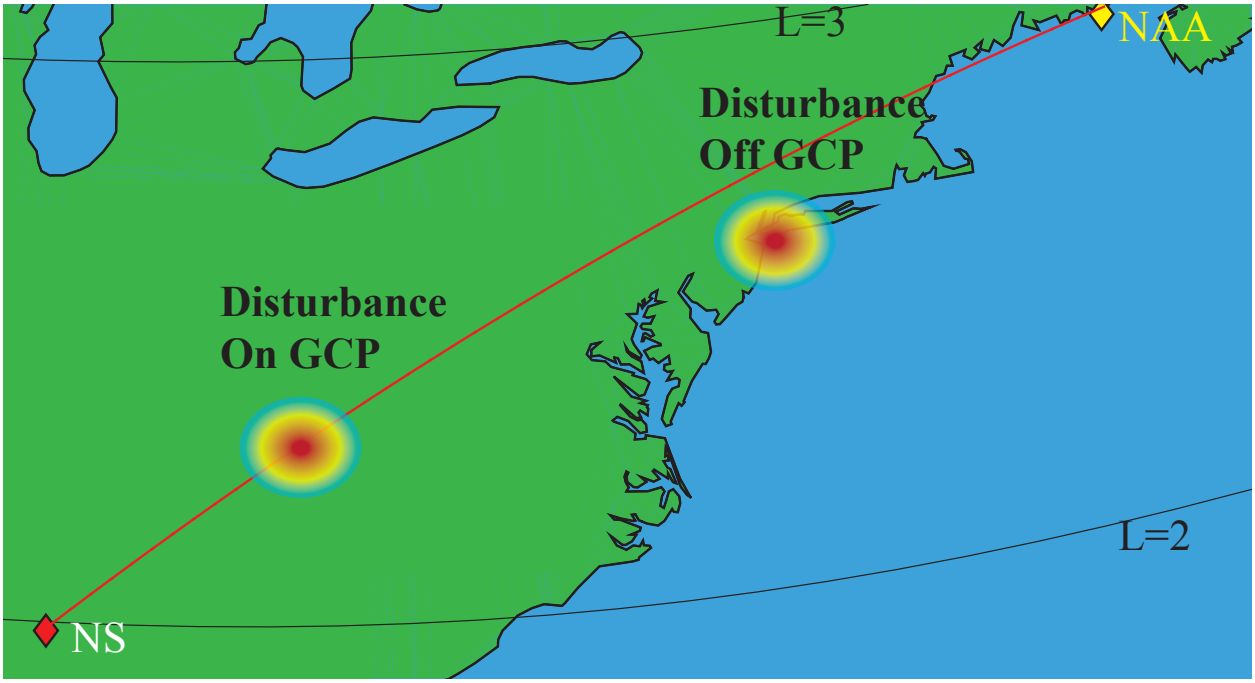

Figure 2-18. Illustration of electron disturbances on and off the propagation path (NAA-NS) in the northern hemisphere.

Using the combined models, different aspects of the disturbances can be explored such as the disturbance radius (constant or time-varying) and the location of the disturbance (on- or off-GCP). Figure 2-18 is an illustration of the LEP disturbances located on and off the propagation path of NAA-NS. Four variations of the precipitation disturbance are simulated using the three models. For a constant radius (200 km, or FWHM of 150 km), the disturbance is positioned on the GCP and 100 km off the GCP and the normalized SFM signals are calculated, which is shown in Figure 2-19 as the solid lines. A time-varying radius (110 km to 200 km in 1 second) disturbance is simulated in the same two locations (on and off GCP). The normalized SFM signals are shown in Figure 2-19 as the dashed lines.

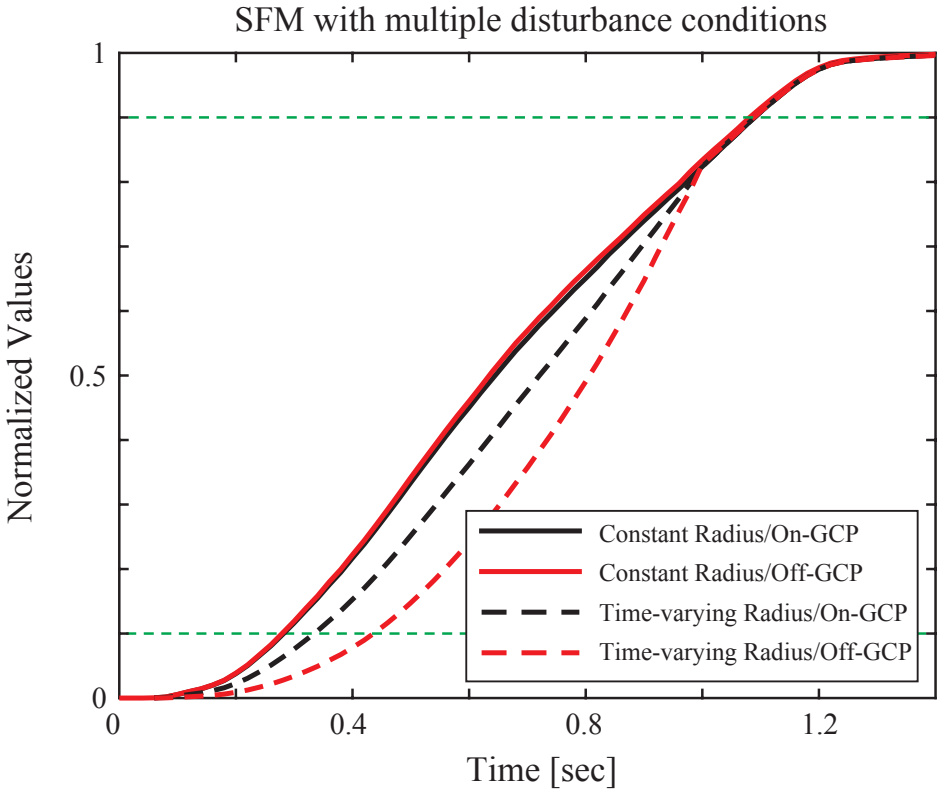

Figure 2-19. Normalized SFM with multiple disturbance conditions when the disturbance radius is constant on the propagation path (black solid) and off the propagation path (red solid) and when the disturbance radius is varying with time on the propagation path (black dash) and off the propagation path (red dash).

When the radius is constant, the onset time and onset duration of the normalized SFM are the same whether the disturbance is located on or off the propagation path. When the radius is time-varying, the onset time is delayed relative to the constant radius onset time. There is an additional onset delay when the disturbance is 100 km perpendicular to the GCP, compared to the time-varying on-GCP case. This shows that the onset time delay is affected by the disturbance size change with time. It also shows the distance from the propagation path contributes additional onset time delay when the disturbance is time-varying.

Figure 2-20 shows the LWPC results of the disturbance on the GCP with a constant FWHM of ~150 km. The left and right panels of the figure use ambient electron density

profiles II and III as seen in *Moore and Agrawal* (2011). In the left panel, the normalized amplitude has multiple unusual signatures, specifically the negative dip at the onset, which results from modal interference. Also, the sharp change at 0.6 sec is due to the modal interference which is an LWPC artifact. The right panel, however, shows the normalized amplitude and SFM following the shapes of the observations reported in this document. Because the results when using Profile III resemble the experimental observations, Profile III is chosen for the remaining modeling work in this document. Also seen in the right panel of Figure 2-20, the onset of the normalized amplitude and SFM are the same since the disturbance is located directly on the propagation path of NAA-NS and the FWMH is constant.

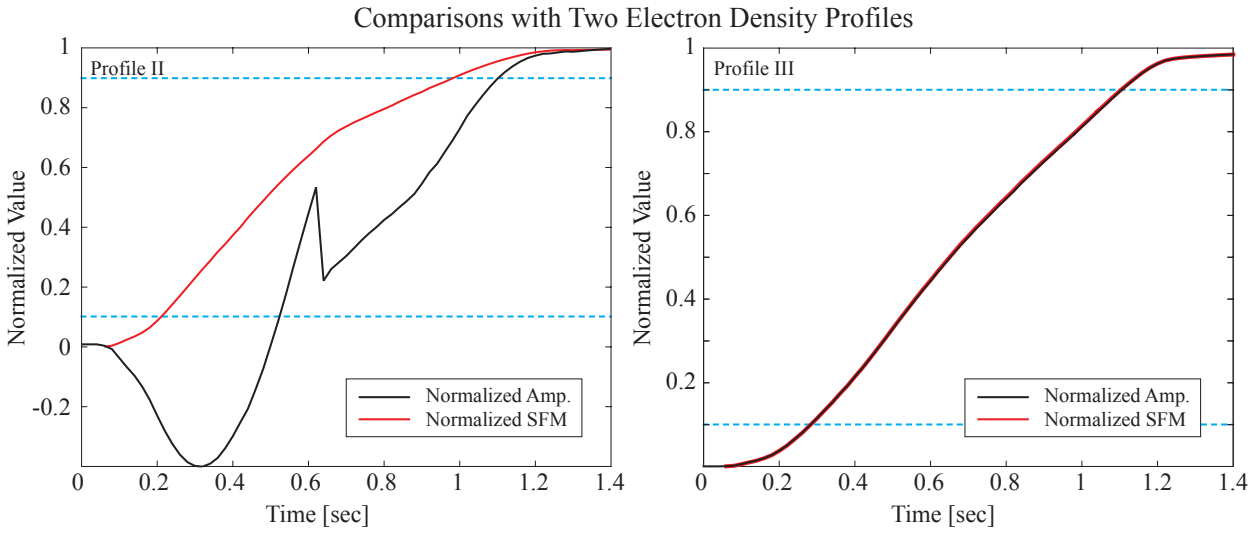

Figure 2-20. Normalized amplitude and SFM using two electron density profiles on the GCP. The left panel uses Profile II and the right panel uses Profile III (*Moore and Agrawal*, 2011)

2.6 Summary

The Fluid Energetic Electron Deposition model (FEED) is newly developed and produces compatible results to the Monte Carlo deposition model. The significant benefit of the FEED model is the run time being 15 times faster than the Monte Carlo model, realistically allowing secondary ionization profiles to be calculated sequentially over time. By successfully combining the three codes, LEP physical processes can be appropriately modeled, which allows the investigation of LEP event characteristics. In this work, this method is used to explore

the inter-hemispheric timing between conjugate LEP events and its spatial and temporal development. Ducted and nonducted perspectives of LEP disturbances can be investigated using the combined models. Experimental observations made in this document are simulated with these models to further approximate and understand LEP disturbances.

CHAPTER 3
INTER-HEMISPHERIC TIMING ANALYSIS FOR CONJUGATE LEP EVENTS

Chapter 2 discussed the modeling technique that will be used in this dissertation to simulate LEP event physics. In this chapter, experimental ground-based observations of conjugate LEP events are reported and quantified using both scattered field analysis and amplitude-only analysis. 46 conjugate LEP events that were simultaneously detected over North America, using the University of Florida's North American VLF (NAV) Array, and in the southern hemisphere, near Palmer Station, Antarctica are analyzed. The interhemispheric timing of conjugate LEP event properties are analyzed statistically for comparison with LEP model predictions and with previously reported observations. Surprisingly, scattered field analysis of the events produces significantly different results than amplitude-only analysis of the events. As a result, the observed interhemispheric timing dependencies of any individual conjugate LEP event (presented by this report or by any previous report) are not attributed to the asymmetries of the Earth's magnetic field. Based on these results, it appears that any convincing experimental detection of a dependence on the asymmetries of the Earth's magnetic field would require the use of scattered field analysis to interpret the data and require sensitivity to the spatial and temporal distribution of the ionospheric disturbances produced in both hemispheres.

3.1 Description of the Experiment

A large geomagnetic storm occurred on 17 March 2015 with a Dst index of -223 nT and a planetary Kp index of 8, affecting energetic electron behavior in the radiation belts and increasing the rate of natural loss process (*Horne et al.*, 2005; *Li et al.*, 2016). During the storm, two VLF transmitter signals were tracked to detect conjugate LEP events, as shown in Figure 3-1. The NAA transmitter signal (24.0 kHz, Cutler, Maine) was recorded at Tuscaloosa, Alabama (NS, 33.47° N, 87.63° W) for the northern hemisphere path, and the NPM transmitter signal (21.4 kHz, Laulaulei, Hawaii) was tracked at Palmer station, Antarctica (PA, 64.77° S, 64.05° W) for the southern hemisphere path. As a result of the

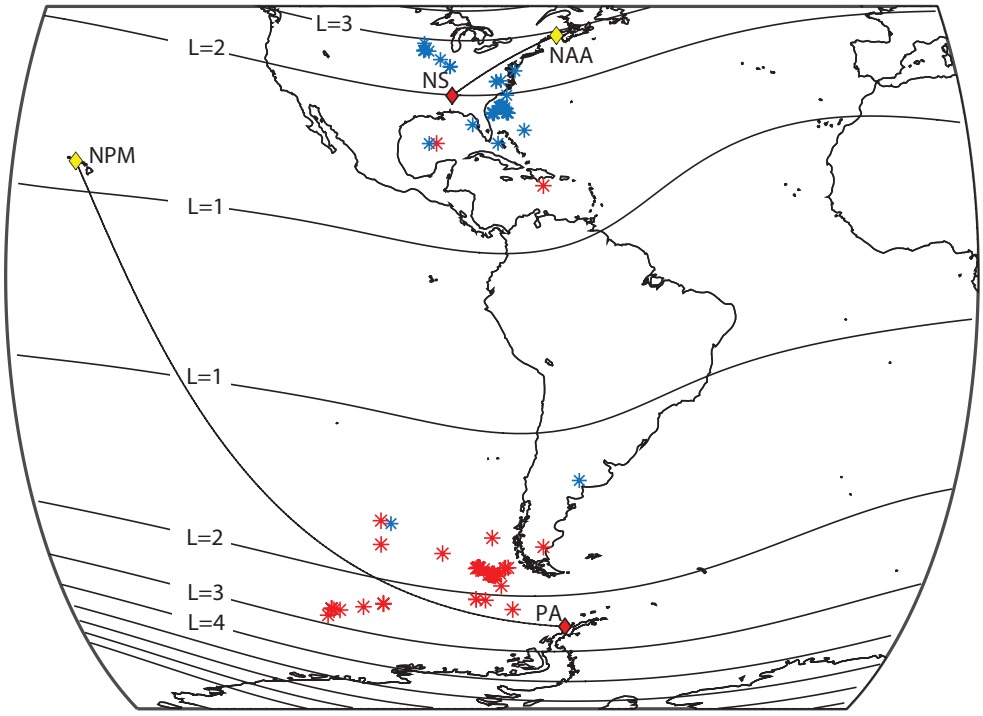

Figure 3-1. A map of Transmitter-Receiver great circle paths (GCPs) with L-shell lines and causative lightning flashes. Blue and red asterisks represent strike locations and their conjugate points, respectively.

storm, 46 conjugate LEP events were observed, with 24 isolated events and 22 overlapped events. All events are observed within 16 days after the geomagnetic storm and 36 of the 46 conjugate events were observed on March 22 and March 23.

Many LEP events are observed during this period, but not all of them exhibit signatures that allow for unambiguous interpretation using both scattered field analysis and amplitude-only analysis. Narrowband data recorded at both NS and PA were closely inspected to search for conjugate LEP events as a result of the geomagnetic storm on March 17, 2015. While the receiver system at Northside operated continuously, the system at Palmer Station operated on nine days between March 17 and March 31, 2015; therefore 9 days are available during this period to search for conjugate LEP events. A total number of 667 LEP events were observed to exhibit amplitude *or* phase signal perturbations (or both) at NS, while 1026 LEP events were observed at PA. Among these events, only 545 conjugate LEP events simultaneously

occur at both sites. Among these 545 events, 16 events exhibited perturbations on only the amplitude or phase at NS, and on only the amplitude or phase at PA. 194 of the 545 events exhibited both amplitude and phase perturbations at one site, but only amplitude *or* phase perturbations at the other site. The remaining 335 events produced amplitude and phase perturbations at both sites simultaneously. Of the 335 simultaneously occurring events with amplitude and phase changes observed in both hemispheres, only 69 events exhibit amplitude changes larger than 0.2 dB and phase changes larger than 4°. Of these 69 events, 23 events exhibit complicated overlapping onset signatures that do not lend themselves to straightforward (and reliable) scattered field analysis. After applying all of these filters, 46 conjugate LEP events remain and are analyzed in this document.

Satellite observations of the radiation belts during the storm showed that the slot region of the radiation belts started to appear around March 23 and was reformed 10 days after the storm (*Pierrard and Rosson*, 2016), consistent with observations of increased LEP activity on those days. GLD-360 recorded flashes are matched with corresponding VLF events to determine the hemisphere origin of lightning flashes. 44 events originated in the northern hemisphere and 2 in the southern hemisphere. All of the conjugate observations recorded in this paper are associated with clearly identifiable whistlers (at PA) and causative sferics (at NS and PA) in broadband data. The presence of whistlers at Palmer Station indicates that ducts were present during this period, although it does not imply that all LEP events observed during this period were ducted LEP events, as opposed to non-ducted LEP events. The 46 conjugate events are analyzed to quantify LEP characteristics using only amplitude observations on the one hand, and using the scattered field magnitude (SFM), which incorporates both amplitude and phase observations, on the other hand.

3.2 Definitions of LEP Event Characteristics

Previous work (*Cotts et al.*, 2011) has supplied the following definitions for LEP event characteristics. In this work, we apply these definitions to both amplitude-only observations and to scattered field magnitude observations, as described below.

- The *onset time* (t_{on}) is the point in time when the amplitude (or scattered field magnitude, SFM) of the signal begins to deviate from the ambient signal level. It is expected that this time is associated with the beginning of the ionospheric disturbance. In practice, it is identified as the time at which the amplitude (or SFM) reaches 10% of its maximum deflection.

- The *onset delay* (Δt) is the time between the causative lightning discharge and the *onset time*. The physical processes that occur during this time period include the lightning discharge, propagation through the ionosphere, coupling to the magnetosphere, propagation to the equatorial region, the scattering trapped electrons, and the subsequent precipitation of the electrons into the ionosphere. In this dissertation, the causative lightning discharge is not identified; instead, interhemispheric timing delays are calculated by taking the difference between northern and southern hemisphere onset times, which is the same as the difference between northern and southern hemisphere onset delays.

- The *onset duration* (t_d) is the time between the event onset (10%) and 90% of the peak amplitude (or SFM) deviation. It is intended to be a measure of how long the electrons precipitated onto the ionosphere.

- The *recovery time* (t_r) is the time between the peak amplitude (or SFM) deviation and the time when the signal returns to the pre-event level. Physically, the recovery time represents the time required for the atmospheric chemistry to return to equilibrium. Previous work defined the pre-event level as 10% of the maximum amplitude change. This dissertation quantifies the *recovery rate*, which quantifies the e-folding time as the slope of the scattered field magnitude on logarithmic scale. The details of the e-folding time are shown in Section 3.3.

- The maximum amplitude or phase change (ΔA or $\Delta\phi$) is the maximum deviation in the signal from the ambient level. The maximum magnitude (ΔM) is quantified on normalized SFM signals.

All the LEP event properties, whether defined on amplitude signals or on normalized SFM signals are presented graphically with details in Section 3.3.

3.3 Sequential Scattered Field Method

LEP events are categorized into isolated and overlapping events to rigorously quantify VLF perturbation properties. An isolated LEP event is defined as a standalone event during which neither amplitude nor phase signals exhibit another perturbation. It physically means that there is only one ionospheric disturbance patch near the GCP or that other disturbance patches are not significant in affecting the VLF signal. Overlapping LEP events occur when multiple disturbance patches are produced along the same GCP and each scatters a VLF signal resulting

in overlapping LEP signatures. The receiver sees the separate LEP temporal signatures as combined on top of another.

As it is described in Section 1.5, the VLF signal arriving at the receiver (the total field) is interpreted as a superposition of the direct signal from the transmitter (the ambient field) and the net signal scattered by the secondary ionization patch in the ionosphere (the scattered field) (*Poulsen et al.*, 1990; *Dowden and Rodger*, 1997; *Dowden et al.*, 1997; *Kotovsky and Moore*, 2015). The ambient field is estimated by interpolating linearly between the pre-onset and post-recovery ambient fields, and the normalized scattered field is calculated as described here. Figure 3-2 shows the scattered field analysis procedure for an isolated LEP event. Figure 3-2a and Figure 3-2b show the amplitude and phase of the total field, and Figure 3-2c shows a zoomed view of the amplitude perturbation exhibiting the event onset. The yellow dashed lines in Figure 3-2a and Figure 3-2b are the linear ambient estimations of the total field amplitude and phase, which are derived by linearly interpolating between first-order least-squares fits to the pre-onset and post-recovery ambient fields. Figure 3-2d shows the magnitude of the scattered field, whereas Figure 3-2e shows the magnitude normalized by the estimated ambient field and zoomed to the event onset. The red dashed line in Figure 3-2d shows the exponential decay fit obtained using the initial recovery rate. The initial recovery rate is taken to be the slope of the first order regression of the scattered field magnitude using a logarithmic time scale, and it is determined using the first 10 seconds after the event clearly starts to recover. It was observed that our entire dataset exhibits exponential decay rather than logarithmic decay, although *Dowden and Rodger* (1997) and *Dowden et al.* (2001) showed cases of both for LEP events, based on temporal variation of the scattered field magnitude. For data sets such as those presented by *Dowden and Rodger* (1997) and *Dowden et al.* (2001), it would be reasonable to apply the same process described here to isolate overlapping events, but substitute logarithmic recovery for exponential recovery. Note that we once again define the terms, scattered field magnitude (SFM) and scattered field angle (SFA), to highlight them and distinguish them from the amplitude and phase of the total field.

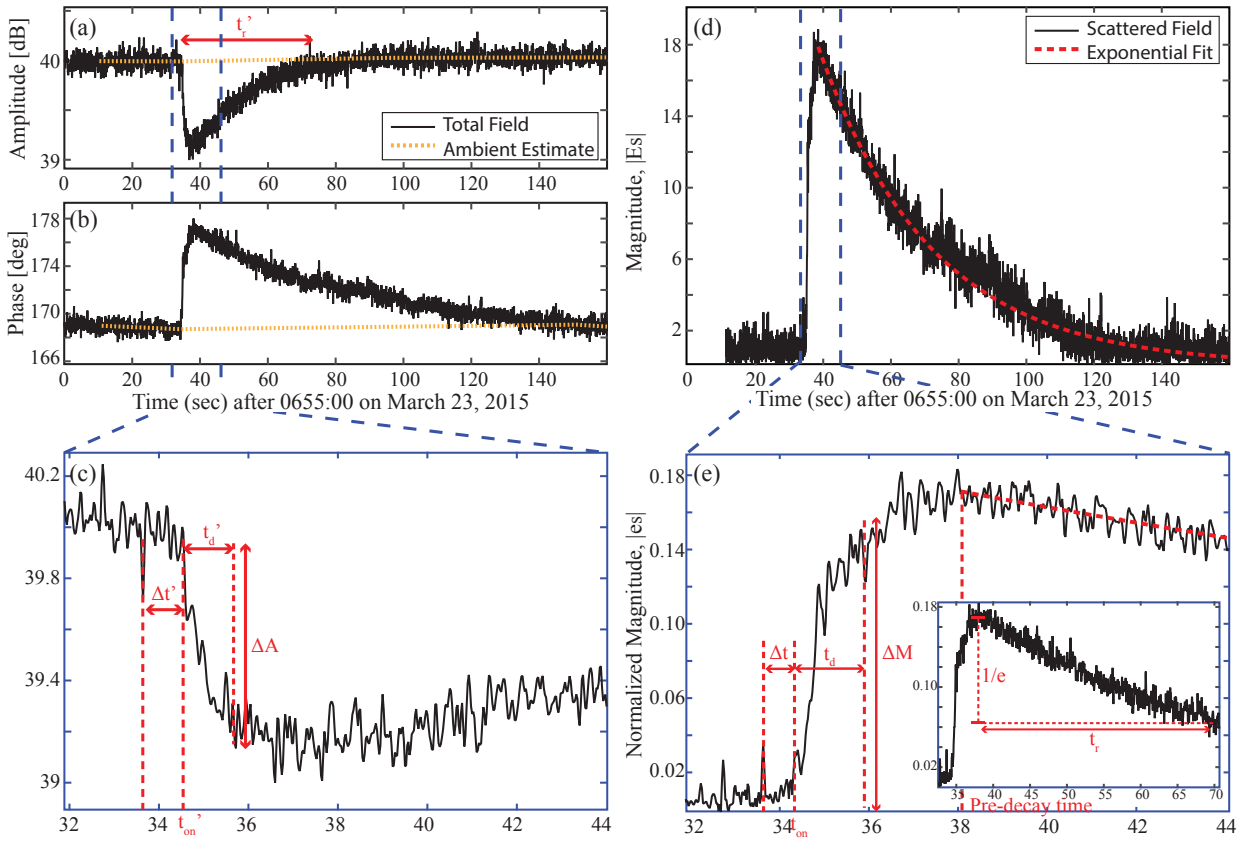

Figure 3-2. An isolated conjugate event observed on March 23, 2016. (a) Amplitude and (b) phase perturbations with the ambient estimate (yellow dotted line) and (c) amplitude zoomed in to the onset time. (d) The magnitude of the scattered field, resulting from the subtraction of the ambient estimate from the total field. The red dashed line is the exponential decay fit. (e) The magnitude of the normalized scattered field zoomed in to the onset time.

Figure 3-2c and Figure 3-2e show the event properties defined using the amplitude and the scattered field magnitude. The characteristics measured using the amplitude are different than those measured using the SFM, which implies that the differences may lead to different statistical results (see Section 3.4 for details). For clarity, properties denoted using an apostrophe (′) indicate the use of amplitude-only measurements.

Two types of overlapping events are observed in the dataset. The most common type occurs when a subsequent event overlaps the preceding event during its recovery stage. Another type occurs when the subsequent event overlaps the preceding event during its event onset. Figure 3-3 shows a ten minute long data snippet that highlights the two types

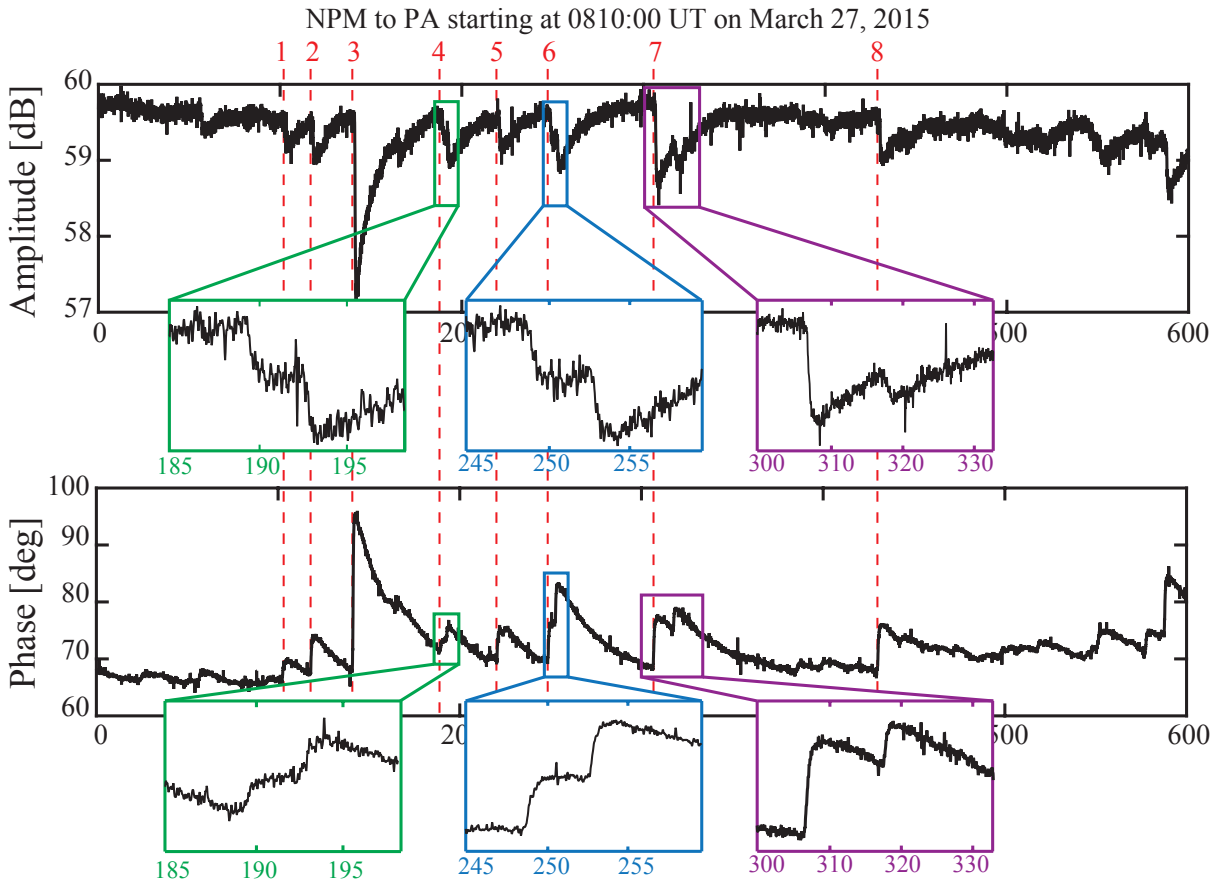

Figure 3-3. A ten minute data sample of conjugate overlapped events observed at 08:10 UT on March 27, 2015. The events are numbered with the red dashed lines to indicate when each event begins. Event 4 and Event 6 show onset duration overlap and Event 7 recovery overlap.

of overlapping events in both amplitude and phase. Event 7 clearly exhibits recovery stage overlap, where the overlapping event starts after the first event has transitioned to the recovery stage. Events 4 and 6 exhibit onset overlap, where the second event occurs before the first event exhibits any discernible form of recovery. In this document, only the recovery stage overlapping events are considered candidates for sequential scattered field analysis which can disentangle overlapping events.

The total field of overlapping events at the receiver is considered as the sum of the ambient field and multiple scattered fields. Note again that the ambient field can be obtained by subtracting the scattered field from the total field. Therefore, we model the recovery

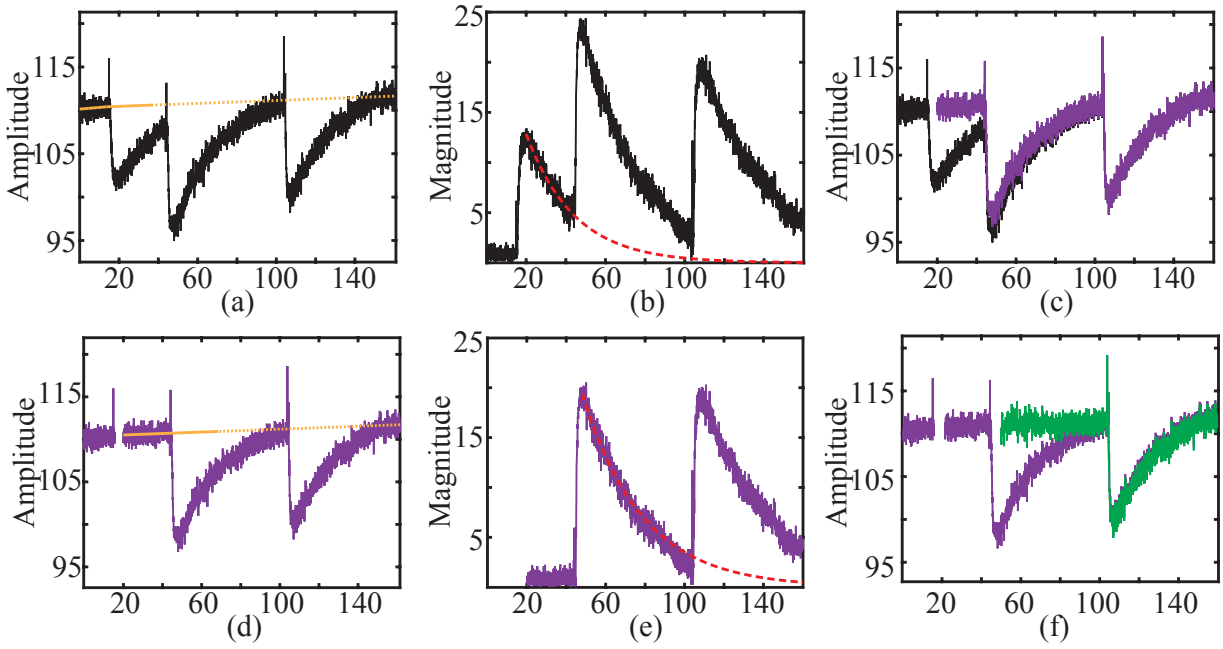

Figure 3-4. Sequential scatter field analysis process for VLF amplitude signal to disentangle overlapping LEP events.

portion of the scattered field and subtract it from the total field. The event recovery is modeled using the initial rate before the event is interrupted by the next event (Figure 3-4b). The recovery is modeled as exponential using the SFM signal and linearly using the scattered field angle. The complex-valued modeled recovery is then subtracted from the complex-valued total field signal to separate out the preceding event (Figure 3-4c) and identify the ambient field for the subsequent event (Figure 3-4d). This sequential process is repeated for each of the following events (Figure 3-4e and Figure 3-4f). Figure 3-5 shows the total field amplitude and phase before and after the subtraction of the 8 overlapping conjugate events detected on March 23, 2015 at 08:48 UT. By isolating the preceding event, the pre-onset and onset duration portions of the subsequent event are revealed, which allows the precise quantification of the onset time and onset duration of the subsequent event. One limitation of this method is that the onset duration of the scattered field magnitude is not modeled, resulting in gaps in the restored ambient field.

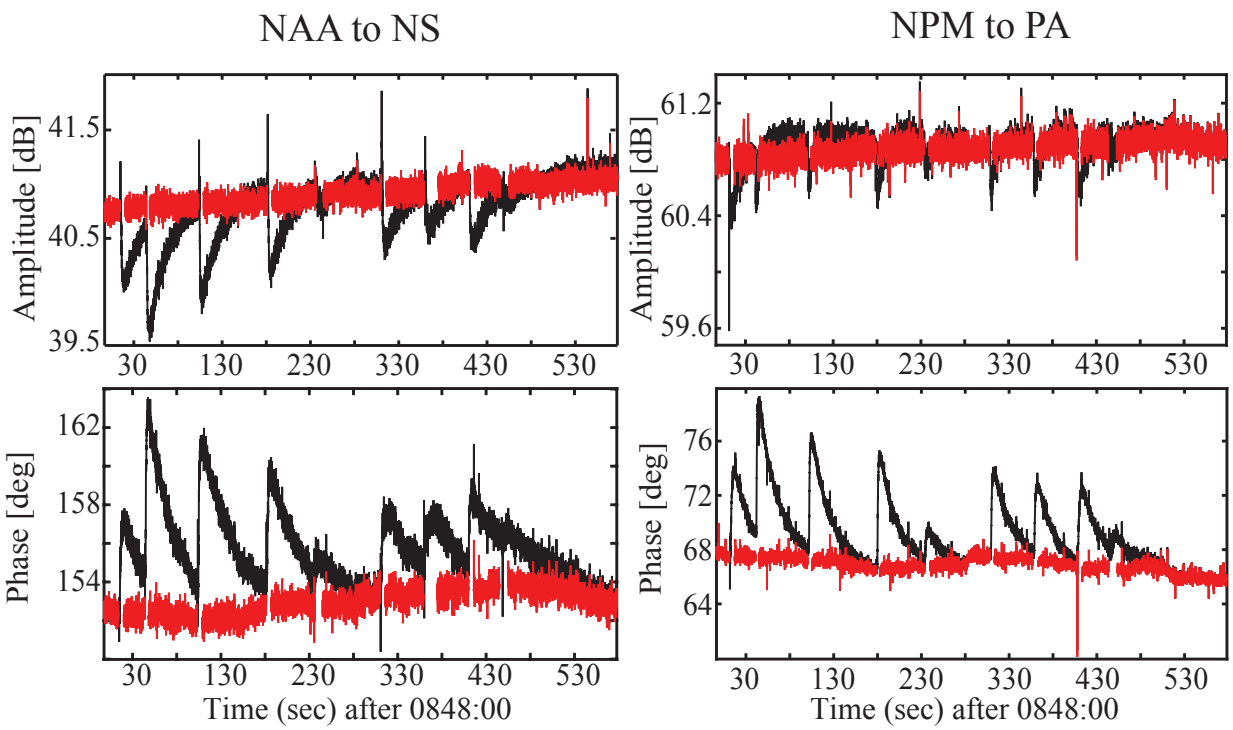

Figure 3-5. Conjugate overlapping LEP events on March 23, 2015 at 08:48 UT show the amplitude and phase perturbations in black. The red shows the ambient and phase fields reconstructed using the overlap scattered field analysis.

3.4 Statistical Analysis

The statistical analysis presented herein is divided into two sections, depending on whether the LEP event property is potentially affected by the timing of magnetospheric processes.

3.4.1 Onset Time, Onset Delay, and Onset Duration

LEP event onset time, onset delay, and onset duration are likely to be affected by the timing of magnetospheric processes. Because the two different receiver sites experience different SNR's, it is difficult to immediately identify the method that best represents the timing properties we seek to extract. Three methods were applied to determine the onset time and four methods were applied to determine the onset duration. The first method defines the onset time as the 10% point of the maximum amplitude change and the onset duration as the time between the 10% and the 90% of the maximum amplitude change. This method is the same as that presented by *Cotts et al.* (2011). The second method is to quantify the 10%

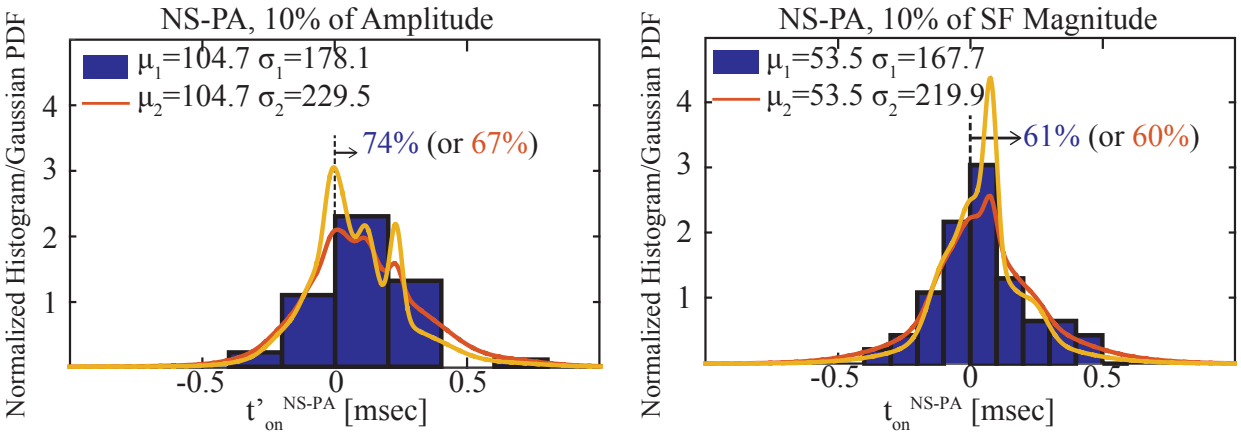

Figure 3-6. Onset Time Difference Statistics. (a) 10% of Amplitude and (b) 10% of Magnitude

onset time and the 10% to 90% onset duration using scattered field magnitude instead of total field amplitude. For the two methods described above, the error bar is set using the pre-event standard deviation, assuming that pre-event noise level remains the same throughout the event. The third method measures the 10% onset time and the 10% to 90% onset duration of an n^{th}-order polynomial regression using the magnitude of the normalized scattered field. n is selected by eye to reject sferic impulses and provide some measure of noise rejection. This method finds a close fit to the entire LEP signature (from onset to recovery). The 1-σ confidence intervals are applied to provide one standard deviation error bars on the fitting curve. The fourth method for the onset duration quantifies the time between the onset time and the pre-decay time using the scattered field magnitude. This method characterizes the effective duration of the precipitation burst. Deviation from the exponential recovery fit determines the pre-decay time.

Figure 3-6 presents the statistical results for onset time differences between receivers using the two methods. If the onset time difference, $NS - PA$, is positive, it indicates that LEP events occur earlier at PA, and this is found to be the case for all three methods. Figure 3-6a shows that, based on the amplitude-only measurements, 74% (or 67%) of the conjugate LEP events started earlier at PA, and on average the event at PA preceded the event at NS by 104 $\pm$ 178 ms (or 104 $\pm$ 229 ms). Method 2, which employs scattered field analysis, shows that

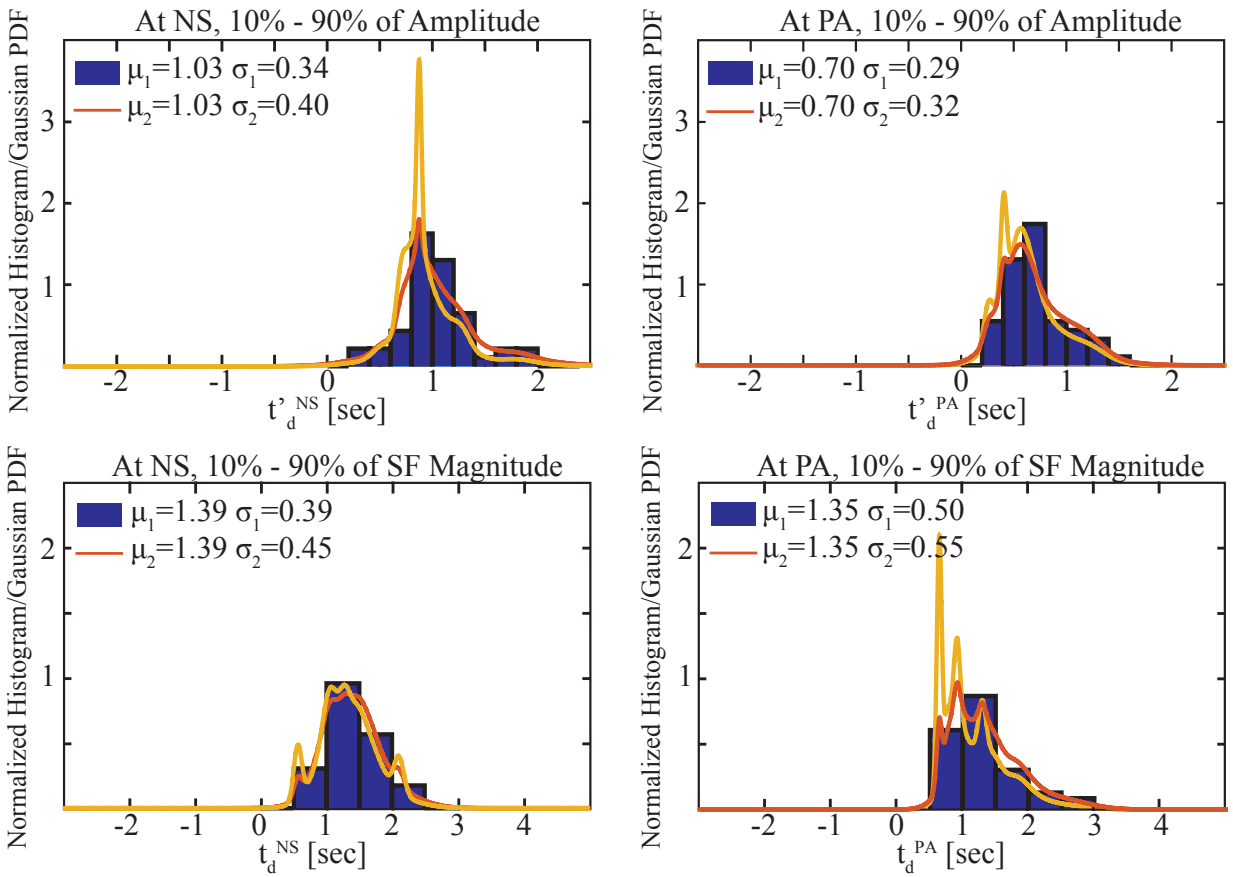

Figure 3-7. Onset duration and onset duration difference statistics.

only 61% of the conjugate events started earlier at PA, and the average time difference was 53 $\pm$ 219 ms (Figure 3-6b). Method 3, using the nth-order regression, the results for which are not shown, calculated that 63% of the events started earlier at PA, and on average the time difference was 36 $\pm$ 160 ms, which is similar to Method 2.

Within the context provided by previous observations of conjugate LEP events (*Burgess and Inan*, 1990; *Cotts et al.*, 2011; *Golkowski et al.*, 2014), these onset delay observations are particularly revealing. Most of the lightning flashes associated with these events are off the coast of South Carolina, aligning with the "Eastern" groups of previous works. Nevertheless, amplitude-only onset delay differences of 104 $\pm$ 178 ms are much smaller (by a factor of 2) than those observed by *Burgess and Inan* (1990), *Cotts et al.* (2011), and even *Golkowski et al.* (2014), and when scattered field magnitude onset delay differences are used, the difference

is smaller by another factor of 2. These observations do not match the timing predicted by atmospheric backscatter (*Cotts et al.*, 2011); they are too small by a factor of 2−4. These results are not so surprising when one considers that the observations shared by *Burgess and Inan* (1990) also do not align with the predictions of the atmospheric backscatter model, in that the relative onset timing delays of the western group were shorter than those of the eastern group by ∼0.2 seconds. In fact, *Burgess and Inan* (1990) showed that the southern hemisphere onset delays were shorter for the western group than for the eastern group, whereas the northern hemisphere delays were relatively unaffected by longitude. None of these observations are consistent with the predictions of the atmospheric backscatter model, but they may be consistent with timing delays produced by the observation geometry, as will be discussed in Section 3.5.

Regarding onset duration observations, from the statistical results, it is observed that all four calculation methods consistently show longer onset durations at NS than at PA. Figure 3-7 only presents the statistics calculated using the first two methods: the amplitude-only measurements and the scattered field magnitude measurements. The average onset duration at NS and at PA is 1.03 sec and 0.70 sec when measured on the amplitude signals, while it is 1.39 sec and 1.35 sec when measured using SFM. It is interesting to note that the onset durations in both hemispheres are extremely similar when scattered field analysis is employed, and they exhibit >30% differences when amplitude-only analysis is used. This result is reflected in the statistic that 80% of the events experience the longer onset durations at NS when measured using amplitude, whereas only 61% of the events exhibit longer onset durations at NS when calculated using SFM. Table 3-1 summarizes the statistical mean values of the onset durations and the probability of longer precipitation at NS, assuming Gaussian noise distributions. While Method 2 quantifies the SFM onset duration, electrons continue to precipitate until the event begins to recover. Method 4 quantifies the total length of time over which electron precipitation meaningfully occurs. Method 2 and Method 4 can be meaningfully compared to evaluate the persistence of electron precipitation near the VLF reflection height.

Table 3-1. Statistical mean values of the onset duration using four methods

Onset duration	NS	PA	Stats. Probability*
Method 1	1.03	0.70	80.2%
Method 2	1.39	1.35	61.1%
Method 3	1.78	1.61	80.2%
Method 4	6.42	4.83	70%

*: Statistical probability for the electrons to precipitate longer at NS than at PA.

The statistical comparisons show that the conjugate LEPs stay at the maximum for 1.55 seconds longer at NS before they begin to decay than at PA.

The opposite results were observed by *Cotts et al.* (2011): for the eastern group, onset durations calculated using amplitude observations were shorter in the northern hemisphere by $\sim$0.3 seconds. *Golkowski et al.* (2014), on the other hand, determined that the observed LEP onset durations (also for an eastern group) were not significantly different between the two hemispheres. Together, observations now demonstrate that the onset duration differences between hemispheres vary from $+0.3$ seconds to 0.0 seconds to -0.3 seconds. It does not appear that these raw observations are consistent with any magnetospheric property. Instead, it is possible they are significantly affected by the VLF scattering observation geometry in relation to the ionospheric disturbance, as will be discussed in Section 3.5.

3.4.2 Maximum Perturbations and Recovery Time

The statistics on the maximum amplitude, phase, and magnitude deviations and recovery rate are listed in Table 3-2. The statistics on the maximum scattered field angle change are not shown in this paper. It is observed that the maximum amplitude change at NS is larger than at PA by 0.15 dB and that 69% of the events had larger maximum amplitude change at NS. However, when considering amplitude and phase signals together, 90% of the conjugate events had a larger scattered field magnitude change at PA than at NS in part due to the 5.29° larger maximum phase change at PA.

In past work, the recovery time was defined using the amplitude signal as the time between the end of the onset duration and when the amplitude returns the 10% of the ambient field (*Cotts et al.*, 2011). Instead, this work uses the exponential recovery rate to quantify the

Table 3-2. Statistics on other properties

	NS	PA
Max. Amplitude [dB]	0.82 ± 0.37	0.67 ± 0.38
Max. Phase [deg]	4.94 ± 3.93	10.23 ± 5.85
Max. Magnitude	0.12 ± 0.06	0.18 ± 0.09
Recovery Rate [sec]	27.98 ± 14.45	21.62 ± 4.44

recovery time. The exponential recovery rate is the time between the pre-decay point and the e-folding of the maximum scattered-field magnitude. One sigma confidence interval is applied to find the standard deviation of the recovery rate. It is observed that the LEP events at NS took 27.98 seconds to recover to the e-folding point, whereas the conjugate events at PA took 21.62 seconds. 71% of the conjugate events took longer to recover at NS.

3.4.3 Dependence on Causative Lightning Flash Location

The dependence of the LEP timing properties on the latitude and longitude of the causative lightning flashes has been investigated. Table 3-3 compares onset times, onset durations, and maximum signal deflections observed for lightning flashes source in the northern and southern hemispheres. Table 3-3 provides the results calculated using amplitude-only and scattered field magnitude observations. The primed quantities (left) are measured using amplitude-only observations whereas the unprimed quantities (right) are measured using scattered field magnitude observations. Although most of the lightning flashes originated in the northern hemisphere, no clear dependence on the hemisphere of the causative lightning flash is observed. No matter where the causative lightning flash launches whistlers, LEP events tend to occur at PA first, have a larger magnitude perturbation at PA, and exhibit a longer impact at NS.

Figure 3-8 investigates the geomagnetic locations of the causative lightning flashes versus the onset time difference ($t_{on,NS} - t_{on,PA}$) and onset duration difference ($t_{d,NS} - t_{d,PA}$). Figure 3-8 shows the first order poly-fit lines to quantify any longitudinal or latitudinal dependance; the slope of each fit is shown on the graph. The black dashed lines are the fits considering all of the locations and the supporting lines (blue and green dashed lines) are the

Table 3-3. LEP properties associated with causative lightning origins

$t_{on}^{'}$	NS First	PA First	t_{on}	NS First	PA First	Total
Northern Lightning	15	29	Northern Lightning	21	23	44
Southern Lightning	0	2	Southern Lightning	1	1	2
Total	15	31	Total	22	24	46
$t_{d}^{'}$	NS Longer	PA Longer	t_{d}	NS Longer	PA Longer	Total
Northern Lightning	40	4	Northern Lightning	31	13	44
Southern Lightning	2	0	Southern Lightning	0	2	2
Total	42	4	Total	31	15	46
ΔA	NS Bigger	PA Bigger	ΔM	NS Bigger	PA Bigger	Total
Northern Lightning	31	13	Northern Lightning	4	40	44
Southern Lightning	1	1	Southern Lightning	1	1	2
Total	32	14	Total	5	41	46

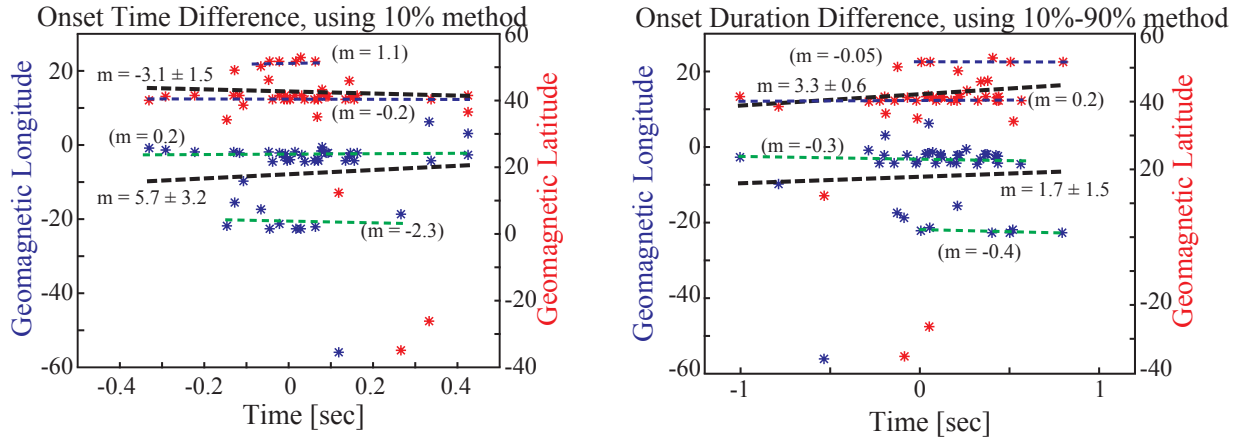

Figure 3-8. Onset time and onset duration difference have no dependance on geomagnetic latitude and longitude of causative lightning flashes.

fits for the clustered groups. The supporting lines exhibit no significant dependance on the geomagnetic latitude or longitude. Only a very subtle dependance of the onset time difference on the longitude is observed (blue on the left panel of Figure 3-8), and we are unsure if it is statistically meaningful. It may be the case that the onset time difference and the onset duration difference depend on the geomagnetic latitude and/or longitude of the whistler launch point, rather than on that of the causative lightning flash, but our data do not address this point.

3.5 Comparisons with Modeling

To compare inter-hemispheric onset times shown in the statistical results, the NAA-NS and NPM-PA propagation paths are simulated using the LEP Event modeling framework discussed in Chapter 2. Onset times at the conjugate points located on and off the great circle path (GCP) are chosen and the simulation results are compared with the statistical analysis.

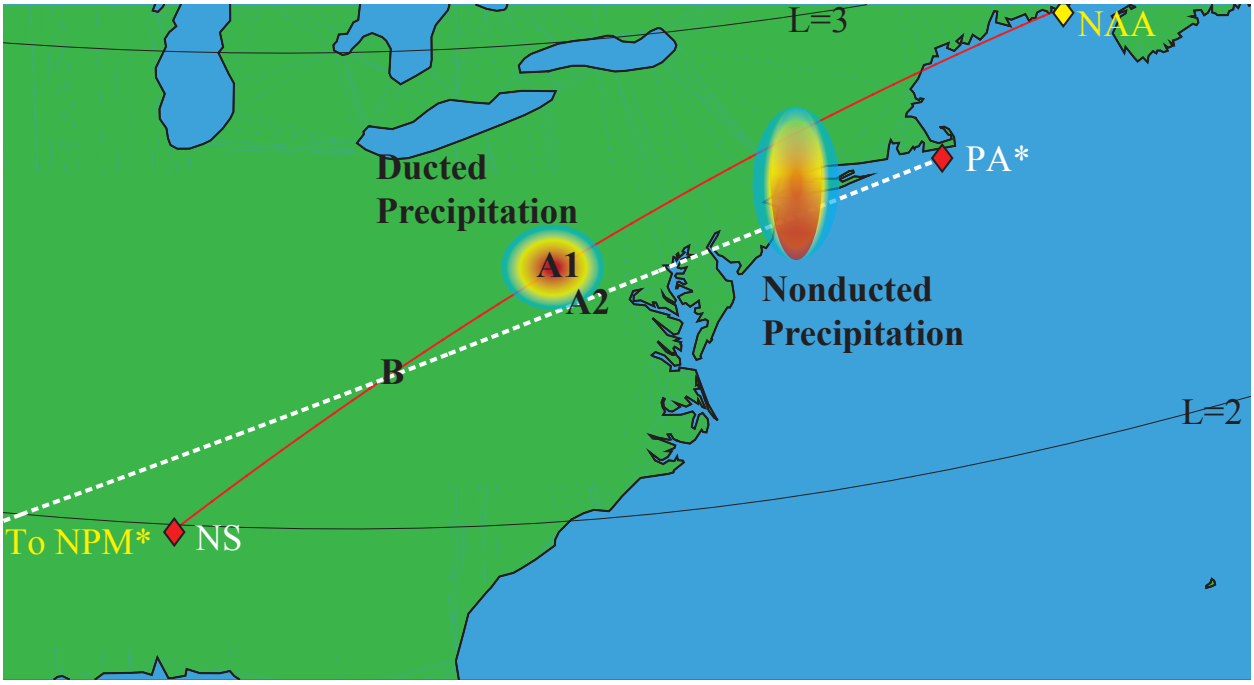

Figure 3-9. Ducted and nonducted disturbance perspectives with various disturbance locations which are on/off NAA-NS and conjugate path of NPM-PA.

Figure 3-9 shows a map to evaluate inter-hemispheric timing for three disturbance locations: Location A1 is directly on the NAA-NS propagation path but off the conjugate propagation path of NPM-PA by approximately 100 km; Location A2 is on the conjugate propagation path of NPM-PA and 100 km away from the NAA-NS path; and Location B lies on both paths and is used as a reference point to remove any magnetospheric time effects calculated by the WIPP code but that do not apply to this analysis. Generally, WIPP results exhibit earlier onset times in northern hemisphere. Previous work (*Cotts et al.*, 2011) accounted for atmospheric backscatter effect with Monte Carlo results to show earlier event onsets in the southern hemisphere. In this work, in order to purely determine the spatial effect

on inter-hemispheric timing, the modeled VLF scattering events at A1 and A2 are shifted in time by the onset time delay of Location B.

Figure 3-9 also shows an illustration of a nonducted precipitation event. The color-scheme of the disturbance from red to blue represents the poleward displacement with time. If the disturbance is located eastwards of the crossing point, Location B (as shown on the figure), the LEP event would exhibit onsets earlier in the southern hemisphere on the conjugate path of NPM-PA than the northern hemisphere, as the disturbance would move poleward. If the nonducted disturbance were located westward of Location B, the LEP event would exhibit onset times earlier in the northern hemisphere than the southern hemisphere.

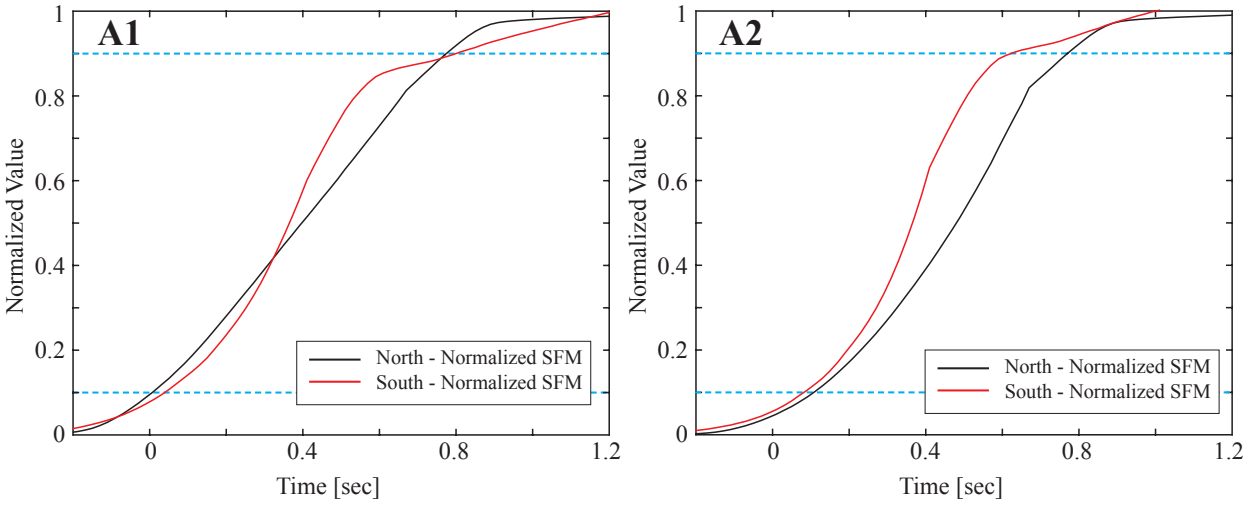

Figure 3-10. Inter-hemispheric time analysis at Locations A1 and A2.

To determine the inter-hemispheric onset time for the ducted perspective, the disturbance is simulated as a localized event whose radius increases with time at Locations A1 and A2 in both northern and southern hemispheres. The FWHM increases from ~80 km at 0 seconds to ~150 km at 1 second and stays at the maximum FWHM afterwards. The left panel of Figure 3-10 shows the normalized SFM due to the disturbance at A1 and the right panel shows at A2, both shifted by the onset delay of the reference point, B. At A1, the onset is earlier in the northern hemisphere.

The normalized SFM observed in the northern hemisphere is 0 at the onset time (defined as 10% point of the maximum) because A1 and B are both located on the NAA-NS propagation path, and there is no time difference in the normalized SFM. In the southern hemisphere, however, Location A1 is 100 km off the NPM-PA GCP; thus there is an onset time delay on the normalized SFM. At Location A1, the northern hemisphere event onset occurs earlier by ∼40 ms using normalized SFM. At A2, the onset occurs earlier in the southern hemisphere because A2 is 100 km off the northern propagation path but directly on the southern path. The onset difference between north and south is −30 ms using the normalized SFM, indicating the southern hemisphere onset is earlier. Between Locations A1 and A2, there is a ∼70 msec time shift of relative onset time.

Based on these modeling results, it is clear that the geometry of the disturbance and the propagation path can significantly affect the observed event onset timing. As the location of the disturbance moves farther from the propagation path, the onset time becomes later. Therefore, the geometry can determine which hemisphere begins to exhibit event onsets earlier, regardless if the event is ducted or nonducted.

3.6 Discussion and Summary

In this chapter, 46 simultaneously observed conjugate LEP events were analyzed. LEP events were categorized into isolated and overlapped events, and scattered field analysis was applied accordingly to rigorously quantify LEP characteristics. Various statistical methods and error analysis were introduced for amplitude only and scattered field magnitude signals. Experimental observations are consistent with the theoretical conclusion presented in Chapter 2 that scattered field analysis is more directly related to the properties of the ionsopheric disturbance than amplitude observations.

The onset time statistics based on the amplitude signals were consistent with past work (*Burgess and Inan*, 1990; *Cotts et al.*, 2011; *Golkowski et al.*, 2014) in that that the LEP events started earlier in the southern hemisphere, but a delay of only ∼100 msec was observed, rather than 200 msec. The onset time statistics measured using the scattered field magnitude

exhibited a much shorter 50 msec time difference. Observations do not appear to support the previously posed atmospheric backscatter theory as reasonably responsible for the observed timing differences.

While past work (*Cotts et al.*, 2011) observed longer onset durations in the southern hemisphere using amplitude observations, onset durations presented herein were longer in the northern hemisphere whether the statistics were calculated using the amplitude or the scattered field magnitude. The discrepancy between past and present work may exist because the past work did not make simultaneous conjugate observations, but it also may exist because the observation geometry affects the onset duration observation.

Collectively, it does not appear possible that the onset timing and duration observations can be explained using the ionospheric backscatter mechanism (*Cotts et al.*, 2011). The timing differences between hemispheres do not align with predictions and are even at odds with previous observations. Instead, the onset time and duration statistics presented herein indicate that another physical process is needed to explain observations. Consideration of the spatio-temporal development of the ionospheric disturbances in the conjugate hemispheres, relative to the locations of the great-circle propagation paths of the VLF waves appears to be a strong candidate to explain these conflicting observations. This possibility will be further evaluated in Chapter 4.

CHAPTER 4
SPATIO-TEMPORAL DEVELOPMENT OF DUCTED AND NON-DUCTED LEP EVENTS

The statistics presented in Chapter 3 are not consistent with theories that attempt to explain interhemispheric timing differences among LEP events. The statistics seem to indicate that observation geometry factors might be involved in the interhemispheric timing differences, but nothing conclusive can be gleaned from the statistics in this regard. The experimental observations and theoretical calculations presented in this chapter, on the other hand, directly address the effects of the spatio-temporal development of LEP events on interhemispheric timing calculations.

Two cases of conjugate LEP events that exhibit different developments are observed and discussed with an emphasis on interhemispheric timing differences. The first case exhibits standard poleward displacement of precipitation in the northern and southern hemispheres by detecting increased onset delay as L-shell values increase. This first case matches theoretical predictions for nonducted LEP events in the northern as well as the southern hemisphere. The second case, however, exhibits increasing onset delays as the precipitation expands radially from a central location. This unusual development of the electron precipitation is reported and discussed in this chapter. Using the modeling framework developed in Chapter 2, the radial expansion of the LEP disturbance is simulated and compared with experimental observations.

This chapter progresses as follows: Section 4.1 describes the observational geometry (i.e., the layout of the VLF transmitters and receivers) used for this chapter, Section 4.2 presents experimental observations for the two conjugate LEP cases detected on multiple propagation paths, Section 4.3 discusses the observations in the context of modeling simulations that explain the radial expansion of the observed precipitation, and lastly Section 4.4 summarizes the results of the chapter.

4.1 Description of the Experiment

The University of Florida North American VLF array (NAV) is distributed to track four US navy transmitters, NLK, NPM, NLM, and NAA, as shown in Figure 4-1. The receiving

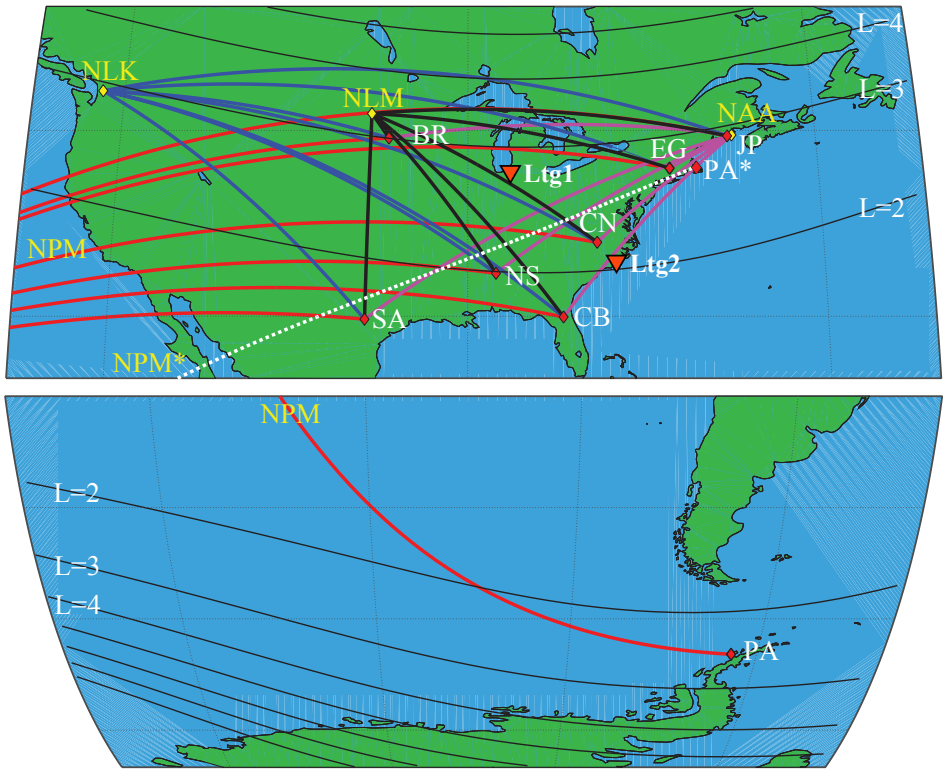

Figure 4-1. Northern hemisphere (top) and southern hemisphere (bottom) maps with transmitter-receiver great circle paths (GCPs). NPM (red), NLK (blue), NLM (black), and NAA (purple) transmitters are tracked at eight VLF receivers. The conjugate path of the southern hemisphere path, NPM-PA, is shown with the white dotted line.

antennas are located at Florida (CB), North Carolina (CN), Connecticut (EG), Maine (JP), South Dakota (BR), Alabama (NS), and Texas (SA) in the northern hemisphere and Palmer station, Antarctica (PA) in the southern hemisphere. The details of the VLF transmitters and receivers are tabulated in Table 4-1 and Table 4-2.

The NAV array produces a mesh grid of GCPs for each transmitter-receiver pair, collectively allowing for the evaluation of the spatial and temporal development of lightning-associated ionospheric disturbances. The mesh grid of GCPs covers the range between L-shell values of 2 and 3, which is where the majority of lightning precipitations occurs. The NPM-PA GCP covers the conjugate region of the NAV mesh in the northern hemisphere, and its conjugate path is plotted with the white dotted line on Figure 4-1.

Table 4-1. Navy VLF Transmitters tracked in the experiment.

Call Sign	Location	Frequency	Coordinates
NLK	Washington, USA	24.8 kHz	48.2°N 121.9°W
NPM	Hawaii, USA	21.4 kHz	21.4°N 158.1°W
NLM	North Dakota, USA	25.2 kHz	46.3°N 98.3°W
NAA	Maine, USA	24.0 kHz	44.6°N 67.2°W

Table 4-2. UF VLF Receivers used in the experiment.

Call Sign	Location	Coordinates
CB	Camp Blanding, Florida	29.9°N 82.0°W
CN	Chapel Hill, North Carolina	35.9°N 79.0°W
EG	East Granby, Connecticut	41.9°N 72.7°W
JP	Jonesport, Maine	44.5°N 67.2°W
BR	Brookings, South Dakota	44.3°N 96.8°W
NS	Northside, Alabama	33.4°N 87.6°W
SA	San Antonio, Texas	29.7°N 98.5°W
PA	Palmer Staion, Antarctica	64.7°S 64.0°W

The received signals are processed in order to rigorously analyze and compare LEP events signatures obtained by tracking different VLF transmitters. The north-south and east-west channels at each site are combined and rotated in post-processing into the direction of the transmitter, after which the scattered field analysis technique is applied (as explained in detail in Chapter 3). Then, for comparison purposes, it is normalized again between 0 and 1 by averaging the maximum perturbation value for a half second and dividing the SFM signals by its maximum average value.

4.2 Experimental Observations

In this section, two cases of spatio-temporal variations of electron precipitations are reported. The first case occurred on October 20, 2016 and the second case on August 23, 2017. The two cases were caused by significant lightning strikes (peak current of 254 kA and -214 kA, respectively). Detailed observations for each case follow.

4.2.1 Case 1; October 20, 2016

There was a lightning flash at 04:32:19.6 UT on 20 October 2016. According to the U.S. National Lightning Detection Network (NLDN) (*Cummins et al.*, 1998), this causative lightning flash occurred at a latitude of 40.5° N and a longitude of 86.2° W and had a peak

current of +254 kA. The location is marked on Figure 4-1 as *Ltg1*. Three transmitter-receiver paths on the NAV array registered the LEP event associated with this lightning flash, and two additional paths registered so-called early VLF events. Early VLF events are not of primary interest for this document, so they are excluded from this analysis. In the northern hemisphere, the LEP event perturbation occurred on the NLM signal observed at two receiver sites, CB and EG (NLM-CB and NLM-EG). No events were registered for the other transmitter signals, NAA, NPM, and NLK, other than the early event on NLK-CN. BR was experiencing local interference at that moment, and it is excluded from this experiment.

Figure 4-2a presents the amplitude and phase changes of the VLF perturbations on the NLM transmitter. CB and EG sites show clear amplitude and phase changes typical of LEP event signatures, whereas an early VLF event is detected at CN. JP and SA do not show any sign of perturbations. In the southern hemisphere, the conjugate LEP event was detected on the NPM-PA path (Figure 4-2b).

Figure 4-3 focuses on the three LEP observations made for Case 1. Figure 4-3a shows the transient LEP signatures normalized and zoomed in to the LEP event onset. Figure 4-3b shows the superposition of the three events for detailed comparison. This figure explicitly exhibits the onset time delay as a function of receiver site, and the order of the onset times are NLM-CB (Blue), NPM-PA (Orange), and NLM-EG (Yellow). Note that not detecting events also means that the precipitation did not perturb the paths. Comparing the onset times between the LEP events implies that the first precipitation happened at CB in the northern hemisphere, second at PA in the southern hemisphere, and last at EG in the northern hemisphere. The first precipitation (NLM-CB) started at lower latitude than the causative sferic (40.5° N). This unusual spatial relationship implies that either the lightning EMP propagated southward and coupled to the magnetosphere at a lower L-shell, or that the lower frequency content of the whistler could have refracted into the lower L-shell in the magnetosphere and precipitated more southerly than the causative sferic. This sferic was identified by NLDN, and the source was confirmed using NAV array broadband receivers. No other strong lightning discharges were

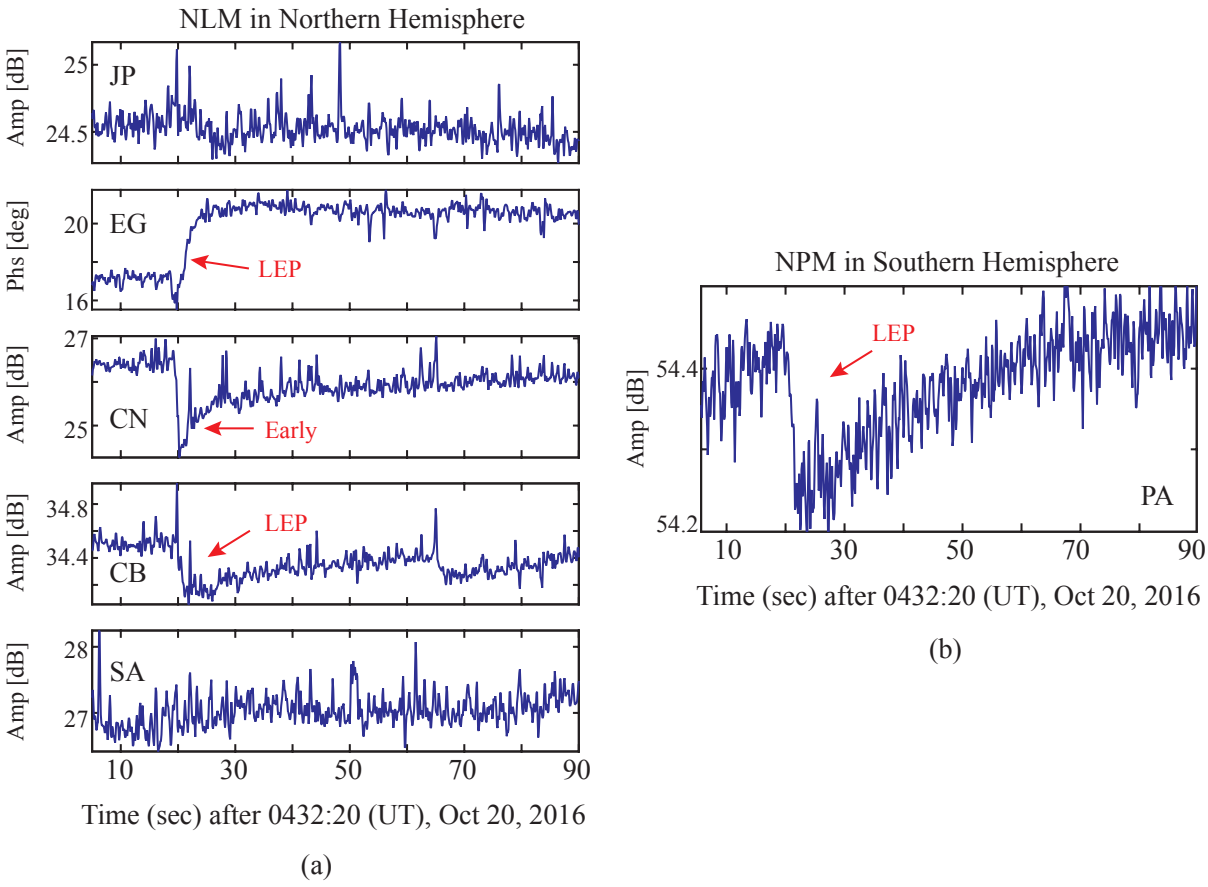

Figure 4-2. Observations of the NLM transmitter signal. Two LEP events and one Early event detected.

observed within 2 seconds by either NLDN or the NAV array receivers. A weak signature of a whistler was recorded at PA (Figure 4-3c), indicating that ducts were present at the time, although this particular precipitation event was not likely caused by a ducted whistler.

There is approximately a half second time difference between NLM-CB (first) and NLM-EG (last) in the northern hemisphere. The propagation path of NLM-EG is at a higher latitude and L-shell (approximately L-shell of 3.1 at the same longitude as *Ltg1*) than the path of NLM-CB (approximately L-shell of 2.1 at the same longitude as *Ltg1*). The increased time delay seen at NLM-EG at a higher latitude than NLM-CB implies the poleward displacement of the precipitation over time. This poleward displacement of the precipitation patch is consistent with the past work with non-ducted whistler waves.

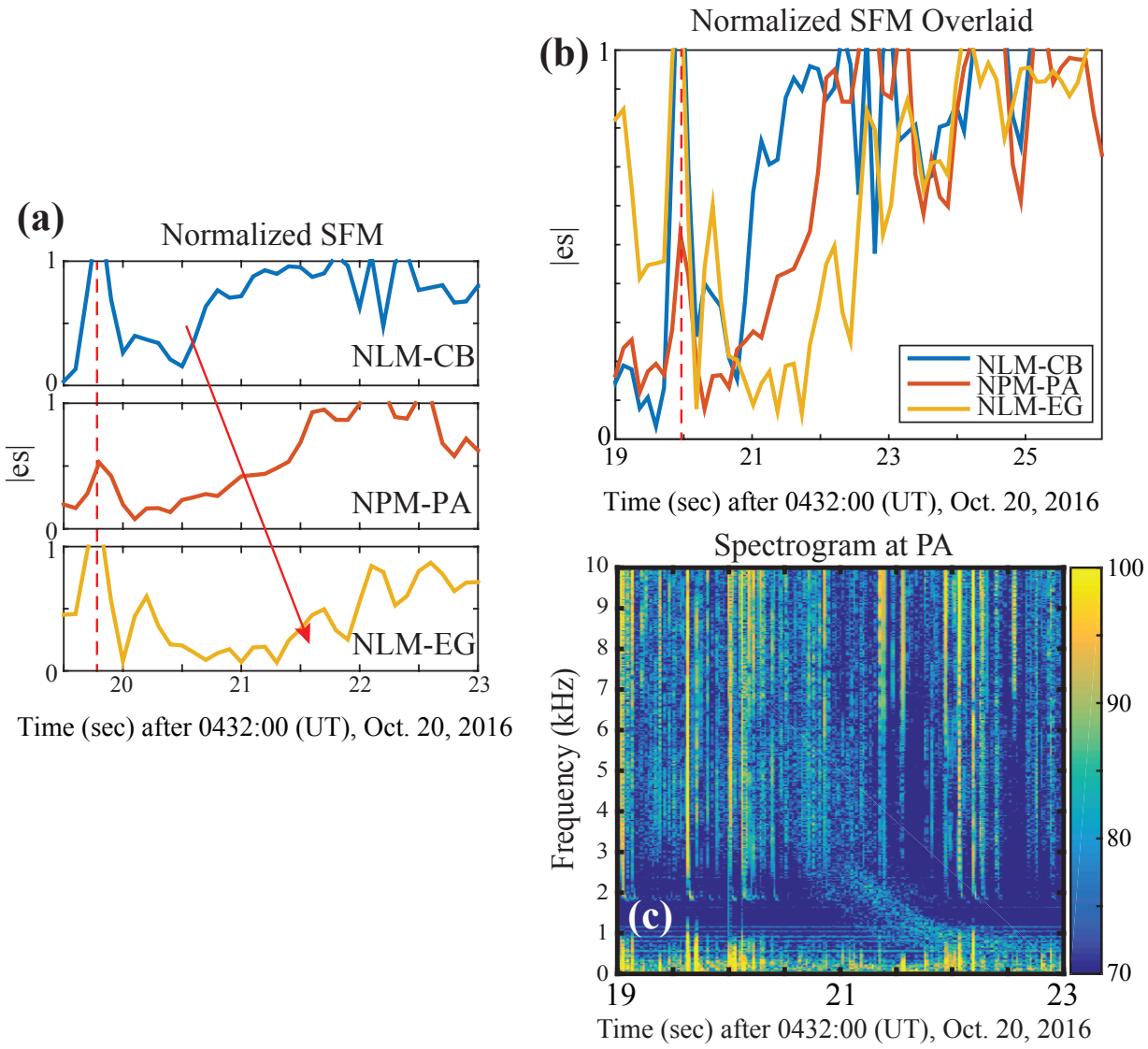

Figure 4-3. Three LEP events are overlaid to show the onset time delay

Definitive observations of conjugate non-ducted LEP events have not previously been reported, however. The NLM-PA conjugate propagation path lies between NLM-CB and NLM-EG at the longitude of *Ltg1*. As expected, the LEP event perturbation on the NLM-PA path occurs after the NLM-CB event onset and before the NLM-EG event onset. These observations are perfectly consistent with standard non-ducted precipitation event predictions of the WIPP code exhibiting poleward displacement of the ionospheric disturbance over time.

It should be clear that for non-ducted LEP events, as the event moves poleward over time, different VLF propagation paths register the event as a function of time. For interhemispheric timing purposes, it would thus be important to account for the location of the VLF propagation path (in L-shell) in the longitudinal plane of the event. If northern and southern hemisphere propagation paths cross the longitudinal plane of the event at different L-shells, the interhemispheric timing may very well be affected by the difference in L-shell.

4.2.2 Case 2; August 23, 2017

For Case 2, the causative lightning flash occurred at 08:42:02.8 UT on 23 August 2017 at a latitude of 34.1° N and a longitude of 77.4° W with a peak current of −214 kA, according to NLDN. The location of the lightning flash is indicated in Figure 4-1 as *Ltg2*. In the northern hemisphere, LEP events were detected on the NAA transmitter signal at the receiver sites of SA, NS, and CN and on the NLM transmitter at CN. Early events were observed on the NAA-CB path. In the southern hemisphere, the conjugate LEP was detected on the NPM-PA path. Figure 4-4a shows the NAA amplitude at different northern hemisphere sites in order to show the VLF perturbations. CN, NS, and SA sites show clear amplitude changes during the LEP event, while an early event is detected at CB. Figure 4-4b presents the phase change of the NLM-CN signal caused by the LEP event. Note that at the receiver site CN, LEP signatures are recorded on two transmitter signals: NAA and NLM, nearly simultaneously. In Figure 4-4c, the amplitude deviation of NPM at PA is presented for the conjugate event.

The normalized scattered field magnitude signals are presented in Figure 4-5. Figure 4-5a shows the five normalized LEP events zoomed to the event onset, and the red arrow approximately marks each onset time. Figure 4-5b is the superposition of the normalized events with the vertical dashed line showing the sferic intrusions. The first deviation associated with this LEP event occurred on the NAA-SA and the NAA-NS paths (blue and orange) at the same time. The second perturbation happened at the same time on the NLM-CN path in the northern hemisphere (yellow) and on the NPM-PA path in the southern hemisphere (purple). The event observed on the NAA-CN path occurred last in the northern hemisphere (green).

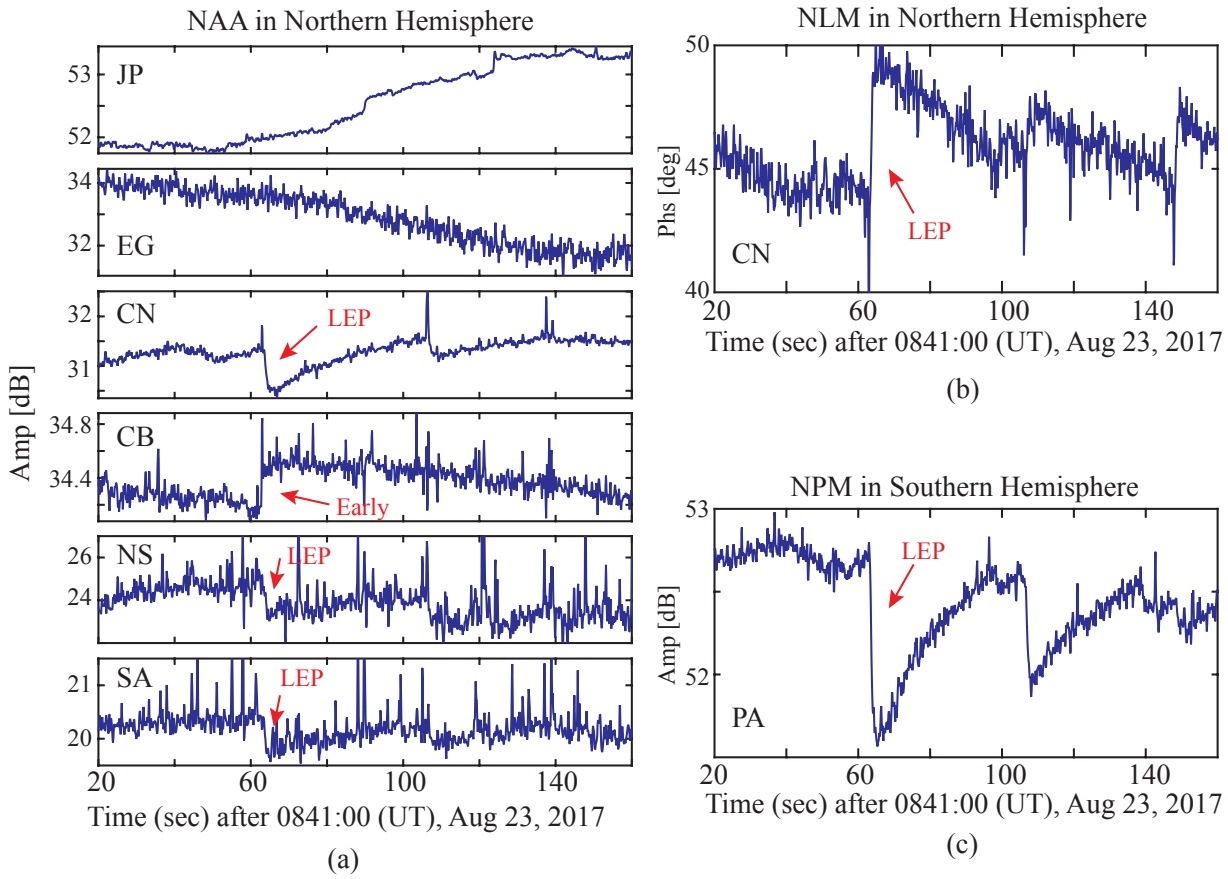

Figure 4-4. Observations of the NAA transmitter signal. Four LEP events and one Early event detected.

The onset time difference between NAA-NS (or NAA-SA) and NLM-CN is measured to be 100 msec, between NAA-NS and NPM-PA 150 msec, and between NAA-NS and NAA-CN 300 msec. This onset time is measured at 20% point of the maximum perturbation since some of the 10% points were not clear. A strong whistler was recorded at PA (Figure 4-5c), indicating that ducts were present at the time of this event.

These observations do not immediately indicate poleward displacement or another clear variation with space and time. We investigate this case with detailed modeling (as described in Chapter 2) to show that it in fact follows the simple geometric pattern of a radial expansion from a central location.

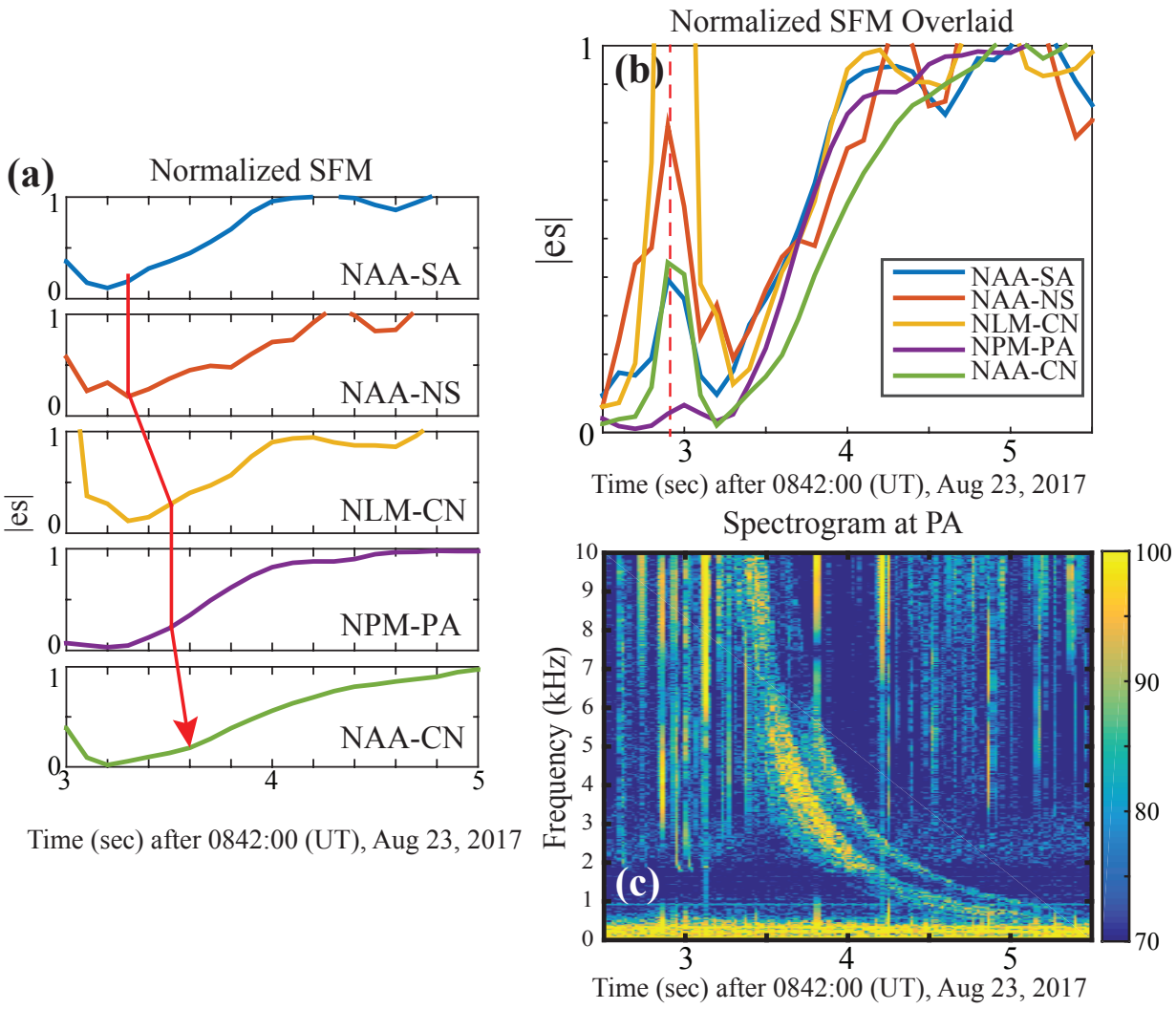

Figure 4-5. Three LEP events are overlaid to show the onset time delay

4.3 Ducted and Non-Ducted Modeling for Case 2

The type of poleward displacement observations presented for Case 1 have been simulated, observed, and discussed in multiple past works (*Johnson et al.*, 1999; *Peter and Inan*, 2004). The signatures observed for in Case 2 have not previously been investigated, however. For Case 2, we consider ducted and non-ducted perspectives to simulate the event onset observations.

If Case 2 were to be a non-ducted LEP event, the disturbance would have precipitated with advancing poleward time delays. Figure 4-6 shows the hypothetical map if Case 2 would have been produced by non-ducted precipitations: at the same longitude as the causative

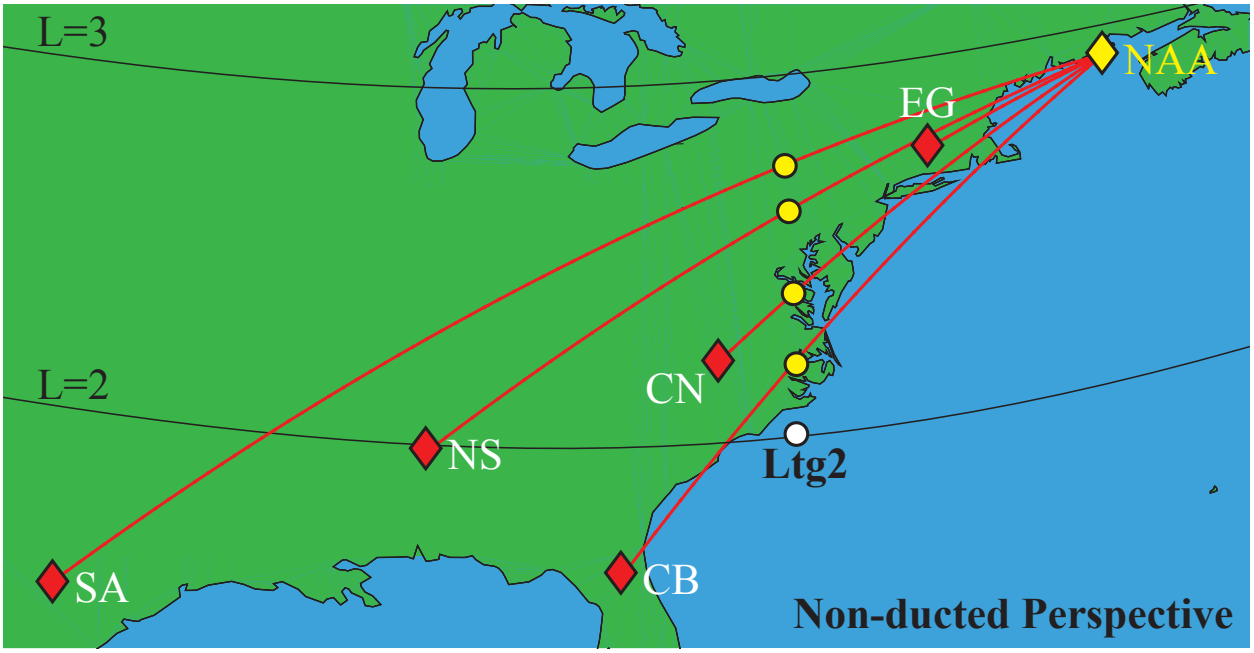

Figure 4-6. Illustration map of the poleward disturbance for Case 2 modeling, if it were non-ducted. The poleward disturbance is located on each respective GCPs with yellow circles.

spheric, *Ltg2*, as time advances, the event perturbations occur on propagation paths at higher L-shells. To simulate this hypothetical situation, the electron density profiles are calculated at each L-shell using the WIPP code precipitating flux output. The timing of the precipitated flux at different L-shells is the causative determination of the onset time difference between each disturbance at respective L-shells.

Figure 4-7 presents the normalized SFM for the NAA-CB, NAA-CN, NAA-NS, and NAA-SA paths. As expected, the poleward onset delay is observed in the modeling results. The NAA-CB path at the lowest latitude onsets first, NAA-CN at the next lowest latitude onsets second, NAA-NS onsets third, and NAA-SA onsets last. The onset difference is observed to be ~200 msec between the first three propagation paths and ~400 msec between NAA-NS and NAA-SA.

The non-ducted modeling results do not agree well with the experimental observations shown in Figure 4-5. Specifically, the NAA-CN path event onset occurs last in the experimental observation but occurs earlier than the NAA-NS and NAA-SA paths in the non-ducted

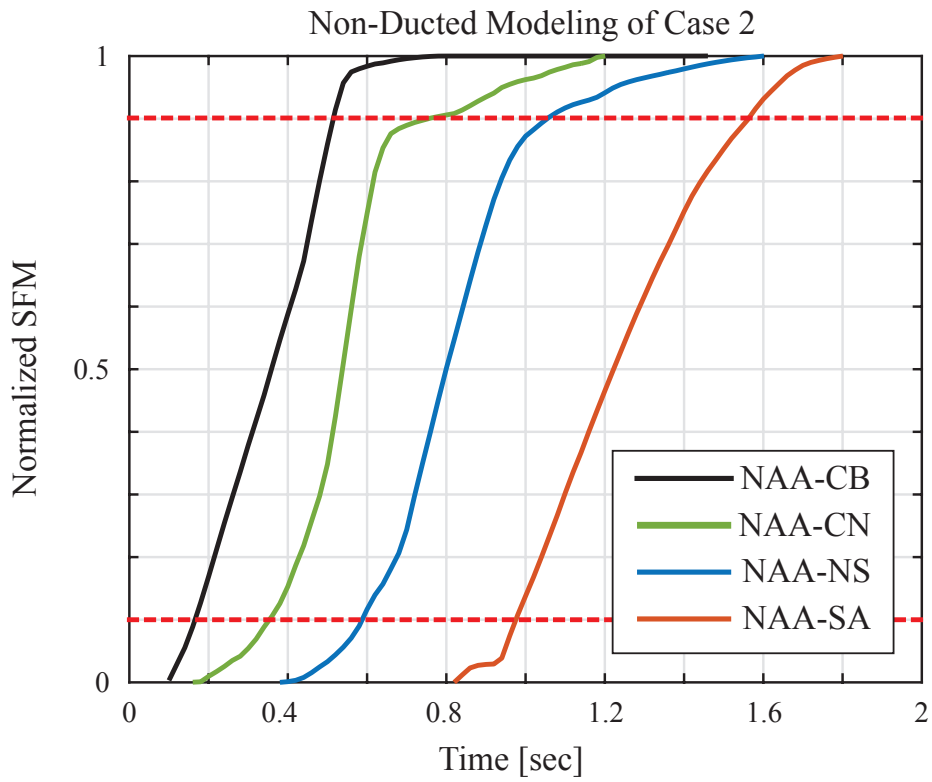

Figure 4-7. Normalized SFM modeling results for Case 2 if it were to be nonducted.

modeling results. Additionally, experimentally the NAA-NS and NAA-SA paths exhibit the same onset time but model predictions indicate a ∼400 msec time difference. It is clear that the experimental observations are not consistent with the non-ducted event interpretation.

Having shown that the non-ducted interpretation is not consistent with Case 2 observations, we now proceed to investigate this case using a ducted LEP event interpretation. As shown in Chapter 2, a ducted LEP event for which the radius remains constant exhibits the same onset duration everywhere. Instead, we model the ducted LEP case using an ionospheric disturbance that expands radially with time.

The first step is to determine the center of the disturbance to be modeled. Experimentally, the earliest event onset occurred on the NAA-NS and NAA-SA paths simultaneously, indicating that the center of the disturbance is somewhere half way in between these paths.

The second event onset is observed on the NLM-CN path, indicating the center of the disturbance should be located farther from this GCP and grow over time. This placement naturally locates the disturbance center farthest away from the NAA-CN path, which is consistent with observations, in that the NAA-CN path registered the latest event onset time. Based on this reasoning, the disturbance location is centered on the X in Figure 4-8. Concentric circles are presented surrounding the X with radii of 100, 200, and 300 km for reference. This disturbance's location is at 39.4° N and 80° W which is L-shell value of 2.4.

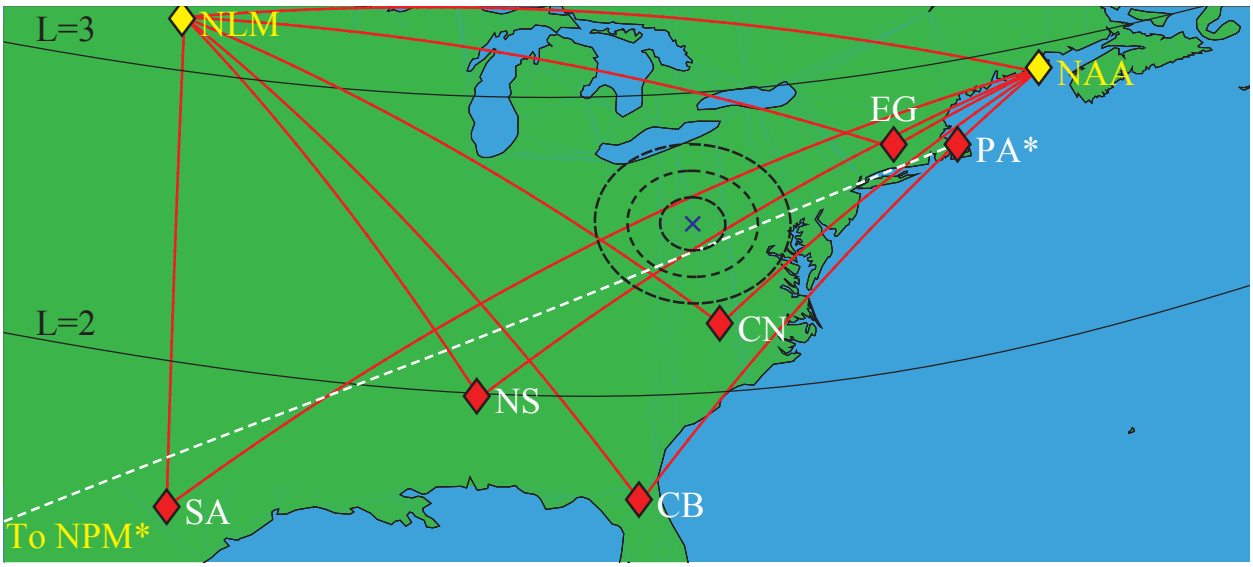

Figure 4-8. Illustration of the disturbance for Case 2 modeling with ducted perspective. The disturbance is located at X with concentric circles of which radii are 100, 200, and 300 km for reference.

The first model, WIPP, takes the latitude of the Case 2 causative sferic (34.1°) and the peak current of the return stroke (-214 kA), according to NLDN. The geomagnetic longitude of the disturbance from the scenario above is approximately 3.8° W. As discussed in the earlier section, because the WIPP code assumes the longitude of the precipitation location is the same as the causative sferic longitude, the L-shell dependent loss cone angles at the longitude of the disturbance, X, are implemented to account for the longitudinal loss cone effect. The loss cone angle at the geomagnetic longitude of the disturbance (3.8° W) can be deduced from Figure 2-3. The respective incoming flux at L=2.4 for both hemispheres is then input into the FEED

model. The FEED model calculates the secondary ionization throughout the lower ionosphere and the electron density profiles integrated over time.

The integrated electron density profiles at location X are simulated as a scattering body in LWPC with five GCPs of the transmitter-receiver pairs (NAA-NS, NAA-SA, NLM-CN, NPM-PA, and NAA-CN). The radius of the scattering body increases temporally and scatters the five GCPs respectively. As the scattering body expands with time, each GCP is perturbed according to the geometry between the path and the time-varying disturbance. The GCPs that are close to the center of the disturbance (NAA-NS and NAA-SA) are perturbed first when the radius of the disturbance is small. As the disturbance grows over time, the GCPs that are farther away from the disturbance center (NLM-CN, NPM-PA, and NAA-CN) are sequentially perturbed, according to the size of the disturbance and the distance to the GCP.

The Full Width Half Max (FWHM) of the Gaussian scattering body is designed to increase with time radially. The FWHM increases parabolically from $\sim$30 km at 0 second to $\sim$300 km at 0.8 second in both hemispheres and stays at maximum afterwards. The rapid expansion of the FWHM corresponds to the region of the maximum of the incoming energy flux in both hemispheres. Also, the maximum FWHM ($\sim$300 km) in the northern hemisphere is designed in order to perturb the farthest GCP of NAA-NS.

After combining the three codes to model the Case 2 observation, the resulting normalized SFM are shown in Figure 4-9. Having defined the onset time as the 10% point of the maximum perturbation, NAA-NS (blue) and NAA-SA (red) exhibit nearly the same onset time with 0.19 and 0.20 seconds, respectively. NLM-CN (yellow) and NAA-CN (purple) have onset times of 0.34 second and 0.44 second, respectively. The conjugate path of NPM-PA (green) shows an event onset time of 0.35 seconds. The first perturbations occurred on the NAA-SA and NAA-NS paths, which start nearly at the same time, the second perturbation in the northern hemisphere is on the NLM-CN path while the NPM-PA perturbation closely follows in time in the southern hemisphere, and the last event onset happens on the NAA-CN path nearly 0.25 seconds after the first perturbations.

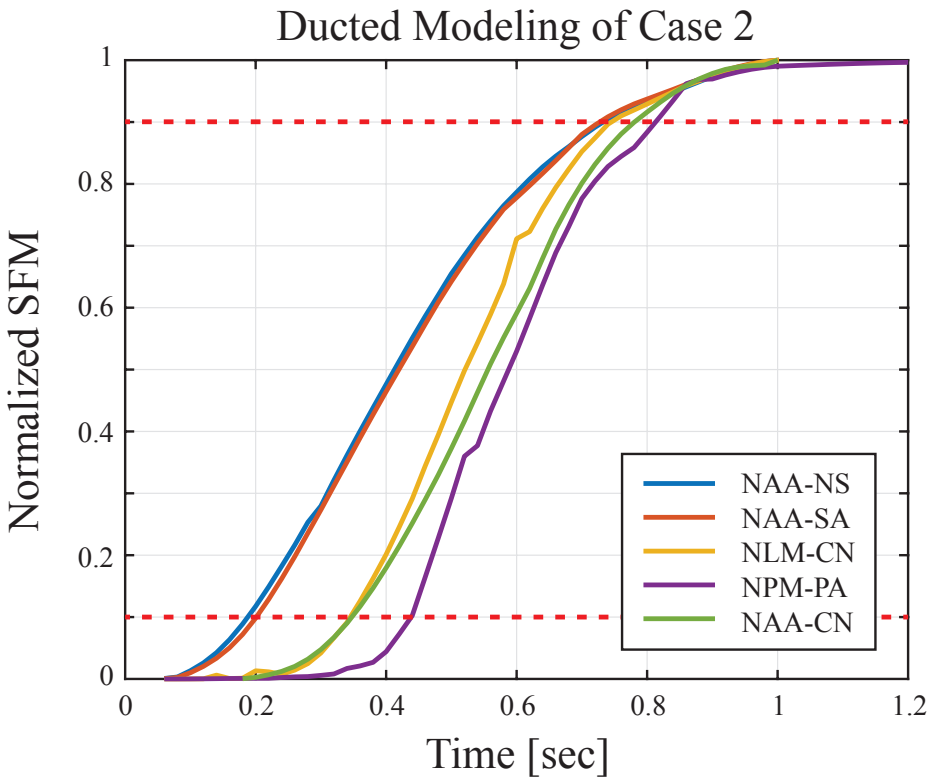

Figure 4-9. Normalized SFM modeling results for Case 2 with five GCPs.

These modeling results agree well with the experimental observations presented for Case 2, shown in Figure 4-5. In both of the observation and the modeling results, the NAA-NS and NAA-SA paths are perturbed simultaneously first. The NLM-CN and NPM-PA paths are perturbed second, and the NAA-CN path is perturbed last. The modeling onset time differences between NAA-NS and each propagation path are ~150 msec for NLM-CN and NPM-PA and 250 msec for NAA-CN, which agree closely to the observation onset time differences (100 msec, 150 msec, and 300 msec, respectively in the observations). The Case 2 observations thus appear to be consistent with the scattering from an ionospheric disturbance that is expanding radially with time. The inference is that ducted electron precipitation may very well produce an ionospheric disturbance that can expand radially with time.

4.4 Discussion and Summary

Non-ducted and ducted LEP events exhibit dramatically different onset timing signatures. Non-ducted LEP events exhibit poleward displacement behavior over time, whereas what are presumed to be ducted LEP events exhibit radial expansion from a central point over time. This chapter shows the first examples of conjugate non-ducted LEP events and conjugate ducted LEP events. These two different types of events would impact interhemispheric timing statistics, such as those presented in Chapter 3, in dramatically different ways, depending on the observation geometries in the northern and southern hemispheres.

It is in this context that we reinterpret the statistical observations presented in this dissertation and in previous work (*Burgess and Inan*, 1990; *Cotts et al.*, 2011; *Golkowski et al.*, 2014). The use of individual receivers in the northern and southern hemispheres to detect LEP events does not (at this point in time) provide a means to identify whether the LEP event is a non-ducted or a ducted LEP event. It is also completely unknown how often the two types of LEP events occur. Because the two events produce different spatio-temporal signatures, they are expected to produce different interhemispheric timing statistics. Based on these observations it becomes clear that the statistics presented in this dissertation and in previous work do not discern between ducted and non-ducted events and thus blend the different event statistics together.

It is possible that arrays like the NAV array can be used to automatically discern between ducted and non-ducted events on a large-scale basis. Without an equivalent array in the southern hemisphere, however, the observed interhemispheric timing differences will be dominated by the spatio-temporal development of the ionospheric disturbance, rather than the timing of the magnetospheric processes involved.

CHAPTER 5
SUMMARY AND SUGGESTION FOR FUTURE WORK

5.1 Summary

This dissertation experimentally and theoretically investigated many aspects of conjugate lightning-induced electron precipitation (LEP) events with a focus on interhemispheric timing differences. Ultimately, it was shown that non-ducted and ducted LEP events exhibit very different spatio-temporal development signatures that affect interhemispheric timing measurements in different ways. As a result, it was shown that remote sensing of the magnetosphere using ground-based LEP measurements is possible, but requires receiver arrays in the northern and southern hemispheres in order to identify and quantify propagation and scattering effects and isolate the magnetospheric processes of interest.

Chapter 1 highlighted the scientific background and knowledge that are necessary to understand LEP event physics. Ionospheric and magnetospheric plasma physics were introduced, and the LEP-related numerical models were introduced, including the WIPP, Monte Carlo deposition, and LWPC models.

Chapter 2 introduced a new precipitation model, FEED. The fundamental equations used in the FEED model were developed in great detail. The FEED model was validated against a well-accepted Monte Carlo model. The main benefits of the FEED model is that it runs significantly faster than the Monte Carlo method, although it does not account for several effects important for other applications. The longitudinal dependence on the loss cone angle was implemented in the WIPP code, which showed minimal timing effect but significant change in precipitating flux. Combining the three models (WIPP, FEED, and LWPC) was described in detail. These combined models represented three stages of the entire LEP process and allowed the temporal and spatial effects of the precipitating disturbance to be simulated. The fast run time of the FEED model made it possible to calculate the large number of electron density changes as a function of time, to be input into the LWPC propagation model. The 3D LWPC

was run sequentially in time, varying the properties of the scattering body, to determine the effects on the VLF signal.

In Chapter 3, a large number of conjugate LEP events were observed and analyzed statistically. To quantify the interhemispheric timing of conjugate LEP events more precisely, scattered field analysis was employed. Sequential scattered field analysis was employed to isolate overlapping VLF perturbations. Characterizing LEP timing with amplitude only measurements and scattered field magnitude measurements produced different statistical results. The onset time was more likely (75%) to be earlier in the south using the amplitude only measurements, which turned out to be a 60-40 chance when using the scattered field magnitude. Observations definitively ruled out atmospheric backscatter as the physical process governing the observed interhemispheric timing differences. Modeling efforts appear to show that the onset was determined based on the geometry of the disturbance with the propagation path. Depending on the geometry, the propagation path located along lower latitudes would be perturbed earlier with a non-ducted perspective, while the higher latitude propagation path could be perturbed first with a ducted perspective.

Chapter 4 presented LEP observations using a mesh of VLF receivers that demonstrated the spatio-temporal development of the precipitation. The first case showed traditional poleward displacement as many previous efforts have modeled and observed. This non-ducted case perturbed two signal paths in the northern hemisphere and one conjugate path in the southern hemisphere. Whether in the north or the south, the perturbation timing aligned with the L-shell of the propagation path at the longitude of the causative lightning flash. An interesting feature was that the identified causative sferic was located at a higher latitude than the propagation path that the LEP event onset was first observed.

Chapter 4 also presented a case exhibiting radial expansion of the electron precipitation, which has not been reported previously. The LEP disturbance was detected on five Tx-Rx propagation paths with delays in the onset time in the radial direction. The observations in

this case were modeled with the ducted and non-ducted perspectives. The results of the non-ducted modeling effort (poleward time delay) did not agree with the experimental observation. The ducted modeling results, however, exhibited radial expansion with time, agreeing well with experimental observations. For the ducted model, an LEP disturbance was designed to have a radius growing over time and it sequentially perturbed the propagation paths in the lateral direction showing a excellent agreement with the experimental observations.

This dissertation has demonstrated with experimental observations and with modeling simulations that the spatio-temporal development of the LEP disturbance dominates inter-hemispheric timing calculations. To determine magnetospheric properties using these types of observations, numerous propagation paths covering the disturbance region both in northern and southern hemispheres are required.

5.2 Suggestions for Future Work

While this dissertation presents great improvement in understanding lightning induced electron precipitation events, there is still room for future improvement.

More southern hemisphere observation locations would be valuable. Most of the VLF receivers are currently located in North America, which I took great advantage of for this dissertation. The conjugate area of the northern hemisphere receivers is around the Antarctic Peninsula. Other than the current VLF receiver at Palmer Station, Antarctica, more receivers could be utilized to create a mesh in the southern hemisphere as well. With a mesh grid of GCPs in the southern hemisphere, the spatio-temporal development of conjugate LEP events could be analyzed in both hemispheres.

The way of combining three numerical models can also be improved. The three models are separate standalone programs, and a user should manually link them together feeding an output to another's input. The WIPP code is currently written in C shell and FORTRAN, the FEED model is written in MATLAB, and the 3D LWPC is written in FORTRAN. In the future, WIPP, FEED, and LWPC can be translated in a common language to streamline

the integration from one code to another. Having one standalone program could be more user-friendly.

The current WIPP code assumes that the precipitation occurs at the same longitude as the causative sferic longitude, because it is currently two dimensional. The code could be improved to consider three dimensional refraction and account for the longitudinal drift effects in the radiation belts.

Lastly, the current FEED model does not account for electron density recovery with time. Relatively well-known ionospheric chemistry involved with LEP recovery could be potentially modeled and combined with the FEED model to simulate the entire LEP VLF signature. Including the electron density recovery in the FEED model could potentially allow modeling of overlapped LEP events which occur more often than standalone LEP events.

REFERENCES

Abel, B., and R. M. Thorne (1998), Electron scattering loss in Earth's inner magnetosphere 1. Dominant physical processes, *J. Geophys. Res.*, *103*(A2), 2385-2396.

Angerami, J. J., and J. O. Thomas (1964), Studies of Planetary Atmospheres. 1. Distribution of Electrons + Ions in Earths Exosphere, *J. Geophys. Res.*, *69*(21), 4537.

Ashour-Abdalla, M. (1972), Amplification of whistler waves in the magnetosphere, *Planetary and Space Science*, *20*(5), 639-662.

Baker, D. N., X. Li, J. B. Blake, and S. Kanekal (1998), Strong electron acceleration in the Earth's magnetosphere, *Advances in Space Research*, *21*, 4, 609-613.

Bell, T. F. (1984), The nonlinear gyroresonance interaction between energetic electrons and coherent VLF waves propagating at an arbitrary angle with respect to the Earth's magnetic field, *J. Geophys. Res.*, *89*, 905-918.

Berger, M. J., M. Inokuti, H. H. Anderson, H. Bichsel, J. A. Dennis, D. Powers, S. M. Seltzer, and J. E. Turner (1984), Stopping powers for electrons and positrons, *Journal of the International Commission on Radiation Units and Measurements*, *19*, 2.

Bethe, H. A., and J. Ashckin (1953), Passage of Radiation of Radiation through Matter, *Experimental Nuclear Physics*, *1*, 166, John Wiley, New York.

Born, M. and E. Wolf (1961), *Principles of Optics*, Pergamon, New York.

Bortnik, J. (2005), Precipitation of radiation belt electrons by lightning-generated magnetospherically reflecting whistler waves, (Doctoral dissertation). Stanford University.

Bortnik, J., U. S. Inan, and T. F. Bell (2006), Temporal signatures of radiation belt electron precipitation induced by lightning-generated MR whistler waves: 1. Methodology, *J. Geophys. Res.*, *111*, A02204, doi:10.1029/2005JA011182.

Bortnik, J., U. S. Inan, and T. F. Bell (2006), Temporal signatures of radiation belt electron precipitation induced by lightning-generated MR whistler waves: 2. Global signatures, *J. Geophys. Res.*, *111*, A02205, doi:10.1029/2005JA011398.

Budden, K. G. (1985), *The propagation of radio waves*, Cambridge University Press.

Burch, J. L., T. E. Moore, R. B. Torbert, and B. L. Giles (2016), Magnetospheric multiscale overview and science objectives, *Space Sci Rev*, 199, 5-21, doi:10.1007/s11214-015-0164-9.

Burgess, W. C., and U. S. Inan (1990), Simultaneous disturbance of conjugate ionospheric regions in association with individual lightning flashes, *Geophys. Res. Lett.*, *17*, 259.

Carpenter, D. L., and R. R. Anderson (1992), An ISEE/Whistler Model of Equatorial Electron-Density in the Magnetosphere, *Journal of Geophysical Research-Space Physics*, 97 (A2), 1097-1108.

Chang, H. C., and U. S. Inan (1983), Quasi-relativistic electron precipitation due to interactions with coherent VLF waves in the magnetosphere, *J. Geophys. Res.*, *88*, 318-328.

Chen, L., W. Li, J. Bortnik, and R. M. Thorne (2012), Amplification of whistler-mode hiss inside the plasmasphere, *Geophys. Res. Lett.*, *39*, 8.

Cotts, B. R. T., M. Golkowski, and M. C. Moore (2011), Ionospheric effects of whistler waves from rocket-triggered lightning, *Geophys. Res. Lett.*, *38*, L24805, doi:10.1029/2011GL049869.

Cotts, B. R. T., U. S. Inan, and N. G. Lehtinen (2011), Longitudinal dependence of lightning-induced electron precipitation, *J. Geophys. Res.*, *116*, A10206, doi:10.1029/2011JA016581.

Cummer, S. A., T. F. Bell, U. S. Inan, and D. L. Chenette (1997), VLF remote sensing of high-energy auroral particle precipitation, *J. Geophys. Res.*, *102*, A4, 7477-7484.

Cummer, S. A., and U. S. Inan (1997), Measurement of charge transfer in sprite producing lightning using ELF radio atmospherics, *Geophys. Res. Lett.*, *24*, 14, 1731-4, Jul.

Cummer, S. A., U. S. Inan, and T. F. Bell (1998), Ionospheric D region remote sensing using VLF radio atmospherics, *Radio Science*, *33*(6), 1781-1792.

Cummins, K. L., M. J. Murphy, E. A. Bardo, W. L. Hiscox, R. B. Pyle, and A. E. Pifer (1998), A combined TOA/MDF technology upgrade of the U.S. National Lightning Detection Network, *J. Geophys. Res.*, *103*, 9038-9044.

DeWitt, R. N. (1962), The Occurrence of Aurora in Geomagnetically Conjugate Areas, *J. Geophys. Res.*, *67*, 1347-1352.

Dowden, R. L., J. B. Brundell, and C. J. Rodger (1997), Temporal evolution of very strong Trimpis observed at Darwin, Australia, *Geophys. Res. Lett.*, *24*, 2419-2242, doi:10.1029/97GL02357.

Dowden, R. L., and C. J. Rodger (1997), Decay of a vertical plasma column: A model to explain VLF sprites, *Geophys. Res. Lett.*, *24*(22), 2765-2768, doi:10.1029/97GL02822.

Dowden, R. L., C. J. Rodger and J. B. Brundell (2001), Decay of whistler-induced electron precipitation and cloud-ionosphere electrical discharge Trimpis: Observations andanalysis, *Radio Science*, *36*(1), 151-169.

Dungey, J. W. (1963), Loss of Van Allen electrons due to whistlers, *Planetary and Space Science*, *11*, 591-595.

Dysthe, K. B. (1971), Some studies of triggered whistler emissions, *J. Geophys. Res.*, *76*, 28, 6915-6931.

Faganello, M., F. Califano, and F. Pegoraro (2008), Competing mechanisms of plasma transport in inhomogeneous configurations with velocity shear: the solar-wind interaction with Earth's magnetosphere, *Physical Review Letters*, *100*, 015001.

Ferguson, J. A., and F. P. Snyder (1987), The segmented waveguide program for long wavelength propagation calculations, *Tech. Doc. 1071*, Naval Ocean Systems Center, San Diego, Calif..

Gledhill, J. A. (1973), The range-energy relation for 0.1-600 keV electrons, *J. Phys. A: Math., Nucl. Gen.*, *6*, 1420-1428.

Golkowski, M., N. C. Gross, R. C. Moore, B. R. T. Cotts, and M. Mitchell (2014), Observation of local and conjugate ionospheric perturbations from individual oceanic lightning flashes, *Geophys. Res. Lett.*, *41*, 273-279, doi:10.1002/2013GL058861.

Helliwell, R. A. (1965), *Whistlers and Related Ionospheric Phenomena*, Stanford University Press, Stanford, Calif..

Helliwell, R. A., J. P. Katsufrakis, and M. L. Trimpi (1973), Whistler-induced amplitude perturbation in VLF propagation, *J. Geophys. Res.*, *78*, 4679.

Haselgrove, J. (1954), Ray theory and a new method for ray tracing, *Report of the Physical Society Conference on Physics of the Ionosphere*, Cambridge, England 355-367.

Horne, R. B., R. M. Thorne, Y. Y. Shprits, N. P. Meredith, S. A. Glauert, A. J. Smith, S. G. Kanekal, D. N. Baker, M. J. Engebretson, J. L. Posch, M. Spasojevic, U. S. Inan, J. S. Pickett, and P. M. E. Decreau (2005), Wave acceleration of electrons in the Van Allen radiation belts, *Nature*, *437*(8), 227, doi:10.1038/nature03939.

Inan, U. S., and T. F. Bell (1977), The plasmapause as a VLF wave guide, *J. Geophys. Res.*, *83(19)* 2819.

Inan, U. S., T. F. Bell, and R. A. Helliwell (1978), Nonlinear pitch-angle scattering of energetic electrons by coherent VLF waves in the magnetosphere, *J. Geophys. Res.*, *82(19)* 127-142.

Inan, U. S. and D. L. Carpenter (1987), Lightning-induced electron precipitation events observed at L=2.4 as phase and amplitude perturbations on subionospheric VLF signals, *J. Geophys. Res.*, *92*, A4, 3293-3303.

Inan, U. S., D. C. Shafer, W. Y. Yip, and R. E. Orville (1988), Subionospheric VLF signatures of nighttime D region perturbations in the vicinity of lightning discharges, *J. Geophys. Res.*, *93*, A10, 11455-11472.

Inan, U. S., M. Walt, H. Voss, and W. Imhof (1989), Energy spectra and pitch angle distribution of lightning-induced electron precipitation: analysis of an event observed on the S81-1 (SEEP) satellite, *J. Geophys. Res.*, *94, (A2)* 1379-1401.

Jackson, J. D. (1999), *Classical electrodynamics*, 3rd edition, Wiley, New York.

Johnson, M. P., U. S. Inan, and D. S. Lauben (1999), Subionospheric VLF signatures of oblique (nonducted) whistler-induced precipitation, *Geophys. Res. Lett.*, 26(23), 3569-3572.

Kulkarni, P. U., U. S. Inan, T. F. Bell, and J. Bortnik (2008), Precipitation signatures of ground-based VLF transmitters, *J. Geophys. Res., (Space Physics)*, *113* A07, 214.

Kotovsky, D. A., and R. C. Moore (2015), Classifying onset durations of early VLF events: Scattered field analysis and new insights, *J. Geophys. Res.*, *120*, 6661-6668, doi:10.1002/2015JA021370.

Lauben, D. S. (1998), Precipitation of radiation belt electrons by obliquely-propagating lightning-generated whistler waves, (Doctoral dissertation). Stanford University.

Lauben, D. S., U. S. Inan, and T. F. Bell (1999), Poleward-displaced electron precipitation from lightning-generated oblique whistlers, *Geophys. Res. Lett.*, 26, 2633-36.

Laundal, K. M., I. Cnossen, S. E. Milan, S. E. Haaland, J. Coxon, N. M. Pedatella, M. Forster, J. P. Reistad (2017), North–south asymmetries in Earth' s magnetic field effects on high-latitude geospace, *Space Sci. Rev*, *206*, 225-257.

Lehtinen, N. G. (2000), Relativistic runaway electrons above thunderstorms, (Doctoral dissertation). Stanford University.

Li, X. and M. A. Temerin (2001), The electron radiation belt, *Space Science Reviews*, *95*, 569-580.

Li. W., R. M. Thorne, J. Bortnik, X. J. Zhang, J. Li, D. N. Baker, G. D. Reeves, H. E. Spence, C. A. Kletzing, W. S. Kurth, G. B. Hospodarsky, J. B. Blake, J. F. Fennell, S. G. Kanekal, V. Angelopoulos, J. C. Green, and J. Goldstein (2016), Radiation belt electrons acceleration during the 17 March 2015 geomagnetic storm: Observations and simulations, *J. Geophys. Res. Space Physics*, *121*, 5520-5536, doi:10.1002/2016JA022400.

Lyons, L. R., and R. M. Thorne (1973), Equilibrium structure of radiation belt electrons, *J. Geophys. Res.*, *78*, 2142-2179.

McIlwain, C. E. (1961), Coordinates for mapping the distribution of magnetically trapped particles, *J. Geophys. Res.*, *66*, 3681-3691.

McRae, W. M., and N. R. Thomson (2000), VLF phase and amplitude: daytime ionospheric parameters, *Journal of Atmospheric and Terrestrial Physics*, *62*, 609-618.

Mimno, H. R. (1937), The physics of the ionosphere, *Reviews of modern physics*, *9*, 1.

Mitchell, M. F. (2015), Very low frequency remote sensing of the lower ionosphere, PhD dissertation, University of Florida.

Miyoshi, Y., K. Sakaguchi, K. Shiokawa, D. Evans, J. Albert, M. Connors, and V. Jordanova (2008), Precipitation of radiation belt electrons by EMIC waves, observed from ground and space, *Geophys. Res. Lett.*, *35*, L23101.

Moore, R. C., and D. Agrawal (2011), ELF/VLF wave generation using simultaneous CW and modulated HF heating of the ionosphere, *J. Geophys. Res.*, *116*, A04217, doi:10.1029/2010JA015902.

Morgan, R. R. (1968), World-wide VLF effective conductivity map, *Tech. Rep. Report 8013F-1*, Westinghouse Electric Corporation Report 8013F-1.

Nishida, A. and K. Maezawa (1971), Two basic modes of interaction between the solar wind and the magnetosphere, *J. Geophys. Res.*, *76*, 10, 2254-2264.

Omura, Y. and D. Nunn (2011), Triggering process of whistler mode chorus emissions in the magnetosphere, *J. Geophys. Res.*, *116*, A05205.

Otsuka, Y., K. Shiokawa, T. Ogawa, and P. Wilkinson (2002), Geomagnetic conjugate observations of equatorial airglow depletions, *Geophys. Res. Lett.*, *29*, 1753, doi:10.1029/2002GL015347.

Pappert, R. A., and F. P. Snyder (1972), Some results of a mode-conversion program for VLF, *Radio Sci.*, *7*, 913.

Park, C. G. (1972), Methods of determining electron concentrations in the magnetosphere from nose whistlers, *Technical Report 3454-1*, Stanford University, Stanford, CA.

Peter, W. B. (2007), Quantitative measurement of Lightning-induced Electron Precipitation using VLF remote sensing (Doctoral dissertation), Stanford.

Peter, W. B., and U. S. Inan (2004), On the occurrence and spatial extent of electron precipitation induced by oblique nonducted whistler waves, *J. Geophys. Res.*, 109, A12215.

Peter, W. B., and U. S. Inan (2007), A quantitative comparison of lightning-induced electron precipitation and VLF signal perturbations, *J. Geophys. Res.*, *112*, A12212, doi:10.1029/2006JA012165.

Pierrard V., and G. Lopez Rosson (2016), The effects of the big storm events in the first half of 2015 on the radiation belts observed by EPT/PROBA-V, *Ann. Geophys.*, *34*, 75-84, doi:10.5194/angeo-34-75-2016.

Poulsen, W. L., T. F. Bell, and U. S. Inan (1990), Three-Dimensional modeling of subionospheric VLF propagation in the presence of localized D region perturbations associated with lightning, *J. Geophys. Res.*, *95*(A3), 2355-2366.

Poulsen, W. L., U. S. Inan, and T. F. Bell (1993a), A multiple-mode three dimensional model of VLF propagation in the Earth-Ionosphere waveguide in the presence of localized D region disturbances, *J. Geophys. Res.*, *98*(A2), 1705-1717.

Poulsen, W. L., T. F. Bell, and U. S. Inan (1993b), The scattering of VLF waves by localized ionospheric disturbances produced by lightning-induced electron precipitation, *J. Geophys. Res.*, *98*(A9), 15553-15559.

Rakov, V. A., and M. A. Uman (2003), *Lightning: Physics and Effects*, Cambridge Univ. Press, New York.

Ratcliffe, J. A. (1962), *The Magneto-Ionic theory and its applications to the ionosphere.*, Cambridge at the university press.

Ratovsky, K. G., J. K. Shi, A. V. Oinats, and E. B. Romanova (2014), Comparative study of high-latitude, mid-latitude and low-latitude ionosphere on basis of local empirical models, *Sience Direct*, *54*(2014), 509-516.

Rees, M. H. (1963), Auroral ionization and excitation by incident energetic electrons, *Planet. Space Sci.*, *11*, 1209-1218.

Reeves, G. D., H. E. Spence, M. G. Henderson, S. K. Morley, R. H. Friedel, H. O. Funsten, D. N. Baker, S. G. Kanekal, J. B. Blake, J. F. Fennell, S. G. Claudepierre, R. M. Thorne, D. L. Turner, C. A. Kletzing, W. S. Kurth, B. A. Larsen, and J. T. Niehof (2013), Electron acceleration in the heart of the Van Allen radiation belts, *Science*, *341*, 6149, 991-994.

Rodriguez, J. V. (1994), Modification of the Earth's ionosphere by very low-frequency transmitters, (Doctoral dissertation). Stanford University.

Rogers, S. C (1963), Radiation damage to satellite electronic systems, *IEEE Transactions on Nuclear Science*, *10*, 1, 97-105.

Sa, L. A. D. (1990), A wave-particle-wave interaction mechanism as a cause of VLF triggered emissions, *J. Geophys. Res.*, *95*(A8), 12277-12286.

Saito, A., T. Iyemori, M. Sugiura, N. C. Maynard, T. L. Aggson, L. H. Brace, M. Takeda, and M. Yamamoto (1995), Conjugate occurence of the electric field fluctuations in the nighttime midlatitude ionosphere, *J. Geophys. Res.*, *100*(A11), 21439-21451.

Tarcsai, G., P. Szemeredy, and L. Hegymegi (1988), Average electron density profiles in the plasmasphere between L=1.4 and 3.2 deduced from whistlers, *Journal of Atmospheric and Terrestrial Physics*, *50*, 607-611.

Tascione, T. F. (1988), *Introduction to the space environment.*, Krieger Publishing Company, Malabar, Florida.

Thomson, N. R. and M. A. Clilverd (2001), Solar flare induced ionospheric D-region enhancements from VLF amplitude observations, *Journal of Atmospheric and Terrestrial Physics*, *63*, 16, 1729-1737.

Thorne, R. M. (2010), Radiation belt dynamics: the importance of wave-particle interactions, *Geophys. Res. Lett.*, *37*, L22107.

Thorne, R. M., Y. Y. Shprits, N. P. Meredith, R. B. Horne, W. Li, and L. R. Lyons (2007), Refilling of the slot region between the inner and outer electron radiation belts during geomagnetic storms, *J. Geophys. Res.*, *112*, A06203.

Tsunoda, R. T., and R. B. Cosgrove (2001), Coupled electrodynamics in the nighttime midlatitude ionosphere, *Geophys. Res. Lett.*, *28*, 22.

Uman, M. A. (1984), *Lightning*, Dover, Mineola, N.Y..

Vette, J. (1991), The AE-8 trapped electron model environment, National Space Science Data Center, *Report 91-24*, Greenbelt, Maryland.

Voss, H. D., W. L. Imhof, M. Walt, J. Mobilia, E. E. Gaines, J. B. Reagan, U. S. Inan, R. A. Helliwell, D. L. Carpenter, J. P. Katsufrakis and H. C. Chang (1984), Lightning-induced electron precipitation, *Nature*, *312*, 740.

Voss, H. D., M. Walt, W. L. Imhof, J. Mobilia, and U. S. Inan (1998), Satellite observations of lightning-induced electron precipitation, *J. Geophys. Res.*, *103*, A6, 11725-11744.

Wait, J. R. (1961), *Waves in stratified media*, vol. 3, Permagon Press, New York.

Wait, J. R. (1964), Calculated diffraction effects at VLF from a localized ionospheric depression, *Tech. Note 208*, National Bureau of Standards, Boulder, Colo..

Walt, M. (2005), *Introduction to Geomagnetically Trapped Radiation*, Cambridge University Press.

Westcott, B. S. (1962a), Ionospheric reflection processes for long radio waves - I, *J. Atmos. Terr. Phys.*, *24*, 385-399.

Westcott, B. S. (1962b), Ionospheric reflection processes for long radio waves - II, *J. Atmos. Terr. Phys.*, *24*, 619-631.

BIOGRAPHICAL SKETCH

Dooyoung Kim was born in Seoul, Republic of Korea. She attended Gwangmyeong High School in Gyeonggi-do, Republic of Korea. Dooyoung pursued a double degree program for two bachelor's degrees in electrical engineering. In May 2012, She completed a Bachelor of Science degree in electrical engineering with Cum Laude from South Dakota State University in Brookings, South Dakota and in August 2012, another Bachelor of Science degree in electrical engineering from Chung-Ang University in Seoul, Republic of Korea. She completed her master's degree in electrical and computer engineering at University of Florida in Dec 2013. In 2014, Dooyoung enrolled in the Ph.D. program at the University of Florida, department of electrical and computer engineering in Gainesville, Florida. Dooyoung completed her Ph.D. at the University of Florida with primary adviser, Dr. Robert Moore, in August 2020.